Build from the SMEFT up

SMEFT global analyses as a bottom-up approach to constrain BSM physics

Dissertation

Emma Geoffray

Dissertation

submitted to the

Combined Faculty of Mathematics, Engineering and Natural Sciences
of Heidelberg University, Germany

for the degree of

Doctor of Natural Sciences

Put forward by

Emma Geoffray

born in Lyon, France

Oral examination: 15.2.2023

Build from the SMEFT up

**SMEFT global analyses as a bottom-up approach
to constrain BSM physics**

Abstract

Measurements at the Large Hadron Collider (LHC) have so far been remarkably compatible with the Standard Model (SM). Standard Model effective field theory (SMEFT) global analyses are an established framework to re-interpret combinations of measurements as constraints on physics beyond the Standard Model (BSM). But the power of these analyses is that they can also act as springboard to constrain ultraviolet (UV) models. We present this bottom-up approach to setting limits on BSM physics in two steps.

First, we upgrade an existing SMEFT global analysis for Higgs and electroweak (EW) processes, adding over 30 new measurements and constraining two additional operators. We compare the results obtained through profile likelihood and Bayesian marginalization frameworks. We find that the results have a good level of agreement. Differences are observed when a distribution with an under-fluctuation in the high kinematic region leads to volume effects in the marginalization treatment.

Second, we show how to extend the previous SMEFT analysis with a matching procedure to derive constraints on the parameters of a UV model. We then perform a global analysis for the heavy vector triplet (HVT) model. Our results highlight the importance of theory uncertainties arising from the matching. We discuss the complementarity of constraints from SMEFT analyses and model-specific searches.

Zusammenfassung

Die Messungen am LHC waren bisher bemerkenswert gut mit dem Standardmodell (SM) vereinbar. Globale Analysen der effektiven Feldtheorie des Standardmodells (SMEFT) sind ein etablierter Rahmen für die Neuinterpretation von Messkombinationen als Einschränkung der Physik jenseits des Standardmodells (BSM). Die Stärke dieser Analysen liegt jedoch darin, dass sie auch als Sprungbrett für die Einschränkung von Ultraviolett-Modellen dienen können. Wir präsentieren diesen Bottom-up-Ansatz zur Festlegung der Grenzen für die BSM-Physik in zwei Schritten.

Als Erstes aktualisieren wir eine bestehende, globale SMEFT-Analyse für Higgs- und elektroschwache (EW) Prozesse, indem wir über 30 neue Messungen hinzufügen und zwei zusätzliche Operatoren einschränken. Wir vergleichen die Ergebnisse, die durch das Profil-Likelihood- und Bayes'sche Marginalisierungsverfahren erzielt wurden. Damit wird fest gestellt, dass die Ergebnisse ein gutes Maß an Übereinstimmung aufweisen. Unterschiede werden beobachtet, wenn eine Verteilung mit einer Unterfluktuation in der hohen kinematischen Region zu Volumeneffekten bei dem Marginalisieren führt.

Zweitens zeigen wir, wie die vorangegangene SMEFT-Analyse mit einem Matching-Verfahren erweitert werden kann, um Beschränkungen für die Parameter eines UV-Modells abzuleiten. Anschließend führen wir eine globale Analyse für das Modell des schweren Vektortripletts (HVT) durch. Unsere Ergebnisse unterstreichen die Bedeutung der theoretischen Unsicherheiten, die sich aus dem Matching ergeben. Wir diskutieren die Komplementarität von Beschränkungen aus SMEFT-Analysen und modellspezifischen Suchen.

Contents

List of Abbreviations

1D   one-dimensional

1LPI   one-light-particle irreducible

1PI   one-particle irreducible

2D   two-dimensional

2HDM   two-Higgs-doublet model

ATLAS   A Toroidal LHC Apparatus

BCS   Bardeen–Cooper–Schrieffer

BSM   beyond the Standard Model

CL   confidence level

CMS   Compact Muon Solenoid

CP   charge and parity

CPT   charge, parity and time reversal

CR   control region

DOF   degrees of freedom

DY   Drell-Yan

EFT   effective field theory

EW   electroweak

EWPO   electroweak precision observables

ggF   gluon-fusion

HEFT   Higgs effective field theory

HISZ   Hagiwara, Ishihara, Szalapski, and Zeppenfeld

HL-LHC high-luminosity LHC

HVT   heavy vector triplet

HXSWG   Higgs cross section working group

IR   infrared

LEFT   low-energy effective field theory

LEP   Large Electron-Positron Collider

LHC	Large Hadron Collider
LO	leading order
MCMC	Monte Carlo Markov chains
MFV	Minimal Flavor Violation
MSSM	minimal supersymmetric Standard Model
NLO	next-to-leading order
PDF	probability density function
QCD	quantum chromodynamics
QFT	quantum field theory
RG	renormalization group
RGE	renormalization group equations
SM	Standard Model
SMEFT	Standard Model effective field theory
SR	signal region
SSB	spontaneous symmetry breaking
STXS	simplified template cross sections
SUSY	supersymmetry
UFO	universal FEYNRULES output
UV	ultraviolet
VBF	vector boson fusion
VEV	vacuum expectation value
WBS	Weak boson fusion
WC	Wilson coefficient
WET	weak effective field theory

Preface

This thesis is based on research conducted between 2020 and 2022 at the Institute for Theoretical Physics of Heidelberg University in collaboration with other researchers.

The results presented in Chaps. 4 and 5 and have previously been published as:

[1] I. Brivio, S. Bruggisser, N. Elmer, E. Geoffray, M. Luchmann, T. Plehn,
To Profile or To Marginalize – A SMEFT Case Study,
arXiv:2208.08454,

[2] I. Brivio, S. Bruggisser, E. Geoffray, W. Kilian, M. Krämer, M. Luchmann, T. Plehn, B. Summ,
From Models to SMEFT and Back?,
SciPost Phys. 12, 036 (2022), arXiv:2108.01094.

Part of the research carried out during that time did not fit within this thesis, including the following peer-reviewed paper:

[3] A. Esposito, E. Geoffray, T. Melia,
Effective Field Theory for Acoustic and Pseudo-Acoustic Phonons in Solids,
Phys. Rev. D 102, 105009 (2020), arXiv:2006.05429.

Finally, the author is involved in several ongoing projects not ready for publication at the time of this writing.

Introduction

Ten years after the Higgs discovery [4,5], there is still no definite sign of physics beyond the Standard Model (BSM) at the LHC. The Standard Model (SM) of particle physics has been extensively tested and the discovery of the Higgs boson represented its resounding success. However, many questions echo in the ensuing detector silence: what is the nature of dark matter and dark energy? How come neutrinos have mass? Why is the Higgs mass so light? How was the matter-antimatter asymmetry generated? Why is CP-symmetry conserved by QCD interactions? Some of these problems are motivated by other areas of physics. For example, astrophysics and cosmology reveal the presence of weakly coupled dark matter [6–17] . However, most attempts at solving them entail UV models describing new particles and new interactions, which would lead to distinct signatures at colliders. Despite all the measurements performed by the LHC, no trace of new physics has been observed so far [18–29].

New particles might still be hiding in plain sight and revealed by increasing the statistics and precision of some distributions. It is also a distinct possibility that BSM physics is either too weakly coupled or too heavy to be discovered at the LHC. A plethora of dark matter experiments have been (and continue to be) developed to address the problem of a feeble coupling strength [9]. The Standard Model effective field theory (SMEFT), on the other hand, aims to tackle the second problem: what if new physics is too heavy?

If new physics is too heavy and every measurement at the LHC (and other experiments) is ultimately compatible with its SM prediction, the only way to learn from this scenario is to set limits. Constraints can be set either in a model dependent or independent way. The first case derives limits on one UV model at a time. The second one uses the SMEFT to derive general constraints on many types of new physics (within a few assumptions). The SMEFT is a low energy theory describing high energy physics as deviations from the SM, expressed in terms of local operators. It presents itself as an expansion in terms of these local operators and the new physics scale Λ which is parametrized by the Wilson coefficients (WCs). It is considered a model independent way to look for new physics, because its formulation is agnostic to the particular UV completion realized by nature. This theory is well-defined and is able to describe any new physics signature for which the new particles are heavy and sufficiently separated from the SM ones.

Many LHC measurements have been recast into limits on the SMEFT and various UV models over the past few years [19–26, 28–34]. However, most models affect several processes at once and several experiments may constrain a given model. Additionally, the LHC has produced—and will continue to produce in the next 15 years [35]—a wealth of interconnected data. This means limits set through individual measurements are far from convincing. In this context, the need for a global approach to limit setting becomes apparent, which takes into account all the relevant measurements and model parameters.

Global analyses have been performed for the SMEFT and UV models [1, 2, 30–33, 36–50]. Although they give limits which are much more robust than those derived from individual measurements for a limited number of parameters, they also require a lot of time to implement. Meanwhile, new UV models are being invented every week. Computing the predictions to recast all the relevant measurements and derive constraints for each of them would amount to an incredible number of PhD lifetimes.

Thankfully, the SMEFT can also be used as a bottom-up approach to constrain BSM physics. This means SMEFT global analyses can not only set limits on the WCs of the SMEFT expansion, but also on UV model parameters. To explain how this works, we need to come back to our previous statement: the SMEFT can describe any type of new physics, as long as it is sufficiently heavy. This is ensured by the decoupling theorem [51]. This theorem states that, given sufficient scale separation between two physical phenomena, the high energy physics can be expressed in terms of local interactions described by an effective field theory (EFT). As we said previously, this means the SMEFT can be used to look for new physics while remaining agnostic to its specific realization. On the other hand, it also means that matching relations can be derived, which express the WCs as functions of the hypothetical UV parameters. This is the missing piece of the bottom-up approach to limit setting.

EFTs in general and the SMEFT in particular can be seen as swiss knives in the limit-setter's toolbox. They are suitable for any problem where the full theory is unknown or too complicated for the task at hand. Our situation fits both of these requirements. We do not know what kind of BSM physics is realized by nature, how complex or how heavy it is. We especially do not want to set-up a global analysis from scratch for every UV model ever created. However, using a SMEFT global analysis as a stepping stone, the only ingredient missing to set constraints on a given UV model are the matching equations. UV global analyses become more accessible and less time-consuming when building from the SMEFT up.

This work illustrates this approach in two parts. The first goal is to perform an updated SMEFT global analysis for Higgs and EW processes. In particular, we will study how various assumptions and measurements can affect the final constraints. The second objective is to extend the SMEFT framework already in place to carry out a global analysis for a UV model instead. Once again, this is made possible because UV models can be matched onto the SMEFT, which leads to matching equations relating the WCs in the SMEFT to the UV model parameters. In this way, a SMEFT framework (which is UV model independent) can be simply re-purposed to set limits on any relevant UV model.

The thesis is organized as follows: in Chap. 2 we review the SMEFT, its assumptions and our choice of basis for Higgs and EW processes. In Chap. 3, we present the SFITTER framework we will use to perform global analyses. Chapter 4 shows the updated SFITTER SMEFT global analysis in Higgs and EW sector, which includes over 30 new measurements and two additional SMEFT operators. In particular, we investigate the impact of using profiled or marginal likelihoods and discuss the consequences of volume effects on the marginal results. In Chap. 5, we expand upon the SMEFT global analysis to set limits on a specific UV model—the HVT model—by simply adding a matching interface to SFITTER. We focus on the impact of the matching scale on the constraints and compare the results obtained through our SMEFT framework with limits from direct searches. Finally, we conclude and discuss potential avenues for future research in Chap. 6.

Standard Model effective field theory (SMEFT)

2.1 What are effective field theories (EFTs)?

From the well known multipole expansion of electrodynamics, through BCS theory of superconductivity, all the way to an EFT of gravity which extends General Relativity [52–56], there are many examples of effective theories being used in physics. EFTs in particular are quantum field theories (QFTs) and commonly used in the fields of condensed matter and particle physics.

Examples in condensed matter usually involve low-energy EFTs which spontaneously break spacetime symmetries, such as EFTs for superfluids [57–65], for solids [3, 59, 66, 67], and for many other condensed matter systems [59, 68–71]. While examples in particle physics include both low and high energy EFTs. The low energy EFTs are obtained by integrating out heavy particles, such as for the weak effective field theory (WET) (sometimes also called low-energy effective field theory (LEFT)) which describes the interactions of SM particles below $80\,\mathrm{GeV}$, i.e. integrating out the W and Z bosons as well as the top quark and the Higgs boson [72–74]. On the other hand, high energy EFTs are used to parametrize potential new physics above the top mass. Examples include the Standard Model effective field theory (SMEFT) [75, 76] and the Higgs effective field theory (HEFT) [77–80].

Why are EFTs integral to so many areas of physics? What makes them so useful? The main reason is that EFTs can describe deviations from physics at a given energy scale E, without knowing the details of the (often more complex) physics that goes on at a higher energy scale $\Lambda \gg E$.

There are two ways to harness this property. The first use case assumes one knows the details at the high energy scale Λ, but does not want to carry the cumbersome high energy theory framework because only a small fraction of it is useful to describe the low energy phenomena. Then an EFT can be used with a top-down approach: starting from the full high energy theory, one can match the high energy theory onto the low energy EFT by integrating out heavy particles—also called degrees of freedom (DOF)—and running the couplings between heavy particles' mass scales. This results in WCs as functions of the high energy theory parameters. This is for example the approach used to derive the weak effective field theory (WET), where one starts from the SM then integrates out the top quark, as well as the Higgs, W and Z bosons [72–74].

The reverse situation considers the bottom-up approach: starting from the low energy theory, we want to extend it systematically and parametrize any new physics in terms of the low energy degrees of freedom and symmetries we already know. This view assumes that some unknown heavy particles mediate new interactions. Within the EFT, these heavy particles can not be produced and these new interactions appear as point-like interactions, which require new higher order operators to describe them. These new operators are associated to effective coefficients: the Wilson coefficients (WCs). The result is an effective theory which provides a UV model independent way to investigate new physics. This is the way the SMEFT is built and used.

We will go into more details on the specific case of the SMEFT in Sec. 2.2. But first, we want to discuss an assumption inherent in choosing to work with EFTs and how to generally construct an EFT from bottom-up.

The inevitable assumption when using an EFT framework is a separation of scales. One assumes new physics results in small deviations that can be described by an expansion in E/Λ, where E is the low energy scale and Λ is the new physics scale. This assumption breaks down if Λ is not sufficiently separated from E, and the EFT expansion starts diverging and ultimately breaks unitarity.

To build an EFT from bottom-up, the starting point is always to consider the symmetries and particle content of the low energy theory. Note that for the EFT to be general, one should only impose the non-accidental symmetries of the low energy theory. From there, one needs to find all the independent operators built using the low energy particles that also abide by the symmetries. The number of operators is in principle infinite. Because we assume a separation of scales $\Lambda \gg E$, we can order them in an expansion and only consider the first few orders relevant to the specific phenomena we are studying. These new operators and their associated Wilson coefficients (WCs) parametrize new physics solely in terms of low energy degrees of freedom, i.e. in the terms of the particles that can be observed and produced at the low energy E. Whilst the expansion in Λ^{-1} gives us a way to classify new phenomena according to its complexity, i.e. the dimension of the EFT operator, which is a function of the number of particles involved in the new interaction.

To sum up, EFTs describe high energy physics, even when we do not know what this high energy physics is. Thus, they provide a UV model independent way to look for and constrain new physics. They assume a separation of scales between low and high energy phenomena. To construct an EFT, we start with the symmetries and particle content of the low energy theory. Then we add higher order operators mediating new interactions between those particles which respect the symmetries. Finally, we classify the operators in an expansion in Λ^{-1}, where Λ is the new physics scale, or equivalently according to their dimension.

2.2 SMEFT basics

As for any EFT, the SMEFT is based on the assumption that new physics is much heavier than the low energy theory it is based on—in this case the SM. Meaning it assumes there is a separation of scales between the masses of SM particles and those of new physics particles and, by extension, that there are no new light particles.

Starting with the non-accidental symmetries of the SM, presented in Tab. 2.1, and the particle content of the SM, shown in Tab. 2.2, one can construct the SMEFT Lagrangian

Gauge	before SSB	$SU(3)_C \times SU(2)_L \times U(1)_Y$
	after SSB	$SU(3)_C \times U(1)_Q$
Spacetime		Poincaré $ISO(3,1)$
Fundamental		CPT

Table 2.1: Non-accidental symmetries of the SM before and after spontaneous symmetry breaking (SSB).

by adding higher order operators which obey the symmetries. These operators $\mathcal{O}_x^d$ mediate new interactions between the SM particles and their associated Wilson coefficients (WCs) f_x parametrize deviations from the SM. Ordering these operators in an expansion in inverse powers of the new physics scale Λ, or equivalently according to their dimension d, one obtains the following SMEFT Lagrangian before spontaneous symmetry breaking (SSB):

$$\mathcal{L}_{\text{SMEFT}} = \mathcal{L}_{\text{SM}} + \sum_{d>4} \frac{1}{\Lambda^{d-4}} \sum_x f_x \, \mathcal{O}_x^d \tag{2.1}$$

for

$$\mathcal{L}_{\text{SM}} = \mathcal{L}_{\text{gauge}} + \mathcal{L}_{\text{Higgs}} + \mathcal{L}_{\text{fermion}} + \mathcal{L}_{\text{Yukawa}}, \tag{2.2}$$

$$\mathcal{L}_{\text{gauge}} = -\frac{1}{4} G_{\mu\nu}^A G^{A\mu\nu} - \frac{1}{4} W_{\mu\nu}^I W^{I\mu\nu} - \frac{1}{4} B_{\mu\nu} B^{\mu\nu},$$

$$\mathcal{L}_{\text{Higgs}} = (D_\mu \phi)^\dagger D^\mu \phi + \frac{m_h^2}{2} \phi^\dagger \phi - \frac{\lambda}{2} \left(\phi^\dagger \phi \right)^2,$$

$$\mathcal{L}_{\text{fermion}} = i \sum_{\text{generations}} \left(\bar{l}_L \slashed{D} l_L + \bar{e}_R \slashed{D} e_R + \bar{q}_L \slashed{D} q_L + \bar{d}_R \slashed{D} d_R + \bar{u}_R \slashed{D} u_R \right),$$

$$\mathcal{L}_{\text{Yukawa}} = -\sum_{\text{generations}} \left(\bar{l}_L Y_l \, \phi \, e_R + \bar{q}_L Y_d \, \phi \, d_R + \bar{q}_L Y_u \, \widetilde{\phi} \, u_R + \text{h.c.} \right),$$

where $Y_{l,d,u}$ are the Yukawa matrices with indices in the generation space, $\widetilde{\phi} = i\sigma^2 \phi^\star$, $v^2 = \frac{m_h^2}{\lambda}$ and we neglect the gauge fixing and ghost contributions to the SM Lagrangian [76, 81]. In what follows we drop the L, R indices for the fields before SSB as it is clear which ones are left- or right-handed.

Next we discuss SMEFT operators at dimension five, six and beyond.

At dimension five, there is only one independent SMEFT operator allowed by the symmetries, usually referred to as the Weinberg operator [82]. This operator violates lepton number conservation. But since lepton number is an accidental symmetry of the SM, the higher dimensional SMEFT operators do not have to preserve it. This operator also generates masses and mixings for neutrinos.

From there, things get complicated really fast. At dimension six, there are already 63 independent SMEFT operators (59 are baryon number conserving and 4 are baryon number violating) and that number is not even taking Hermitian conjugation or flavor structure into account [76]. If one were to take all three flavor generations into account, then the numbers of baryon number conserving operators grows from 59 to 2499 [83]. While counting all the Hermitian conjugate operators, the total number of operators goes from 63 to 84.

	Scalar Boson (spin 0)	Gauge Bosons (spin 1)			
Before SSB	ϕ ($SU(2)_L$ doublet)	g	W^1 $\quad$ W^2 $\quad$ W^3		B
After SSB	h	g	W^+ $\quad$ W^- $\quad$ Z		γ

	Fermions (spin 1/2) of generation $i = 1, 2, 3$
Before SSB	$u_{R,i}$ $\quad$ $d_{R,i}$ $\quad$ $q_{L,i}$ $e_{R,i}$ $\quad$ $l_{L,i}$
After SSB	u_i $\quad$ d_i ν_i $\quad$ e_i

Table 2.2: Particle content of the SM before and after spontaneous symmetry breaking (SSB). In what follows we drop the L, R indices for the fields before SSB as it is clear which ones are left- or right-handed.

Once at dimension seven and eight, the problem only gets bigger with respectively 30 and 993 independent operators for the simplest flavor assumption (including baryon violating operators and Hermitian conjugates) [84–87]. Clearly, there is no way for us to perform a global SMEFT analysis taking all these parameters into account. So we have to make assumptions to reduce the number of operators we consider.

2.3 Further assumptions

2.3.1 Minimal Flavor Violation (MFV)

For flavor, we start with the completely flavor symmetric assumption $U(3)^5$. This means the operators we consider, in this limit, appear in the Lagrangian summed over all generations.

However, since we want to include measurements that are flavor sensitive, we also break this symmetry for certain operators. This is called Minimal Flavor Violation (MFV) [88–90]. With this flavor assumption, we consider terms which break the $U(3)^5$ flavor symmetry only if they are proportional to the Yukawa matrices. Most importantly, these symmetry breaking operators are in one to one correspondence with the processes constraining them. So even though we break the symmetry in some instances where measurements are highly flavor sensitive, this does not create inconsistencies.

2.3.2 Tree level WCs with one exception

We only consider Wilson coefficients (WCs) that appear as tree level SMEFT corrections to the SM processes we include in the analysis, and assume that SMEFT corrections from higher loop orders are sub-leading.

However, we make one exception for gluon fusion production. As we will discuss further in Sec. 3.3.2, gluon fusion is the dominant Higgs boson production channel at the LHC and a 1-loop process. Thus, for gluon fusion production we consider SMEFT corrections up to 1-loop order.

2.3.3 Truncation at dimension six, but where?

As already mentioned, the number of operators to consider grows rapidly with each order of the expansion. Since the higher order operators are suppressed by higher orders of the new physics scale inverse, it is generally assumed that they can be neglected. Thus, for our SMEFT analysis, we have to decide where to cut the expansion, making sure that this choice is well motivated.

Sometimes, the dimension six operators are so well constrained by some processes that their contribution to another becomes negligible. In that case, it makes sense to move beyond leading order. Weak boson fusion (WBS) is an example, see Ref. [91], where the dimension six WCs are much better probed by diboson processes. This means the operators best constrained by Weak boson fusion (WBS) will be dimension eight. However, this is not the case for the processes we include in our analysis. So we consider only the leading order dimension six corrections.

In the physical observable (usually a cross-section or signal strength), these dimension six SMEFT operators appear in linear and quadratic terms, with respective powers of Λ^{-2} and Λ^{-4}. So there is another choice to be made: should one keep only the linear terms or both linear and quadratic terms? Implementing both leads to more complexity in deriving the SMEFT predictions and with interpreting of the analysis results. However, in our analysis we prefer to include them whenever possible for two reasons.

First, because this ensures the predictions of the physical observables (cross-section or signal strength) in the SMEFT always remain positive. Whereas, including only the linear terms allows for these predictions to be negative for certain values of the WCs. This is not desirable because it makes the prediction unphysical, which is quite a hard constraint that most global analyses codes are ill equipped to handle. This can result in bad numerical responses that are hard to control.

Second, the quadratic terms introduce interference between the WCs, and this helps the analysis converge by preventing flat directions. The authors of Ref. [38] explain it best:

> For rate observables that are positive-definite, the $n-1$-dimensional hyper-surface in the parameter space of n Wilson coefficients is always a compact manifold, like a hyper-ellipsoid. Including the quadratic terms does not reduce the dimension of the parameter space, it merely changes the topology of the likelihood function describing the combinations of Wilson coefficients that provide a certain level of agreement between predictions and data.

Some argue that one should not truncate the EFT expansion at the level of the Lagrangian, but at the level of the physical observable. For cross-sections and signal strengths, this would mean keeping all terms up to order Λ^{-4}, which include the dimension six quadratic terms, but also the dimension eight linear terms. Although this argument makes perfect sense from a mathematical standpoint, it leads to the same fitting problems we already discussed for the dimension six linear terms. So for our SMEFT analyses, we have decided to truncate at dimension six at the level of the Lagrangian.

For our SMEFT predictions, we include dimension six operators up to quadratic terms in the physical observables, wherever this is possible. The only predictions for which we stop at the linear level are electroweak precision observables (EWPO) measured by LEP, as the quadratic contributions have not yet been derived.

To sum up, as already stated in Ref. [1]:

The hypothesis based on a truncated Lagrangian is, strictly speaking, not well defined once we include higher multiplicities of the dimension-6 operators in the amplitude. Therefore, the SMEFT analysis should be interpreted as representing classes of models [92, 93], and the validity of the SMEFT approach rests on the process-dependent assumption that in the corresponding models no new particle is produced on its mass shell [94]. While SMEFT is an excellent framework to interpret a global LHC analysis, possible anomalies need to be interpreted by matching it to UV-complete models [95–98], where for instance WBS signatures of corresponding models might eventually require us to go beyond dimension six operators [91].

2.3.4 Restricting to process classes

Even taking into account the SMEFT operators only up to dimension six, and making simplifying assumptions regarding flavor, there remain too many of them to perform a global analysis with a reasonable amount of time and computing power.

This is where the classification of SMEFT operators and their corresponding Wilson coefficients (WCs), according to the processes they contribute to, comes in. These process classes group together operators that give corrections to a group of phenomenological processes. Examples include Higgs production and decay processes, electroweak (EW) processes and processes involving a top quark, which we will respectively call Higgs, EW, and top process classes.

We usually call a global analysis an attempt to constrain all—or at least the main— operators entering one process class or more. These global analyses are essential to determine bounds on the SMEFT WCs because many operators can influence a given process. So looking at the limits one process sets on a single WC makes little sense as one can only derive limits on one WC at a time by assuming values for the other WCs involved. When performing global analyses however, we are looking at how an entire class of processes constrains all WCs relevant to this class.

Ultimately, we also want to extend our global analyses to multiple process classes to determine the amount of cross-talk between them. Especially given that SMEFT operators can—and often will—contribute to more than one class of processes, which means there is no way to separate them into hermetic groups. In fact, 12 operators out of the 20 in our basis, defined in Tab. 2.4, contribute to more than one process class. For these operators at the frontier between classes, constraints may come mainly from one process class or a combination of them. This will be illustrated in more details in section Sec. 2.4.

Different groups have performed analyses for different combinations of process classes, as shown in Tab. 2.3.

Now that we have reviewed the main assumptions in our SMEFT analysis, we will define the basis for our analysis which will focus on Higgs and EW processes.

Groups	Process classes			
	Higgs	Electroweak	Top	Flavor
SFITTER	[1, 2, 36, 37]		[38]	
SMEFiT	[39]			
Fitmaker	[40]			
Dawson et al..	[41]			
Electroweak Legacy	[42, 43]			
EFTfitter				[44]
TopFitter			[45]	
HEPfit		[46]		
ATLAS	[32]			

Table 2.3: List of SMEFT global analyses performed by different groups classified by the combination of process classes considered.

2.4 Dimension six operator basis for Higgs and electroweak (EW) processes

The content of this section has been published in Refs. [1, 2]. A big part of the text and a table is identical to the content of these publications. We also supplement it with additional information.

Our dimension six SMEFT Lagrangian is then defined as

$$
\begin{aligned}
\mathcal{L}_{\text{eff}} = \mathcal{L}_{\text{SM}} &- \frac{\alpha_s}{8\pi}\frac{f_{GG}}{\Lambda^2}\mathcal{O}_{GG} + \frac{f_{BW}}{\Lambda^2}\mathcal{O}_{BW} + \frac{f_{BB}}{\Lambda^2}\mathcal{O}_{BB} + \frac{f_{WW}}{\Lambda^2}\mathcal{O}_{WW} \\
&+ \frac{f_B}{\Lambda^2}\mathcal{O}_B + \frac{f_W}{\Lambda^2}\mathcal{O}_W + \frac{f_{3W}}{\Lambda^2}\mathcal{O}_{3W} + \frac{f_{\phi 1}}{\Lambda^2}\mathcal{O}_{\phi 1} + \frac{f_{\phi 2}}{\Lambda^2}\mathcal{O}_{\phi 2} \\
&+ \frac{f_\mu m_\mu}{v\Lambda^2}\mathcal{O}_{e\phi,22} + \frac{f_\tau m_\tau}{v\Lambda^2}\mathcal{O}_{e\phi,33} + \frac{f_b m_b}{v\Lambda^2}\mathcal{O}_{d\phi,33} + \frac{f_t m_t}{v\Lambda^2}\mathcal{O}_{u\phi,33} \\
&+ \frac{f_{4L}}{\Lambda^2}\mathcal{O}_{4L} + \frac{f_{\phi e}^{(1)}}{\Lambda^2}\mathcal{O}_{\phi e}^{(1)} + \frac{f_{\phi d}^{(1)}}{\Lambda^2}\mathcal{O}_{\phi d}^{(1)} + \frac{f_{\phi u}^{(1)}}{\Lambda^2}\mathcal{O}_{\phi u}^{(1)} + \frac{f_{\phi Q}^{(1)}}{\Lambda^2}\mathcal{O}_{\phi Q}^{(1)} + \frac{f_{\phi Q}^{(3)}}{\Lambda^2}\mathcal{O}_{\phi Q}^{(3)} \\
&+ \frac{f_{tG}}{\Lambda^2}\mathcal{O}_{tG} + \text{invisible decays} .
\end{aligned}
\tag{2.3}
$$

It contains 20 independent WCs and is based on the HISZ basis [99] expanded with additional relevant operators. The branching ratio of the Higgs to invisible final states, BR_{inv}, is treated as a free parameter, to account for potential Higgs decays to a dark matter agent.

The operators are given in Tab. 2.4, where the field strengths are normalized as $\hat{B}_{\mu\nu} = ig' B_{\mu\nu}/2$ and $\hat{W}_{\mu\nu} = ig\sigma^a W_{\mu\nu}^a/2$. The covariant derivative acting on the Higgs doublet is $D_\mu = \partial_\mu + ig' B_\mu/2 + ig\sigma_a W_\mu^a/2$, where we adopt the '+' convention. We have also

$$\mathcal{O}_{GG} = \phi^\dagger \phi\, G^a_{\mu\nu} G^{a\mu\nu} \qquad\qquad \mathcal{O}_{BW} = \phi^\dagger \hat{B}_{\mu\nu} \hat{W}^{\mu\nu} \phi$$

$$\mathcal{O}_{BB} = \phi^\dagger \hat{B}_{\mu\nu} \hat{B}^{\mu\nu} \phi \qquad\qquad \mathcal{O}_{WW} = \phi^\dagger \hat{W}_{\mu\nu} \hat{W}^{\mu\nu} \phi$$

$$\mathcal{O}_{B} = (D_\mu\phi)^\dagger\, \hat{B}^{\mu\nu}\, (D_\nu\phi) \qquad\qquad \mathcal{O}_{W} = (D_\mu\phi)^\dagger\, \hat{W}^{\mu\nu}\, (D_\nu\phi)$$

$$\mathcal{O}_{3W} = \mathrm{Tr}\left(\hat{W}_{\mu\nu} \hat{W}^{\nu\rho} \hat{W}_\rho{}^\mu \right)$$

$$\mathcal{O}_{\phi 1} = (D_\mu\phi)^\dagger\, \phi\phi^\dagger\, (D^\mu\phi) \qquad\qquad \mathcal{O}_{\phi 2} = \tfrac{1}{2}\partial^\mu\left(\phi^\dagger\phi \right) \partial_\mu\left(\phi^\dagger\phi \right)$$

$$\mathcal{O}_{e\phi,22} = (\phi^\dagger\phi)\, \bar{l}_2 \phi\, e_2 \qquad\qquad \mathcal{O}_{e\phi,33} = (\phi^\dagger\phi)\, \bar{l}_3 \phi\, e_3$$

$$\mathcal{O}_{d\phi,33} = (\phi^\dagger\phi)\, \bar{q}_3 \phi\, d_3 \qquad\qquad \mathcal{O}_{u\phi,33} = (\phi^\dagger\phi)\, \bar{q}_3 \widetilde{\phi}\, u_3$$

$$\mathcal{O}_{4L} = \left(\bar{l}_1 \gamma_\mu l_2 \right)\left(\bar{l}_2 \gamma^\mu l_1 \right) \qquad\qquad \mathcal{O}^{(1)}_{\phi e} = (\phi^\dagger i \overset{\leftrightarrow}{D}_\mu \phi)\,(\bar{e}_i \gamma^\mu e_j)\, \delta^{ij}$$

$$\mathcal{O}^{(1)}_{\phi d} = (\phi^\dagger i \overset{\leftrightarrow}{D}_\mu \phi)\left(\bar{d}_i \gamma^\mu d_j \right) \delta^{ij} \qquad\qquad \mathcal{O}^{(1)}_{\phi u} = (\phi^\dagger i \overset{\leftrightarrow}{D}_\mu \phi)\,(\bar{u}_i \gamma^\mu u_j)\, \delta^{ij}$$

$$\mathcal{O}^{(1)}_{\phi Q} = (\phi^\dagger i \overset{\leftrightarrow}{D}_\mu \phi)\,(\bar{q}_i \gamma^\mu q_j)\, \delta^{ij} \qquad\qquad \mathcal{O}^{(3)}_{\phi Q} = (\phi^\dagger i \overset{\leftrightarrow}{D^A_\mu} \phi)\left(\bar{q}_i \gamma^\mu t^A q_j \right) \delta^{ij}$$

$$\mathcal{O}_{tG} = i g_s (\bar{Q}_3 \sigma^{\mu\nu} T^A u_{R,3})\, \widetilde{\phi}\, G^A_{\mu\nu}$$

Table 2.4: Basis of dimension-6 SMEFT operators adopted in our global analysis. Flavor indices are denoted by i, j and are implicitly contracted when repeated.

defined $(\phi^\dagger i \overset{\leftrightarrow}{D}_\mu \phi) = i\phi^\dagger (D_\mu\phi) - i(D_\mu\phi^\dagger)\phi$, $(\phi^\dagger i \overset{\leftrightarrow}{D}{}^I_\mu \phi) = i\phi^\dagger \sigma^A (D_\mu\phi)/2 - i(D_\mu\phi^\dagger)\sigma^A \phi/2$ and the dual Higgs field $\widetilde{\phi} = i\sigma^2 \phi^\star$.

To construct the Lagrangian of Eq. (2.3), we use the operator basis of Refs. [36, 100], starting with a set of P-even and C-even operators and then using the equations of motion to define a basis without blind directions in the electroweak precision data. We neglect operators that can not be studied at the LHC yet, like those changing the triple-Higgs vertex [101–105]. We also neglect operators which are too strongly constrained from other LHC measurements to affect the Higgs-electroweak analysis, like the ubiquitous triple-gluon operator

$$\mathcal{O}_{G} = f_{ABC} G^\rho_{A\nu} G^\nu_{B\lambda} G^\lambda_{C\rho}\,, \tag{2.4}$$

which is strongly constrained from multi-jet production [106]. Thus, in the bosonic sector the relevant operators are $\mathcal{O}_{GG}$, $\mathcal{O}_{BW}$, $\mathcal{O}_{BB}$, $\mathcal{O}_{WW}$, $\mathcal{O}_{B}$, $\mathcal{O}_{W}$, $\mathcal{O}_{3W}$, $\mathcal{O}_{\phi 1}$, and $\mathcal{O}_{\phi 2}$.

In addition to the purely bosonic operators, we also need to include single-current operators modifying the Yukawa couplings, $\mathcal{O}_{e\phi,22}$, $\mathcal{O}_{e\phi,33}$, $\mathcal{O}_{u\phi,33}$, and $\mathcal{O}_{d\phi,33}$. These terms break the $U(3)^5$ completely flavor symmetric assumption. However, they always appear in the Lagrangian of Eq. (2.3) with a factor of the fermion mass, which is proportional to the Yukawa. So they abide by our Minimal Flavor Violation (MFV) assumption.

The main difference to earlier SFITTER analyses is that we treat the correction to the muon Yukawa f_μ as an independent parameter, while previously it was tied to f_τ via an approximate flavor symmetry. As LHC Run 2 found experimental evidence for the Higgs coupling to muons, this approximation can now be dropped. However, when including the observed branching ratio to muons, we will not be sensitive to the sign of the muon

Yukawa, except for the fact that such a sign flip is not consistent with the SMEFT assumptions.

The four-lepton operator $\mathcal{O}_{4L}$, for which we only retain the (1221) contraction, induces a shift in the Fermi constant.

Other single-current operators modify gauge and gauge-Higgs ($HVff$) couplings [42, 107–113] $\mathcal{O}_{\phi e}^{(1)}$, $\mathcal{O}_{\phi d}^{(1)}$, $\mathcal{O}_{\phi u}^{(1)}$, $\mathcal{O}_{\phi Q}^{(1)}$, and $\mathcal{O}_{\phi Q}^{(3)}$. For these operators, we maintain for simplicity a $U(3)^5$-invariant flavor structure, and all currents are implicitly defined with diagonal flavor indices. In this limit, the operators $\mathcal{O}_{\phi L}^{(1)}, \mathcal{O}_{\phi L}^{(3)}$, analogous to $\mathcal{O}_{\phi Q}^{(1)}, \mathcal{O}_{\phi Q}^{(3)}$, are redundant with the bosonic set via equations of motion [36, 100].

Dipole operators and $\mathcal{O}_{\phi ud,ij}^{(1)} = \tilde{\phi}^\dagger(i\, D_\mu \phi)(\bar{u}_{R,i}\gamma^\mu d_{R,j})$ are neglected for two reasons: the approximate flavor symmetry requires them to scale with the SM Yukawa couplings and their interference with the SM is always proportional to the fermion masses. Both factors suppress their effects except for the top quark. The three dipole moments of the top quark—electric, magnetic and chromomagnetic—are not suppressed, so in this work we choose to retain the chromomagnetic operator [42, 114–116] $\mathcal{O}_{tG}$. It affects the Higgs observables at the LHC significantly through the loop-induced production process [39, 40, 117–119].

Table 2.5 shows which of the operators defined in Tab. 2.4 belong to which sector. Note that we take into account all the operators which yield SMEFT corrections to Higgs processes only (7), the single operator which affects EW processes only ($\mathcal{O}_{3W}$) and all the operators at the intersection between these two sectors (10). To this we add two operators at the intersection between the Higgs and the top sectors: $\mathcal{O}_t$ and $\mathcal{O}_{tG}$. The first one because it is expected to be well constrained by Higgs processes. The second one, however, even though constrained by Higgs processes, would lead to a blind direction with $\mathcal{O}_{GG}$ unless one adds in constraints from the top sector, which is what we do in Sec. 4.3.5.

What we do not include in our basis are operators affecting only top processes and those contributing to EW and top processes, but not Higgs processes. This is because we expect these operators to be primarily constrained by top processes, which we do not include in the analysis. We also exclude the third operator at the intersection between the top and Higgs processes: the triple-gluon operator $\mathcal{O}_G$ defined in Eq. (2.4). The reason being that this operator is much better constrained by non-Gauge and non-top processes, as we already mentioned.

Additionally, for the global analysis it is convenient to work with the two orthogonal combinations

$$\mathcal{O}_\pm = \frac{\mathcal{O}_{WW} \pm \mathcal{O}_{BB}}{2} \qquad \Rightarrow \qquad f_\pm = f_{WW} \pm f_{BB}\,. \tag{2.5}$$

The rotation is defined such that only $\mathcal{O}_+$ contributes to the $H\gamma\gamma$ vertex.

If we base our calculation on the Lagrangian given in Eq.(2.3), we strictly speaking need to supplement it with a renormalization scheme or a renormalization condition. For each process, a reasonable assumption is that all Lagrangian parameters, including the WCs, are evaluated at the same renormalization scale μ_R. For the processes entering our global analysis, an appropriate central scale choice is $\mu_R \in [m_H/2, m_H]$. To improve the precision beyond leading order, one should eventually account for the renormalization

Operators	Process classes		
	Higgs	Electroweak	Top
$\mathcal{O}_{GG}$	✓		
$\mathcal{O}_{BW}$	✓	✓	✓
$\mathcal{O}_{BB}$	✓		
$\mathcal{O}_{WW}$	✓		
$\mathcal{O}_B$	✓	✓	
$\mathcal{O}_W$	✓	✓	
$\mathcal{O}_{3W}$		✓	
$\mathcal{O}_{\phi 1}$	✓	✓	✓
$\mathcal{O}_{\phi 2}$	✓		
$\mathcal{O}_{e\phi,22}$	✓		
$\mathcal{O}_{e\phi,33}$	✓		
$\mathcal{O}_{d\phi,33}$	✓		
$\mathcal{O}_{u\phi,33}$	✓		✓
$\mathcal{O}_{4L}$	✓	✓	✓
$\mathcal{O}_{\phi e}^{(1)}$	✓	✓	
$\mathcal{O}_{\phi d}^{(1)}$	✓	✓	✓
$\mathcal{O}_{\phi u}^{(1)}$	✓	✓	✓
$\mathcal{O}_{\phi Q}^{(1)}$	✓	✓	✓
$\mathcal{O}_{\phi Q}^{(3)}$	✓	✓	✓
$\mathcal{O}_{tG}$	✓		✓

Table 2.5: Process classes of the dimension six SMEFT operators in our basis.

group evolution [83], and evaluate the SMEFT predictions at the energy scale appropriate for each process. This scale can vary for instance across bins of a kinematic distribution. In this work, all SMEFT predictions are calculated at leading order, so we postpone an in-depth analysis of renormalization group effects to a future work, together with a systematic study of the impact of higher-order corrections to inclusive Higgs production and decay rates.

Now that we have established the basis for our global SMEFT analyses, we will give more technical details regarding how the analyses are performed using the SFITTER tool.

SFitter: a tool for SMEFT global analyses and beyond

SFITTER [120] is a multi-purpose analysis tool used for SMEFT [1, 36–38, 50, 104] and UV model analyses [2], but also SUSY dark matter [121–126], as well as Higgs searches [127–129].

The basic principle behind a likelihood analysis is to compare the prediction of a given process with a measurement of that process in order to determine the likelihood. The prediction is computed for one point in the parameter space of a chosen model. The measurement is implemented with its corresponding uncertainties, which follow certain probability distributions. Through the link between probability distributions and likelihoods, which we will establish again in Sec. 3.1, one obtains the value of the likelihood at the model parameter point given the measured value and uncertainties of the process. If one wants to take more than one measurement into account, one then needs to combine the individual likelihoods.

Then this likelihood computation has to be repeated for many points until a map of the likelihood as a function of the model parameters is obtained. This means one needs an efficient way to sample the likelihood function around the region of interest, i.e. around the maximum likelihood point. In our case we will use Monte Carlo Markov chains (MCMC). Using the likelihood map, we can finally determine the limits on the model parameters.

In what follows, we will first explain how likelihoods are computed within SFITTER in Sec. 3.1. Then we will describe the method used to map the likelihood over the relevant parameter region in Sec. 3.2. These first two components will be general to any model. After that we specialize to SMEFT global analyses and discuss the implementation of the measurements and SMEFT predictions for Higgs and EW processes, in Sec. 3.3. Finally, we will show how one can make the results of the global SMEFT analysis work double time by constraining UV models. Sec. 3.4 will describe this UV interface in more details.

3.1 Computing the likelihood at a point

We start from the conditional probability density function (PDF) $p(d|m)$ to measure the data d given the model m. We know that repeating the measurement enough times

will yield the density function $p(d|m)$ and that it is normalised if we integrate over the random variable d:

$$\int_d p(d|m) = 1 \,, \tag{3.1}$$

However, there is another way to view this conditional PDF once the measurement has already been performed. Indeed if the data d is fixed, $p(d|m)$ can be recast as the likelihood of the model m:

$$\mathcal{L}(m) = \mathcal{L}(m|d) = p(d|m) \,. \tag{3.2}$$

The likelihood is a function of the model m and is not normalised to 1. Computing the likelihood is a way to measure the level of agreement between the measured data d and the model m.

In what follows, we will go into more details regarding likelihoods. We will first see, in Sec. 3.1.1, the different likelihood function which stem from Gaussian, flat and Poisson distributions. Then in Sec. 3.1.2, we will present how likelihoods should be combined for the profiling and marginalization treatments.

3.1.1 Different probability density functions (PDFs), different likelihoods

It is particularly important to treat uncertainties on the measurement correctly. For this reason, in SFITTER we take into account different types of PDFs. It is easy to understand that each one will, in turn, correspond to a different likelihood function. Concretely, we consider three types of PDFs: Gaussian, flat and Poisson distributions. We will present each one here, following [9].

Depending on the PDF, the data d will be best described either by a continuous random variable $-\infty < x < \infty$, measured with expected value μ and additional parameter σ, or by a discontinuous random variable $n = 0, 1, 2, ...$, measured with expected value ν.

The likelihood derived from a Gaussian PDF is given by

$$\mathcal{L}(\mu, \sigma|x) = p(x|\mu, \sigma) = \mathcal{N}_{\mu,\sigma}(x) = \frac{1}{\sqrt{2\pi}\sigma} \exp \frac{-(x-\mu)^2}{2\sigma^2} \,. \tag{3.3}$$

The likelihood which stems from a flat PDF is given by

$$\mathcal{L}(\mu, \sigma|x) = p(x|\mu, \sigma) = \mathcal{F}_{\mu,\sigma}(x) = \frac{1}{2\sigma}\Theta(x - (\mu - \sigma))\Theta((\mu + \sigma) - x) \,. \tag{3.4}$$

Finally, we consider the likelihood generated by a Poisson PDF

$$\mathcal{L}(\nu|n) = p(n|\nu) = \text{Pois}(n|\nu) = \frac{\nu^n e^{-\nu}}{n!} \,, \ \nu > 0 \,. \tag{3.5}$$

3.1.2 Combining likelihoods: profiling versus marginalization

Both the profiling and marginalization treatments start from the same exclusive likelihood, which is a function of the model parameters f_x, the nuisance parameters for systematic θ_{syst} and theory θ_{theo} uncertainties, and the expected background b. First, we will show

how this exclusive likelihood is constructed for a single channel. Then we generalize it to multiple channels.

The exclusive likelihood for one channel is constructed by taking the product of the individual likelihoods that constrain the parameters:

$$
\begin{aligned}
\mathcal{L}_{\text{excl}}(f_x, \theta_{\text{syst}}, \theta_{\text{theo}}, b) = {} & \text{Pois}(d|m(f_x, \theta_{\text{syst}}, \theta_{\text{theo}}, b)) \\
& \times \text{Pois}(b_{\text{CR}}|b\,k) \prod_i \mathcal{N}_{\theta_{\text{syst},i},\,\sigma_i}(0) \prod_j \mathcal{F}_{\theta_{\text{theo},j},\,\sigma_j}(0) \,.
\end{aligned}
\tag{3.6}
$$

The first factor on the r.h.s. of Eq. (3.6) represent the likelihood expected from the model as a function of the parameters $m(f_x, \theta_{\text{syst}}, \theta_{\text{theo}}, b)$ given the observed data d. The second gives the likelihood of the expected background b, given the observed value for this background in a control region (CR) b_{CR} and the interpolation factor k between the CR and the signal region (SR). Both of these likelihoods are well described by a Poisson distribution. The last two factors represent the likelihoods of the nuisance parameters for systematic θ_{syst} and theory θ_{theo} uncertainties given that they should be centered around zero with given half-widths σ. In SFITTER, these likelihoods are assumed to follow Gaussian distributions for systematic uncertainties and flat distributions for theory uncertainties.

In the context of Bayesian marginalization, the second line of Eq. (3.6) can be understood as priors encoding our prior knowledge or belief on the expected background b and the nuisance parameters θ_{syst} and θ_{theo}. While for a profile likelihood, these should be understood as PDFs constructed from auxiliary measurements (or imaginary measurements in the case of the nuisance parameters θ_{syst} and θ_{theo}).

Likelihoods of a set of measurements can simply be multiplied. Thus, combining channels to generalize Eq. (3.6) to a set of N channels simply is accomplished by replacing

$$
\begin{aligned}
\text{Pois}(d|m)\text{Pois}(b_{\text{CR}}|b\,k) \quad &\longrightarrow \quad \prod_l \text{Pois}(d_l|m_l)\text{Pois}(b_{\text{CR}_l}|b_l\,k_l) \\
\mathcal{N}_{\theta_{\text{syst},i},\sigma_i}(0) \quad &\longrightarrow \quad \mathcal{N}_{\vec{\theta}_{\text{syst},i},\Sigma_i}(\vec{0}) \\
\mathcal{F}_{\theta_{\text{theo},j},\sigma_j}(0) \quad &\longrightarrow \quad \prod_l \mathcal{F}_{\theta_{\text{theo},lj},\sigma_{lj}}(0) \,.
\end{aligned}
\tag{3.7}
$$

These replacements assume that the theory uncertainties are uncorrelated[1], while the systematics can be correlated. For this, we introduce an N-dimensional Gaussian with the covariance matrices Σ_i encoding the correlations between uncertainties of category i entering different channels l. We use either uncorrelated or fully correlated systematics.

From the exclusive likelihood given in Eq. (3.6) and generalized to multiple channels via Eq. (3.7), one can then construct the marginal and profiled likelihoods. The marginal likelihood is obtained by integrating over nuisance parameters θ_{syst} and θ_{theo} and the expected background b

$$
\mathcal{L}_{\text{marg}}(f_x) = \int \prod_i d\theta_{\text{syst},i} \int \prod_j d\theta_{\text{theo},j} \int db \, \mathcal{L}_{\text{excl}}(f_x, \theta_{\text{syst}}, \theta_{\text{theo}}, b) \,,
\tag{3.8}
$$

---

[1] In past SFITTER analyses, the theory uncertainties were sometimes taken to be fully correlated across bins, see Ref. [37]. More recently in Refs. [1, 2, 36], this assumption was dropped because it lead to a higher dimensionality of the analysis, which is computationally expansive. We checked that this change did not impact the results significantly.

while the profiled likelihood is obtained by taking the maximum over the same parameters.

$$\mathcal{L}_{\text{prof}}(f_x) = \max_{\theta_{\text{syst}}, \theta_{\text{theo}}, b} \mathcal{L}_{\text{excl}}(f_x, \theta_{\text{syst}}, \theta_{\text{theo}}, b) \,. \tag{3.9}$$

Although in theory the only difference between the profiling and marginalization treatments resides in the profiling and marginalization procedures shown in Eqs. (3.8) and (3.9), in practice we have to make additional assumptions to compute these profiled and marginal likelihoods in a numerically efficient way. For example, although many of the integrals in Eq. (3.8) can be solved analytically, marginalizing over an exclusive likelihood combining N channels still requires the numerical integration of a N-dimensional integral. We choose to perform this integral using the Laplace method. This and other assumptions made in SFITTER for the new marginalization treatment, will be presented in greater details in Chap. 4. In what follows, we will briefly present what happens in SFITTER when profiling over the exclusive likelihood. More details can be found in Refs. [130, 131].

Profiling: additional combining assumptions

The exclusive likelihood in Eq. (3.6) multiplies together two Poisson likelihoods for the data and the background, as well as several flat and Gaussian likelihoods. The next step is to profile over the expected background and all the nuisance parameters, following Eq. (3.9). The problem is the profiling step can not be performed analytically, because the two Poisson likelihoods can not be combined analytically with the Gaussian likelihoods. Furthermore, profiling numerically over so many nuisance parameters (we usually consider more than 30 systematic uncertainties and up to 15 theory uncertainties) would be too computationally expensive.

This means we need to take an alternative approach that combines the likelihoods analytically whenever possible, and uses heuristic formulae (which would be exact for the fully Gaussian case) otherwise. What follows is a brief overview of this scheme and the assumptions taken within SFITTER.

Profiling over all but one systematic nuisance parameters   In this scheme, the hardest thing to deal with are the systematic Gaussian uncertainties. We first want to combine all of them into a total Gaussian likelihood, neglecting the correlations between different channels. The correlations will be re-introduced at a later point through a heuristic formula.

For a single channel with data d, model prediction m and expected background b, we first focus on the part of the likelihood made of all the Gaussian likelihoods. Profiling this part of the likelihood over all but one of the systematic nuisance parameters also yields a Gaussian likelihood, with a systematic nuisance parameter $\theta_{\text{syst,tot}}$. Because the categories i are independent, the total systematic uncertainty on this channel is then given by the sum squared of the individual uncertainties: $\sigma_{\text{syst,tot}}^2 = \sum_i \sigma_i^2$. However, the individual uncertainty per category σ_i needs to be expressed in terms of the uncertainties on the data and expected background for this category, $\sigma_{i,d}$ and $\sigma_{i,b}$ respectively. Taking the data and expected background as fully correlated, the total systematic uncertainty for a single channel is: $\sigma_{\text{syst,tot}}^2 = \sum_i (\sigma_{i,d} - \sigma_{i,b})^2$. Such that the log-likelihood combining

all the Gaussian systematic uncertainties on the signal (defined as $d - b$) for a single channel is given by

$$-2 \log \mathcal{L}(m - b | d - b, \sigma_{\text{syst,tot}}) = -2 \log \frac{\mathcal{N}_{(m-b),\sigma_{\text{syst,tot}}}(d - b)}{\mathcal{N}_{0,\sigma_{\text{syst,tot}}}(0)} = \frac{(d - m)^2}{\sum_i (\sigma_{i,d} - \sigma_{i,b})^2} \, , \quad (3.10)$$

where we normalize the likelihood $\mathcal{L}(m - b | m - b, \sigma_{\text{syst,tot}}) = 1$.

Next, we extend this formula to multiple channels following the prescriptions in Eq. (3.7), still neglecting the correlations between channels. This amounts to considering only the diagonal entries of the covariance matrices $\Sigma_{i,d}$ and $\Sigma_{i,b}$ for the uncertainties on the data and expected background in each category i. For a given channel l, the total systematic uncertainty is then $\Sigma_{\text{syst,tot}}^{ll} = \sum_i (\sqrt{\Sigma_{i,d}^{ll}} - \sqrt{\Sigma_{i,b}^{ll}})^2$ and the log-likelihood becomes

$$\frac{(d - m)^2}{\sigma_{\text{syst,tot}}^2} = \frac{(d - m)^2}{\sum_i (\sigma_{i,d} - \sigma_{i,b})^2} \quad \longrightarrow \quad \frac{(d_l - m_l)^2}{\Sigma_{\text{syst,tot}}^{ll}} = \frac{(d_l - m_l)^2}{\sum_i (\sqrt{\Sigma_{i,d}^{ll}} - \sqrt{\Sigma_{i,b}^{ll}})^2} \, . \quad (3.11)$$

Profiling over the expected background b and the last systematic nuisance parameter
We then need to combine the two Poisson likelihoods together with the total Gaussian likelihood derived previously. No analytical formula exist for this combination. So we rely on a heuristic formula, which is exact in the limit where the two Poisson likelihoods can be approximated by Gaussian likelihoods. This has also been shown to give reasonable results when we are not in this fully Gaussian limit [130]. The heuristic formula is obtained by summing the normalised inverse log-likelihoods together

$$\frac{1}{\log \mathcal{L}(m)} \approx \frac{1}{\log \frac{\text{Pois}(d|m)}{\text{Pois}(m|m)}} + \frac{1}{\log \frac{\text{Pois}(b_{\text{CR}} | (d-m)k + b_{\text{CR}})}{\text{Pois}((d-m)k + b_{\text{CR}} | (d-m)k + b_{\text{CR}})}} + \frac{1}{\log \frac{\mathcal{N}_{(m-b),\sigma_{\text{syst,tot}}}(d-b)}{\mathcal{N}_{0,\sigma_{\text{syst,tot}}}(0)}} \, ,$$
$$(3.12)$$

instead of profiling over the expected background b and the total systematic nuisance parameter $\theta_{\text{syst,tot}}$. Note that the value of the model m, which depends on the expected background b, is evaluated at $b = \frac{b_{\text{CR}}}{k}$.

Profiling over theory nuisance parameters The flat likelihoods and their nuisance parameters θ_{theo} representing theory uncertainties remain. For each channel, we first combine all the flat likelihoods into one total flat likelihood (by profiling over all but one of the theory nuisance parameters). The uncertainty for this total flat likelihood is then given by the sum of the individual flat uncertainties $\sigma_{\text{theo,tot}} = \sum_j \sigma_j$ and we call the remaining theory nuisance parameter $\theta_{\text{theo,tot}}$.

Finally, we need to combine the approximate formula for the likelihood of two Poisson likelihoods and the total Gaussian likelihood given in Eq. (3.12) with the total flat likelihood derived previously. This is done by profiling over the last theory nuisance parameter $\theta_{\text{theo,tot}}$. The result of this step is simple: the final likelihood is flat and normalized to 1 for $|d - m| \leq \sigma_{\text{theo,tot}}$, otherwise the likelihood is given by Eq. (3.12) where the model m is shifted towards the data d by an amount $\sigma_{\text{theo,tot}}$.

This part of the procedure is inspired by the RFit scheme [132].

Re-introducing systematic correlations between channels   The previous steps have given us a profiled likelihood $\mathcal{L}_l$ for each individual channel l, which can also be converted to a value of

$$\chi_l^2 = -2 \log \mathcal{L}_l \,. \tag{3.13}$$

So far, we have neglected correlations between channels. It is time to re-introduce them considering a correlation matrix C between channels and $\vec{\chi}$ (such that $\chi_l = \sqrt{\chi_l^2}\,\mathrm{sign}\,(d_l - m_l)\,$) for individual channels. Similarly to Eq. (3.13), the profiled likelihood correlating all channels is given by

$$-2 \log \mathcal{L} = \vec{\chi}^T C^{-1} \vec{\chi} \,. \tag{3.14}$$

Again, this is a heuristic formula which is exact in the limit where both Poisson likelihoods can be approximated by Gaussian likelihoods. Considering the fully Gaussian limit, the correlation matrix C is 1 for the diagonal entries and can be rewritten as a function of the covariance matrices per category Σ_i for the off-diagonal entries

$$C_{ln} = \frac{\sum\limits_i \Sigma_i^{ln}}{\sigma_{l,\exp}\,\sigma_{n,\exp}} = \frac{\sum\limits_i \sqrt{\Sigma_i^{ll}}\,\sqrt{\Sigma_i^{nn}}\,\rho_{i,ln}}{\sigma_{l,\exp}\,\sigma_{n,\exp}} \,, \tag{3.15}$$

where $\rho_{i,ln}$ is 1^2 if the category i is fully correlated and the channels l and n were measured by the same experiment, otherwise we assume no correlation and $\rho_{i,ln}$ is 0. The quantity $\sigma_{l,\exp}$ is also defined in terms of the covariance matrices per category Σ_i

$$\begin{aligned} \sigma_{l,\exp}^2 &= \Sigma_{\mathrm{syst,tot}}^{ll} + \sigma_{\mathrm{Pois},d}^2 + \sigma_{\mathrm{Pois},b}^2 \\ &= \sum_i (\sqrt{\Sigma_{i,d}^{ll}} - \sqrt{\Sigma_{i,b}^{ll}})^2 + d + \frac{b_{\mathrm{CR}}}{k} \,. \end{aligned} \tag{3.16}$$

3.2 Mapping the likelihood

We are interested in mapping the profiled and marginal likelihoods in the region around their respective best fit point, i.e. the point with the highest likelihood. This is because we can extract information from these maps, such as 68% and 95% confidence level (CL) limits, as we will explain in Sec. 3.2.3.

To get this map and constrain the analysis parameters, we need two essential ingredients. The first is a way to compare two likelihood points, i.e. a statistical test. As we will see in Sec. 3.2.1, the most efficient test is the likelihood ratio. Second, we require a way to efficiently sample the parameter space around the maximum likelihood point. For this we use Monte Carlo Markov chains (MCMC), presented in Sec. 3.2.2.

3.2.1 Statistical test: the likelihood ratio

In order to compare two models or hypotheses, we need a statistical test. This is a measure of the goodness of fit of the test model m_{test} compared to a reference model m_0 given the data d. In our case, we choose the likelihood ratio, which has been proven by

---

[2]In practice, we take $\rho_{i,ln} = 0.99$ because for $\rho = 1$ the correlation matrix C is not invertible.

Neyman and Pearson [133] to be the most efficient statistical test to distinguish between the zero hypothesis m_0 and a test hypothesis m_test:

$$t(m) = \frac{\mathcal{L}(m_\text{test}|d)}{\mathcal{L}(m_0|d)} \,. \tag{3.17}$$

When setting limits, the zero hypothesis or reference model is taken as the best fit point $m_0 = m_\text{best}$, such that $\mathcal{L}(m_\text{best}|d) = \max_m \mathcal{L}(m|d)$. Whereas, when used in a MCMC algorithm, the zero hypothesis is taken to be the model point the chain is currently at, $m_0 = m_\text{current}$.

3.2.2 Monte Carlo Markov chains (MCMC)

We want an efficient way to map the parameter space around the highest likelihood point. We choose Monte Carlo Markov chains (MCMC): sequences of points in the parameter space, such that the next point in a chain is determined through a statistical test against the current point only.

More precisely, a test point m_test is sampled from a probability distribution—flat, Breit-Wigner or Gaussian—centred on the current point m_current. Then, we compare the likelihood of the current point $\mathcal{L}(m_\text{current}|d)$ with that of the test point $\mathcal{L}(m_\text{test}|d)$ through the likelihood ratio defined in Eq. (3.17). If

$$\frac{\mathcal{L}(m_\text{test}|d)}{\mathcal{L}(m_\text{current}|d)} > 1 \,, \tag{3.18}$$

the test point is accepted as the next point in the chain, $m_\text{next} = m_\text{test}$. If the likelihood of the test point is smaller than the one of the current point, however, the test point is accepted as next point only if

$$\frac{\mathcal{L}(m_\text{test}|d)}{\mathcal{L}(m_\text{current}|d)} \geq r \,, \tag{3.19}$$

with $r \in [0, 1]$ a random number drawn from a uniform distribution. Otherwise, the test point is rejected and the next point on the chain is chosen identical to the current point, $m_\text{next} = m_\text{current}$.

This algorithm is called the Metropolis algorithm [134] and it ensures that the probability of the test point to be selected is

$$\min\left(1, \frac{\mathcal{L}(m_\text{test}|d)}{\mathcal{L}(m_\text{current}|d)}\right) \,. \tag{3.20}$$

Since the test point is drawn randomly around the current point, and as the chain favors points with higher likelihood, a MCMC is constructed to map the region of highest likelihood well. On the other hand, it still provides the possibility to accept points with lower likelihoods, which is essential when mapping regions with complex likelihood shapes (such as likelihoods with multiple maxima). Additionally, this method scales linearly[3] with the dimension of the parameter space, which makes it computationally less expensive than other methods, e.g. using a grid.

---

[3]It scales linearly if the parameters of the random distribution used for sampling are appropriately tuned.

Our MCMC also requires a burn-in phase, which ensures that the influence of initial conditions is suppressed. The way to do that is to simply delete the start of the chain up to a certain percentage of points. We choose to cut out the first 1% of the chain when mapping a profiled likelihood and the first 10% when mapping a marginal one. This burn-in phase is especially important for the marginalization treatment. Indeed, because this procedure requires integrating over parameters, an accurate representation of the density of points in the parameter space is essential to compute the marginal likelihood.

3.2.3 Limits on the parameters

Once we have a map of the profiled and marginal likelihoods (defined in Eqs. (3.8) and (3.9)), the goal is to extract limits on the Wilson coefficients (WCs). The first step is to profile (i.e. maximize), respectively marginalize (i.e. integrate), over all WCs except the one or two we want to constrain. The ways to derive the intervals from there is different for each treatment.

First, we discuss the procedure for a profiled likelihood. The proper way to derive these intervals is to use the Feldman-Cousins method, which is based on Neyman's construction with the likelihood ratio as an ordering rule or test statistics. However, this is a very cumbersome approach that very few people use. Most people prefer likelihood-based intervals, and that is how we construct our profiled intervals. These make use Wilks' theorem [135], which states that $-2 \log t(m)$ (where $t(m)$ is the likelihood ratio defined in Eq. (3.17)) follows a χ^2 distribution, if the data d has a large enough sample size. Consequently, setting limits on a χ^2 distribution is easy. One just has to look for parameter values for which the χ^2 value exceeds a certain threshold. The threshold depends the number of degrees of freedom (DOF) and the confidence level (CL) limit one is trying to set. The values we will use are given in Tab. 3.1.

The procedure is a bit different for a marginal likelihood. We first need to identify the maximum, and integrate around that point keeping the likelihood values on the borders of the integral the same. If additional peaks exists, we compute the integral for the part of the curve above a given likelihood threshold. We stop the integral and read the limits when the value of the integral (i.e. the area under the curve) exceeds 68% or 95% of the full integral.

The first procedure results in confidence intervals and the second in credible intervals. These two types of intervals have, in principle, different statistical interpretations and are, therefore, not required to match. Note that we sometimes use this second procedure to set limits on the profiled likelihood as well, for better comparison between the two methods.

	68%CL	95%CL
1 DOF	0.989	3.841
2 DOF	2.279	5.991

Table 3.1: χ^2 value setting the 68% or 95%CL limits on a distribution with 1 or 2 DOF.

3.3 Global SMEFT analysis for Higgs and EW processes

Up until this point, the computation and mapping of the likelihood were kept very general and applicable to any model constrained by data from various counting experiments considering Poisson, Gaussian or flat uncertainties. In this section, we specialize to mapping the likelihood for a specific model—the SMEFT— given data from a few relevant experiments—ATLAS, CMS, and LEP. As already discussed in Chap. 2, the SMEFT parameter space is vast and we only consider a 21-dimensional subspace given by the Lagrangian in Eq. (2.3). In Sec. 3.3.1 we present, the specific processes which enter in our analysis and constrain the parameter space. Then in Sec. 3.3.2, we discuss how the SMEFT predictions are implemented within SFITTER.

3.3.1 Measurements implementation

Higgs processes

We consider processes involving the five main Higgs production channels (gluon-fusion (ggF), vector boson fusion (VBF), as well as WH, ZH, and $t\bar{t}H$ associated production) and decaying through the most prominent decay channels ($b\bar{b}$, W^+W^-, gg, $\tau^+\tau^-$, ZZ particularly $ZZ^{(*)} \to 4l$, $\gamma\gamma$, $Z\gamma$, and $\mu^+\mu^-$). Additionally, we consider the case where the Higgs decays to invisible final states, such as dark matter particles.

We omit the decay into $c\bar{c}$ because the constraints on this decay channel are poor. It is not expected to be observed even at high-luminosity LHC (HL-LHC) [136]. We note that a few measurements also constrain associated $b\bar{b}H$ production, but none in the latest updates.

The values for (or constraints on) these processes mainly stem from rate or signal strengths measurements by the ATLAS and CMS experiments, taken with partial or complete data from Run 1 or Run 2 of the LHC. These are generally low-kinematic measurements in the sense that they mainly constrain the bulk of the distribution of interest. This means that in turn they mostly constrain non-kinematically enhanced operators and the better constraints come from higher precision in the measurement.

We also include a few high-kinematic measurements for VH associated production. These searches target the high-kinematic region of the relevant invariant mass distributions and are used to constrain kinematically enhanced WCs, such as $f_{\phi Q}^{(3)}$, $f_{\phi u}^{(1)}$, f_W, f_{BB}, etc. We note that the best constraints on those kinematically enhanced operators might not always come from the highest bin in the distribution, as precision in these highest bins is often low. Instead, the best constraints might come from slightly less energetic bins, that have both some kinematic enhancement in the SMEFT coefficients and a reasonable precision.

EW processes

EW processes encompass diboson VV production at the LHC with electroweak precision observables (EWPO) from LEP and a combined fit of the Particle Data Group.

The diboson measurements are always implemented as kinematic distributions. Some target the low-kinematic regions and others the high-kinematic regions.

The EWPO are a set of 15 observables. 12 *Z*-pole observables are taken from the final LEP results [137]: the total width of the *Z* peak as well as partial width to leptons, charm and bottom quarks, forward-backward asymmetries, the lepton neutral current asymmetry from τ polarization and the hadronic pole cross-section. The remaining three observables are *W*-pole observables from the Particle Data Group [138]: the mass, width of the peak, and the branching ratio to leptons and neutrinos. These are low-kinematic measurements which primarily constrain the following operators: f_{BW}, $f_{\phi 1}$, f_{4L}, and $f_{\phi e}^{(1)}$—although more coefficients contribute to these observables, they are usually better constrained by other measurements.

Uncertainties

For the electroweak precision observables (EWPO), we consider only Gaussian uncertainties: uncorrelated statistical Gaussian uncertainty on individual measurements and Gaussian uncertainties correlating the 15 observables together.

For the LHC measurements (Higgs and diboson processes), we usually consider statistical systematic and theory uncertainties. The statistical uncertainties on rate measurements are implemented using Poisson distributions for both the data and background. While for signal strengths measurements we assume the statistical uncertainty follows an uncorrelated Gaussian distribution. For systematic uncertainties, we always use Gaussian uncertainties and we assume either 100% correlation or no correlation between the measurements of a given experiment. The categories of systematic uncertainties we take as fully correlated correspond to uncertainties on the luminosity, detector effects (such as pile-up or jet uncertainties), lepton or photon reconstruction, *b*- or τ-tagging, and lepton isolation. We take as uncorrelated any systematic uncertainty cited by the experiment which does not fit into the predefined correlated categories. Finally, the theory uncertainties are assumed to follow flat uncorrelated distributions. These come from both theory uncertainties on the measurement quoted by the experiment and theory uncertainties on our SMEFT prediction.

3.3.2 SMEFT predictions

All our SMEFT predictions are implemented for the basis given in Eq. (2.3). Note that when computing these predictions we make a big assumption: that the SMEFT only affects the signal and not any of the backgrounds. This is clearly a big caveat that most SMEFT global analyses have to adhere to, otherwise the predictions would become incredibly complicated to derive.

Rates and signal strengths measurements of Higgs processes

Rates and signal strengths measurements of various Higgs production and decay channels are used. For this type of measurement, the predictions were already implemented in Refs. [36, 37] for Run 1 and 2 respectively (assuming standard cuts targeting the bulk of the distribution) at quadratic order in our dimension six SMEFT basis. Exact SMEFT predictions were used wherever available, and the rest were computed using `Madgraph5` [139].

Distributions for VV and VH

Distributions are used for diboson VV measurements and for searches for high-kinematic VH associated Higgs production, because we expect to extract relevant kinematic information from them. For this type of measurement, the predictions have to be redone every time for two reasons. First, the contribution of the kinematically enhanced operators grows with energy and as such will vary bin by bin. Second, the cuts required to target the high energy tails of distributions are significantly different from those of the rate measurements and thus need to be adjusted for every analysis.

These predictions were also computed at quadractic order in the SMEFT using `Madgraph5` [139], `Pythia8` [140], `FastJet` [141], and `Delphes` [142]. We go into more details regarding the implementation of three new high-kinematic distributions in Secs. 4.3.1, 4.3.2 and 5.4.1, but in general the predictions for these distributions are hard to obtain. We first need to reproduce a background to make sure our calibration is good. Then, we have to reproduce the signal (which is usually sub-leading and the reason why we can not calibrate with it) and add the SMEFT contributions. We stress that going through these steps is required because these searches are not designated SMEFT studies, which means the experimental results are not recast in terms of SMEFT by the experiments themselves.

Electroweak precision observables (EWPO)

The EWPO are the processes for which the predictions are given at linear order in the SMEFT within SFitter and were taken from Ref. [143].

3.4 Beyond SMEFT: UV global analyses

SMEFT analyses are interesting in and of themselves. Given the number of parameters, measurements and assumptions (in the SMEFT predictions, the measurements' implementation and the statistical frameworks) that go into them, the results are very likely to vary from one analysis to the next. Studying how each factor impacts the constraints is important in itself, and will be explored further in Chap. 4.

However, SMEFT analyses are not the end goal. The SMEFT must always be put into the broader context of BSM physics. With this in mind, global SMEFT analyses can also be used as a building block towards UV model analyses, see Refs. [2, 41]. In section Sec. 3.4.1, we discuss the one missing ingredient to be able to perform a UV global analysis using everything we already put in place for the SMEFT global analysis. Then, in Sec. 3.4.2, we present the implementation of the matching interface within SFitter.

3.4.1 One missing ingredient: matching UV models onto the SMEFT

Implementing a global analysis is time intensive: one needs to build an analysis tool to construct and map the likelihood, then to implement measurements and predictions for relevant processes. Even though many ingredients of the SMEFT analysis can—to a large extent—be re-used when changing the model under investigation, that is not the case for the predictions. These need to be computed again for all relevant processes in the new model. The predictions for distributions are particularly long and complicated to derive, as we explain in more details in Secs. 4.3.1, 4.3.2 and 5.4.1. This begs the question: is

there simpler way to derive limits on UV model parameters if one already has a SMEFT global analysis in place? The answer is yes.

The idea is to use the predictions already implemented in terms of the WCs of the SMEFT, but to have those WCs described as functions of the UV model coefficients:

$$\frac{f_x}{\Lambda^2}(g_x, Q)\,, \tag{3.21}$$

where f_x are the Wilson coefficients (WCs) of our SMEFT basis defined in Eq. (2.3), g_x are the UV model parameters, and Q is the matching scale. This way one can map the likelihood over the UV model parameter space using the data already implemented

$$\mathcal{L}(m(f_x)|d) = \mathcal{L}(m(g_x)|d)\,. \tag{3.22}$$

Expressions of the form of Eq. (3.21) are called matching equations and computed through a matching procedure. This procedure has been made increasingly faster and systematized in the past few years thanks to the development of functional matching methods [144–157]. We go into more details regarding the matching of one particular UV model—the heavy vector triplet model—onto the SMEFT in Chap. 5. For now, it is enough to understand that implementing those matching formulae as an interface of the SMEFT global analysis allows us to perform a UV global analysis instead.

Note that we need to map the likelihood directly in the UV model parameter space, which means running new Monte Carlo Markov chains (MCMC) in that space. We can not re-use previous mappings performed in the SMEFT parameter space. This is because the matching equations essentially define a very particular lower dimensional slice inside the higher dimensional SMEFT volume. Thus, the mapping in the SMEFT parameter space will not be optimal for the UV subspace. In fact, as we will show in Chap. 5, the constraints in the UV model space considered are far from the usual Gaussian shapes of the SMEFT analysis. Thus, they require to map with great precision certain areas that are very small within the higher dimensional SMEFT volume.

3.4.2 New SFitter matching interface

To implement this within SFitter, we simply need to define a new model where the parameters of interest are those of the UV model, then add a matching interface which computes the value of the WCs given those of the UV model parameters. This matching interface is implemented very simply using the ability within SFitter to define new parameters of interest as functions the parameters used in the prediction. This feature had already been used in other contexts. A simple example is shown in Chap. 4, where the analysis was performed using the parameters $f_\pm$ defined in Eq. (2.5), because those parameters ensure better convergence. We simply make use of this property using the more complex matching functions for the first time.

There is an additional difficulty to consider. The matching equations were derived in the more commonly used Warsaw basis, which differs slightly from the basis presented in **??**. This means we also need to rotate the matching equations from the Warsaw basis into our own basis.

Rotation from Warsaw basis

The content of this section has been published in Ref. [2]. A big part of the text is identical to the content of this publication. We have updated the equations to include two additional operators.

The matching to the heavy vector triplet (HVT) model (described in Sec. 5.2.1) is automated for the Warsaw basis of SMEFT operators [76], in the general flavor case. The results obtained are provided on github at [158] and we give explicit expressions for the tree-level matching in Sec. 5.2.3. In order to interface them with SFITTER, the matching results are mapped onto the basis of Tab. 2.4, to which we need to add the following operator

$$\mathcal{O}_\phi = \left(\phi^\dagger \phi\right)^3 \tag{3.23}$$

to match the number of operators needed in the Warsaw basis. In the following we denote the operators in the Warsaw basis, defined as in Ref. [76], by Q_k and the associated WCs by C_k, such that the dimension six SMEFT Lagrangian in this basis has the form

$$\mathcal{L}_{\text{Warsaw}} \supset \frac{1}{\Lambda^2} \sum_k \sum_{ij} C_{k,ij} \, Q_{k,ij} \,, \tag{3.24}$$

where k runs over the operators labels and i,j are flavor indices, that are present for fermionic operators. The relations between the two operator bases are

$$
\begin{aligned}
&\mathcal{O}_{GG} = Q_{\phi G}\,, &&\mathcal{O}_{3W} = \frac{g^3}{4} Q_W\,, \\
&\mathcal{O}_{BB} = -\frac{g'^2}{4} Q_{\phi B}\,, &&\mathcal{O}_{WW} = -\frac{g^2}{4} Q_{\phi W}\,, &&\mathcal{O}_{BW} = -\frac{gg'}{4} Q_{\phi WB}\,, \\
&\mathcal{O}_{\phi 1} = Q_{\phi D}\,, &&\mathcal{O}_{\phi 2} = -\frac{1}{2} Q_{\phi \square}\,, &&\mathcal{O}_\phi = Q_\phi\,, \\
&\mathcal{O}_\tau = Q_{e\phi,33}\,, &&\mathcal{O}_t = Q_{u\phi,33}\,, &&\mathcal{O}_b = Q_{d\phi,33}\,, \\
&\mathcal{O}_\mu = Q_{e\phi,22}\,, &&\mathcal{O}_{\phi e}^{(1)} = Q_{\phi e,ij}\,\delta^{ij}\,, &&\mathcal{O}_{\phi u}^{(1)} = Q_{\phi u,ij}\,\delta^{ij}\,, \\
&\mathcal{O}_{\phi d}^{(1)} = Q_{\phi d,ij}\,\delta^{ij}\,, &&\mathcal{O}_{\phi Q}^{(1)} = Q_{\phi q,ij}^{(1)}\,\delta^{ij}\,, &&\mathcal{O}_{\phi Q}^{(3)} = \frac{1}{4} Q_{\phi q,ij}^{(3)}\,\delta^{ij}\,, \\
&\mathcal{O}_{4L} = Q_{ll,1221}\,, &&\mathcal{O}_{tG} = ig_s Q_{uG,33}\,,\,, \tag{3.25}
\end{aligned}
$$

and

$$
\begin{aligned}
\mathcal{O}_W &= \frac{g^2}{8} Q_{\phi W} + \frac{g'g}{8} Q_{\phi WB} - \frac{3g^2}{8} Q_{\phi \square} + \frac{g^2 m_h^2}{4} (\phi^\dagger \phi)^2 - \frac{g^2 \lambda}{2} Q_\phi \\
&\quad - \frac{g^2}{4} [(Y_e)_{ij} Q_{e\phi,ij} + (Y_u)_{ij} Q_{u\phi,ij} + (Y_d)_{ij} Q_{d\phi,ij} + \text{h.c.}] - \frac{g^2}{8} \left(Q_{\phi q,ij}^{(3)} + Q_{\phi l,ij}^{(3)} \right) \delta^{ij} \\
\mathcal{O}_B &= \frac{g'^2}{8} Q_{\phi B} + \frac{gg'}{8} Q_{\phi WB} - \frac{g'^2}{2} Q_{\phi D} - \frac{g'^2}{8} Q_{\phi \square} \\
&\quad - \frac{g'^2}{4} \left(\frac{1}{6} Q_{\phi q,ij}^{(1)} - \frac{1}{2} Q_{\phi l,ij}^{(1)} + \frac{2}{3} Q_{\phi u,ij} - \frac{1}{3} Q_{\phi d,ij} - Q_{\phi e,ij} \right) \delta^{ij}\,, \tag{3.26}
\end{aligned}
$$

where all repeated flavor indices are implicitly summed over, and λ is the quartic coupling in the Higgs potential, normalised such that

$$V(\phi) = -\frac{m_h^2}{2} \phi^\dagger \phi + \frac{\lambda}{2} (\phi^\dagger \phi)^2 \,. \tag{3.27}$$

25

As the vector triplet model we are interested in is defined in a flavor-symmetric limit, after the matching procedure the Wilson coefficients of the Warsaw basis operators $Q_{\phi e, \phi u, \phi d}$ and $Q_{\phi l, \phi q}^{(1),(3)}$ will have the form

$$C_{\phi \psi, ij} = \bar{C}_{\phi \psi} \, \delta_{ij} \, , \tag{3.28}$$

while

$$C_{ll,ijkl} = \bar{C}_{ll} \delta_{ij} \delta_{kl} + \bar{C}'_{ll} \delta_{il} \delta_{kj} \, . \tag{3.29}$$

Using this notation, the mapping in terms of Wilson coefficients is

$$
\begin{aligned}
f_B &= \frac{8}{g'^2} \bar{C}_{\phi l}^{(1)} & -\frac{\alpha_s}{8\pi} f_{GG} &= C_{\phi G} \\
f_W &= -\frac{8}{g^2} \bar{C}_{\phi l}^{(3)} & f_{3W} &= \frac{4}{g^3} C_W \\
f_{BB} &= -\frac{4}{g'^2} \left[C_{\phi B} - \bar{C}_{\phi l}^{(1)} \right] & f_{\phi 1} &= C_{\phi D} + 4\bar{C}_{\phi l}^{(1)} \\
f_{WW} &= -\frac{4}{g^2} \left[C_{\phi W} + \bar{C}_{\phi l}^{(3)} \right] & f_{\phi 2} &= -2C_{\phi \Box} - 2\bar{C}_{\phi l}^{(1)} + 6\bar{C}_{\phi l}^{(3)} \\
f_{BW} &= 4 \left[-\frac{C_{\phi W B}}{g g'} - \frac{\bar{C}_{\phi l}^{(3)}}{g^2} + \frac{\bar{C}_{\phi l}^{(1)}}{g'^2} \right] & f_{\phi} &= C_{\phi} - 4\lambda \bar{C}_{\phi l}^{(3)}
\end{aligned}
\tag{3.30}
$$

and for the fermionic ones

$$
\begin{aligned}
\frac{m_\tau}{v} f_\tau &= C_{e\phi,33} - 2(Y_e)_{33} \bar{C}_{\phi l}^{(3)} & f_{\phi e}^{(1)} &= \bar{C}_{\phi e} - 2\bar{C}_{\phi l}^{(1)} \\
\frac{m_t}{v} f_t &= C_{u\phi,33} - 2(Y_u)_{33} \bar{C}_{\phi l}^{(3)} & f_{\phi u}^{(1)} &= \bar{C}_{\phi u} + \frac{4}{3} \bar{C}_{\phi l}^{(1)} \\
\frac{m_b}{v} f_b &= C_{d\phi,33} - 2(Y_d)_{33} \bar{C}_{\phi l}^{(3)} & f_{\phi d}^{(1)} &= \bar{C}_{\phi d} - \frac{2}{3} \bar{C}_{\phi l}^{(1)} \\
\frac{m_\mu}{v} f_\mu &= C_{e\phi,22} - 2(Y_e)_{22} \bar{C}_{\phi l}^{(3)} & f_{\phi Q}^{(1)} &= \bar{C}_{\phi q}^{(1)} + \frac{1}{3} \bar{C}_{\phi l}^{(1)} \\
f_{4L} &= \bar{C}'_{ll} & f_{\phi Q}^{(3)} &= 4 \left[\bar{C}_{\phi q}^{(3)} - \bar{C}_{\phi l}^{(3)} \right] \\
f_{tG} &= -\frac{i}{g_s} C_{uG,33} \, .
\end{aligned}
\tag{3.31}
$$

In addition, the Higgs quartic coupling gets redefined as

$$\lambda_{\text{HISZ}} = \lambda_{\text{Warsaw}} + \frac{4m_h^2}{\Lambda^2} \bar{C}_{\phi l}^{(3)} \, . \tag{3.32}$$

This translates into corrections to the cubic and quartic Higgs self-couplings, which do not contribute to any of the observables in our analysis.

4

To profile or to marginalize: a SMEFT case study

Studying the variables which impact SMEFT global analyses is the first step in a bottom-up approach to constrain new physics.

In this chapter, we perform a SMEFT global analysis for Higgs and electroweak (EW) processes. Our goal is to use the SFITTER framework established in Chap. 3 and present a new Bayesian marginalization treatment for the likelihood computation. We validate this treatment for the old dataset of Ref. [36], then extend the dataset with over 30 new measurements. Finally, we will show the results of the profiled and marginal likelihood treatments for the extended dataset and discuss the differences.

The research presented in this chapter has been published in Ref. [1]. The work was conducted in collaboration with Ilaria Brivio, Sebastian Bruggisser, Nina Elmer, Michel Luchmann, and Tilman Plehn. All figures and tables as well as a significant part of the text are identical to the content of this publication.

4.1 Introduction

Higgs physics at the LHC [159] perfectly illustrates a deep tension in contemporary particle physics: on the one hand, the existence of a fundamental Higgs boson is a direct consequence of describing the electroweak gauge sector in terms of a quantum field theory, specifically a renormalizable gauge theory. It looks like Nature chose the simplest possible realization of the Higgs mechanism, with one light scalar particle and an electroweak vacuum expectation value (VEV) of unknown origin. On the other hand, puzzles like dark matter or baryogenesis seem to point to non-minimal Higgs sectors for convincing solutions based on renormalizable quantum field theory, but without any LHC hint in these directions. The main goal of the LHC Higgs program is to understand if Nature really took the opportunity of a minimal electroweak and Higgs sector solving as many problems as possible, or why she skipped this opportunity in favor of theoretically less attractive alternatives. Or, more practically speaking, we need to study as many Higgs properties as precisely as possible.

Given the vast LHC dataset already after Run 2 and our fundamental ignorance of the correct UV-completion of the SM, we need to measure Higgs-related observables and express them in a consistent, fundamental, and comprehensive theory framework. To provide the necessary precision, this framework has to be defined beyond leading order in perturbation theory, it needs to incorporate kinematic information, and it should allow

us to combine as many LHC observables as possible. The EFT extension of the Standard Model (SMEFT) [160] fulfills precisely these three requirements and defines a theoretical path to understanding the entire LHC dataset in terms of a fundamental Lagrangian. Its main shortcoming is the necessary truncation in the operator dimensionality. The truncated SMEFT approximation will hardly describe new physics appropriately, so SMEFT should really be viewed as a systematic, conservative limit-setting tool. Of course, this practical aspect does not cut into the fundamental attractiveness of an effective quantum field theory description of all LHC data.

There exists a range of phenomenological Higgs-gauge analyses [30–32, 36, 41–43, 47, 48], top analyses [33, 38, 45, 49], combinations of the two [39, 40], and combinations with parton densities [161]. These analyses are typically based on experimentally preprocessed information, including the full range of uncertainties. Given that by assumption any SMEFT analysis will be centered around the renormalizable SM-Lagrangian, the main focus of all global analyses is the uncertainty treatment and the correlations between the different operators. Technically, these two tasks tend to collide. We can choose a conservative uncertainty treatment based on profile likelihoods and nuisance parameters, but it is much more computing-efficient to treat correlations through covariance matrices of marginalized Gaussian likelihoods [162]. The SFITTER framework [36–38, 50, 127, 128] is unique in the sense that it has mostly been used for profile likelihood analyses, but can provide marginalized limits equally well [121, 127].

We make use of this flexibility and study, for the first time, the difference between profiled and marginalized likelihoods of the same global Run 2 dataset. In Sec. 4.2 we find that for the Higgs-electroweak dimension-6 operators and the given dataset the two approaches agree well, so we can use the marginalized setup to treat correlated measurements and uncertainties efficiently. Based on these results, we include a range of recent Run 2 measurements from Higgs studies as well as from exotics resonance searches, again with a focus on a comprehensive and conservative uncertainty treatment, in Sec. 4.3. Finally, we study the impact of these new measurements and the inputs from a global top analysis in Sec. 4.4 and find interesting differences between the profiling and marginalization methods.

4.2 Bayesian SFitter setup

Global SMEFT analyses are a key ingredient to a more general analysis strategy at the LHC, which is to test theory predictions based on perturbative quantum field theory using the full kinematic range of the complete set of LHC measurements. It is worth stressing that SMEFT analyses are currently the only way to systematically probe kinematic LHC measurements beyond resonance searches. They come with two assumptions which greatly simplify the actual analyses

1. experimentally, we know that our SMEFT analysis is not confronted with established anomalies; those should be discussed using properly defined BSM models;

2. theoretically, SMEFT can only describe small deviations from the Standard model, otherwise the dimensional expansion in Eq. (2.1) is not valid.

While global SMEFT analyses with a truncated Lagrangian can translate kinematic measurements into fundamental parameters, these two aspects imply that their outcome will be limit-setting. For our analysis this means that we already know that the global

maximum of the SMEFT likelihood lies around the SM-limit $f_x/\Lambda^2 \to 0$. The exact position of the most likely parameter point is of limited interest, the main task of the global analysis is to determine the uncertainty on the values of the WCs or, more in general, the finite preferred region in the multi-dimensional SMEFT parameter space.

In this spirit, the goal of the SFITTER framework is to enable an independent interpretation of experimental inputs, without relying on pre-processed information and including a comprehensive treatment of statistical, systematic, and theory uncertainties [50, 127, 128]. The SFITTER methodology relies on the construction of a likelihood function in which these uncertainties can be described by nuisance parameters. In all previous SFITTER analyses, nuisance parameters are profiled over. The resulting profile likelihood is then profiled over the parameters of interest, to extract one- and two-dimensional limits on the WCs. An alternative, Bayesian treatment is based on marginalising over nuisance parameters and parameters of interest. It has been adopted in several SMEFT analyses [162–166] and simplifies greatly the treatment of correlated uncertainties. The goal of this work is to perform an apples-to-apples comparison between a profiled and a marginalised likelihood, employing exactly the same data and uncertainties inputs in both cases.

Marginal likelihood

Since marginalization is new in SFITTER, we provide a brief description of the main features. The corresponding profile likelihood treatment is discussed in detail in Refs. [36–38, 127, 128]. The first step of a global analysis is the construction of the fully exclusive likelihood $\mathcal{L}_{\text{excl}}$, which is a function of the parameters of interest f_x and of a set of nuisance parameters θ_i. This $\mathcal{L}_{\text{excl}}$ is defined with the following uncertainty treatment: (i) statistical uncertainties are included via a Poisson distribution, in some cases approximated using a Gaussian whenever this stabilizes the numerical evaluation; (ii) systematic uncertainties are assumed to be Gaussian, organized in 31 categories, such that uncertainties within the same category are fully correlated through a covariance matrix or through nuisance parameters. Systematics which do not fit into any of the 31 categories are assumed to be uncorrelated; (iii) theory uncertainties are modelled as flat distributions. Whenever theory uncertainties need to be correlated we use an explicit nuisance parameter.

For a Bayesian analysis we first marginalize over or integrate out the nuisance parameters. This yields the marginal likelihood $\mathcal{L}_{\text{marg}}$, for one counting measurement and one parameter illustrated by

$$\mathcal{L}_{\text{marg}}(f_x) = \int d\theta \, \mathcal{L}_{\text{excl}}(f_x, \theta) = \int d\theta \, \text{Pois}(d|m(f_x, \theta)) \, p(\theta) \,. \tag{4.1}$$

Here d stands for the measured number of events, m is the model (theory) prediction, θ is a nuisance parameter and $p(\theta)$ the distribution over the nuisance parameter which, in the Bayesian context, defines the prior. In SFITTER, nuisance priors are either Gaussian or flat. Computing $\mathcal{L}_{\text{marg}}$ in SFITTER starts with the marginalisation procedure over the nuisance parameters, so we omit the dependence on f_x for now.

SFITTER provides several options to define the statistical model of a measurement, including a simplified Gaussian likelihood where uncertainties add in quadrature. A more sophisticated and reliable framework starts with a typical LHC measurement as an independent counting experiment, which is modelled by a Poisson distribution.

Systematic uncertainties or theory uncertainties then define the completely exclusive likelihood for one measurement

$$\mathcal{L}_{\text{excl}}(\theta) = \text{Pois}(d|m(\theta_1, \theta_2, ..., b)) \, p(b) \prod_i p(\theta_i) \,. \tag{4.2}$$

Here d is the measured number of events, b the background estimate, and m the model prediction, that is a function of the nuisance parameters θ_i. The distributions $p(b)$ and $p(\theta_i)$ incorporate our knowledge about these quantities. In general, they can be extracted from auxiliary measurements, simulations, or other possible sources. However, because tracking hundreds of different reference measurements is beyond the scope of SFITTER, we simply assume $p(\theta_i)$ to be Gaussian for systematic uncertainties and flat or uniform for theory uncertainties,

$$p(\theta_i) = \begin{cases} \mathcal{N}_{\theta_{\text{syst},i}, \sigma_i}(0) & \text{systematics} \\ \mathcal{F}_{\theta_{\text{theo},i}, \sigma_i}(0) & \text{theory} \,. \end{cases} \tag{4.3}$$

In this step we assume that all prior distributions for θ_{syst} and θ_{theo} are centered around zero, with given half-widths σ.

For $p(b)$, SFITTER provides several choices: for measurements where b is extracted from a single control region (CR) measurement we use

$$p(b) = \text{Pois}(b_{\text{CR}}|bk) \,, \tag{4.4}$$

where k is an interpolation factor between control region (CR) and signal region, b_{CR} is the measured number of events in the control region, and b is the expected number of background events in the signal region. For measurements with several control regions or with simulated backgrounds we assume the combined $p(b)$ to be a Gaussian. Systematic uncertainties on the background measurement can also be included, and are assumed to be fully correlated with the uncertainties on the signal region within the same category.

Typically, the dependence of the theory prediction m on the nuisance parameters in Eq. (4.2) is not spelled out or extremely complex to determine. To simplify this task, we assume a leading linear dependence on assumed-to-be small uncertainties

$$m \approx s + b + \theta_{\text{theo},1} + \theta_{\text{theo},2} + \cdots + \theta_{\text{syst},1} + \theta_{\text{syst},2} + \cdots \equiv s + b + \theta_{\text{tot}} \,. \tag{4.5}$$

where s is the expected number of signal events. The exclusive likelihood of Eq. (4.2) can then be written as

$$\mathcal{L}_{\text{excl}}(\theta) \approx \text{Pois}(d|s + b + \Sigma\theta_{\text{theo},j} + \Sigma\theta_{\text{syst},i}) \, p(b) \prod_j \mathcal{F}_{\theta_{\text{theo},j}, \sigma_j}(0) \prod_i \mathcal{N}_{\theta_{\text{syst},i}, \sigma_i}(0) \,, \tag{4.6}$$

The marginal likelihood for a single measurement is then constructed by integrating over all nuisance parameters,

$$\begin{aligned} \mathcal{L}_{\text{marg}} &= \int \prod_j d\theta_{\text{theo},j} \int \prod_i d\theta_{\text{syst},i} \int db \, \mathcal{L}_{\text{excl}}(\theta) \\ &= \int \prod_j d\theta_{\text{theo},j} \mathcal{F}_{\theta_{\text{theo},j}, \sigma_j}(0) \int \prod_i d\theta_{\text{syst},i} \mathcal{N}_{\theta_{\text{syst},i}, \sigma_i}(0) \end{aligned}$$

$$\times \int db \, \text{Pois}(d|s + b + \Sigma\theta_{\text{theo},j} + \Sigma\theta_{\text{syst},i}) \, p(b) \, . \quad (4.7)$$

The integration over b can be performed analytically if $p(b)$ is a Poisson distribution. In this case, the convolution $\mathcal{P}(d|s + \theta_{\text{tot}})$ of $p(b)$ and $\text{Pois}(d|m)$ gives a so-called Poisson-Gamma model, as Eq. (4.4) is a special case of the Gamma distribution,

$$\mathcal{L}_{\text{marg}} = \int \prod_j d\theta_{\text{theo},j} \mathcal{F}_{\theta_{\text{theo},j},\sigma_j}(0) \int \prod_i d\theta_{\text{syst},i} \mathcal{N}_{\theta_{\text{syst},i},\sigma_i}(0) \times \mathcal{P}(d|s + \theta_{\text{tot}}) \, . \quad (4.8)$$

We use θ_{tot} as defined in Eq. (4.5). To solve the remaining integrals over the nuisance parameters we replace one of the integrals, for instance $\theta_{\text{syst},1}$ with $(\theta_{\text{tot}} - \Sigma_{i\neq 1}\theta_{\text{syst},i})$,

$$\mathcal{L}_{\text{marg}} = \int d\theta_{\text{tot}} \, \mathcal{P}(d|s + \theta_{\text{tot}})$$
$$\times \underbrace{\int \prod_j d\theta_{\text{theo},j} \mathcal{F}_{\theta_{\text{theo},j},\sigma_j}(0) \int \prod_{i\neq 1} d\theta_{\text{syst},i} \mathcal{N}_{\theta_{\text{syst},i},\sigma_i}(0) \mathcal{N}_{\theta_{\text{syst},1},\sigma_1}(0)}_{\text{solved analytically}} \, .$$
$$(4.9)$$

Assuming only Gaussian plus at most three flat priors, all θ-convolutions except for one can be performed analytically. The corresponding closed formulas are implemented in SFITTER, speeding up the marginalisation. The remaining 1-dimensional integral in Eq. (4.9) is solved numerically with Simpson's method.

Marginalizing over nuisance parameters and profiling over them will not give the same marginalized likelihood. Only for statistical uncertainties described by Poisson statistics and Gaussian systematics, the two lead to the same marginalized result in the limit of large enough statistics. Differences appear when we use flat theory uncertainties. For a Bayesian marginalization the central limit theorem ensures that the final posterior will be approximately Gaussian. Using a profile likelihood, two uncorrelated flat uncertainties add linearly, while a combination of flat and Gaussian uncertainties give the well-known RFit prescription [132]. Figure 4.1 shows, as an illustration, the distributions obtained combining one Gaussian with one (left) or three (right) flat nuisance parameters. We see that the profile likelihood or RFit result maintains a flat core and is independent of the number of theory nuisances, while the marginalised result varies and is very close to a Gaussian in the right panel.

Combining channels

Unlike probabilities, likelihoods of a set of measurements can simply be multiplied. This means we can generalize Eq. (4.2) and (4.6) to a set of N measurements by replacing

$$\text{Pois}(d|m)p(b) \quad \longrightarrow \quad \prod_k \text{Pois}(d_k|m_k)p(b_k)$$
$$\mathcal{N}_{\theta_{\text{syst},i},\sigma_i}(0) \quad \longrightarrow \quad \mathcal{N}_{\vec{\theta}_{\text{syst},i},\Sigma_i}(\vec{0})$$
$$\mathcal{F}_{\theta_{\text{theo},j},\sigma_j}(0) \quad \longrightarrow \quad \prod_k \mathcal{F}_{\theta_{\text{theo},kj},\sigma_{kj}}(0) \, , \quad (4.10)$$
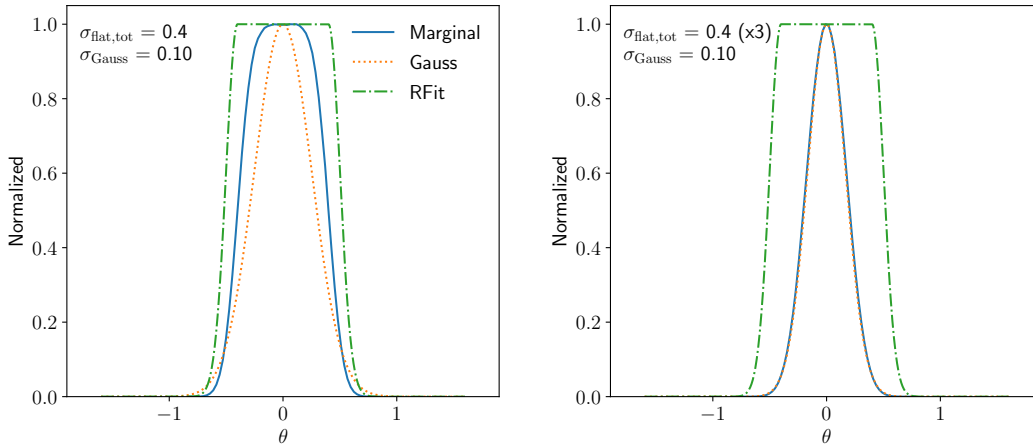
Figure 4.1: Marginalized and profiled likelihoods from the convolution of a Gaussian distribution with one (left) and three (right) flat ones. The orange curve shows, for comparison, the Gaussian obtained adding half-widths in quadrature.

with

$$m_k \approx s_k + b_k + \sum_i \theta_{\text{syst},ki} + \sum_j \theta_{\text{theo},kj} \equiv s_k + b_k + \theta_{\text{tot},k} \ . \tag{4.11}$$

Here we assume that the theory uncertainties are uncorrelated, while the systematics can be correlated, so we need to introduce an N-dimensional Gaussian with the covariance matrices Σ_i encoding the correlations between uncertainties of category i entering different measurements k. We use either uncorrelated or fully correlated systematics.

When we compute the marginal likelihood in analogy to Eq. (4.7) the only non-trivial aspect are the correlated systematic uncertainties including the covariance matrix. However, the convolution of N-dimensional Gaussians still leads to one N-dimensional Gaussian, where the combined covariance matrix is the sum of the individual covariance matrices. This means, in the last step of Eq. (4.9) we are now left with an N-dimensional integral over $\theta_{\text{tot},k}$, correlated through the covariance matrix appearing in the distribution of the systematic nuisance parameters.

In SFITTER, this integral is solved by approximating it with the Laplace method. This is computationally efficient and works well for cases where most of the probability is concentrated around one mode. This is the case when the nuisance parameters are Gaussians or flat. We can then write

$$\int dx^n f(x) = \int dx^n e^{\log f(x)} \ , \tag{4.12}$$

and assume that $f(x)$ has a maximum at $x = x_0$. Then one can expand $\log f(x)$ up to second order around x_0 as

$$\log f(x) \approx \log f(x_0) + \underbrace{\frac{\partial}{\partial x} \log f(x_0)(x - x_0)}_{=0} + \underbrace{\frac{\partial^2}{\partial x_i x_j} \log f(x_0)(x - x_0)_i \ (x - x_0)_j}_{=F_{ij}(x_0)} + \ ...$$
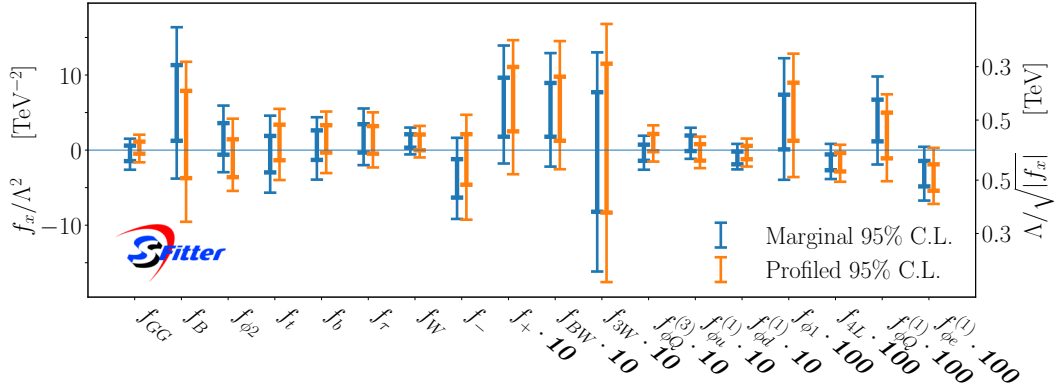
$$\tag{4.13}$$

Figure 4.2: 68% and 95% confidence intervals from profile likelihoods and Bayesian marginalization. The dataset is the same as in Ref. [36].

such that the integral is approximated by

$$\int dx^n f(x) \approx f(x_0) \sqrt{\frac{(2\pi)^n}{\det F(x_0)}} \; . \tag{4.14}$$

Note that $f(x)$ is given by the exclusive likelihood, with the maximum at $f(x_0)$ kept through profiling but not through marginalization. The matrix $F(x_0)$ is the Hessian of the log-likelihood at the maximum, i.e. the Fisher information matrix in the space of the nuisance parameters. In SFITTER, x_0 is extracted with an analytic expression, approximating the Poisson distribution in Eq. (4.2) with a Gaussian. The resulting error is compensated by keeping a finite first derivative in Eq. (4.13), which in turn requires us to modify Eq. (4.14) by introducing an additional term depending on the first derivative of the log-likelihood. Both the first and second derivatives can be computed numerically. All these approximations in evaluating the exclusive and marginal likelihoods have been checked by evaluating the exclusive likelihood using Markov chains.

Validation

We can validate the implementation of the Bayesian marginalization over nuisance parameters and WCs starting from the fully exclusive likelihood using the operator basis and dataset of Ref. [36]. The SMEFT Lagrangian is given in Eq. (2.3), but without the muon Yukawa, the top-gluon coupling $\mathcal{O}_{tG}$, and the invisible branching ratio of the Higgs. For the direct comparison we construct the marginal likelihood by profiling or marginalizing over all nuisance parameters and Wilson coefficients. We then extract the posterior probability and 68% and 95% confidence intervals. Unless otherwise specified, we assume flat, wide priors for all WCs. This choice minimizes the impact of the prior on the final result, and we have verified that our priors on the WCs indeed fulfill this condition. In Fig. 4.2, we show the 68% and 95%CL limits from the corresponding 18-dimensional operator analysis. We see that the results of the two methods are in excellent agreement.

Going beyond confidence intervals, we can look at the distributions of the 1-dimensional profile likelihoods or marginalized probabilities. We show three examples in Fig. 4.3. Because the analysis relies on actual LHC data, the central values are not at zero Wilson coefficients. The well-measured WC f_W shows no difference between the profile and the
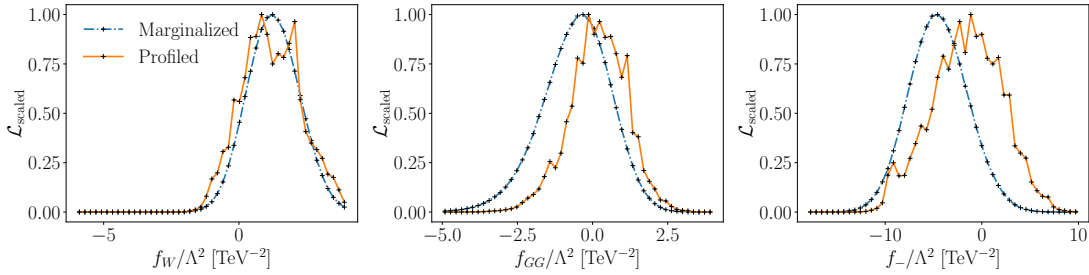
Figure 4.3: Profile likelihoods vs marginalized likelihood for a set of WCs. The two curves are scaled such that the maximum values are at $\mathcal{L}_{\text{scaled}} = 1$.

marginalized results. For f_{GG}, we see a slight deviation in the central values, within one standard deviation and therefore not statistically significant. This effect points to the theory and pdf uncertainties, which we assume to be flat, and which therefore allow the central value to move freely for the profile likelihood approach, while the marginalization leads to a well-defined maximum when combining two individually flat likelihood distributions. In Fig. 4.2 we see that this difference only has a slight effect on the lower boundary when we extract 95%CL limits on f_{GG}. Finally, we see a similar effect for f_-, even though this measurement depends on several different LHC channels. According to Fig. 4.2 this is one of the largest and still not significant differences between the two methods.

The source of the differences in Fig. 4.3 can be traced back to whether the uncertainty-related nuisance parameters are marginalised or profiled. Fig. 4.4 shows that, once the uncertainty treatment is fixed, the results are independent of whether the WCs are marginalized or profiled over.

Next, we check 2-dimensional profiled and marginalised likelihoods. Figure 4.5 shows three examples involving the same WCs as in Fig. 4.3. First, we see that there exists an anti-correlation between f_{GG} and f_t, the modified top Yukawa also affecting the loop-induced production process $gg \to H$. This suggests that a slightly high rate measurement can be accommodated by adjusting either of the two Wilson coefficients. Because the uncertainty on this measurement includes sizeable theory and pdf contributions, the same difference between the two methods can be seen for each of the two WCs individually and for their correlation. Another instructive example is the correlation between f_W, determined from kinematic distributions, and $f_{\phi 2}$ leading to a shift in the Higgs wave function. Here the difference only appears in $f_{\phi 2}$, the parameter extracted from total
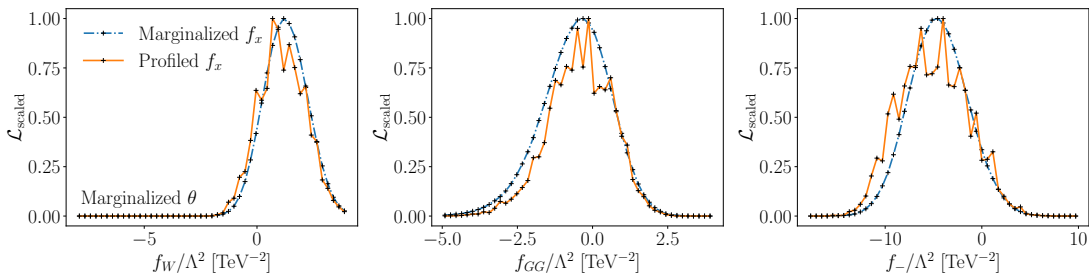

Figure 4.4: Likelihoods profiled vs marginalized over the Wilson coefficients f_x, but always marginalized over all nuisance parameters θ. We show the same WCs as in Fig. 4.3.
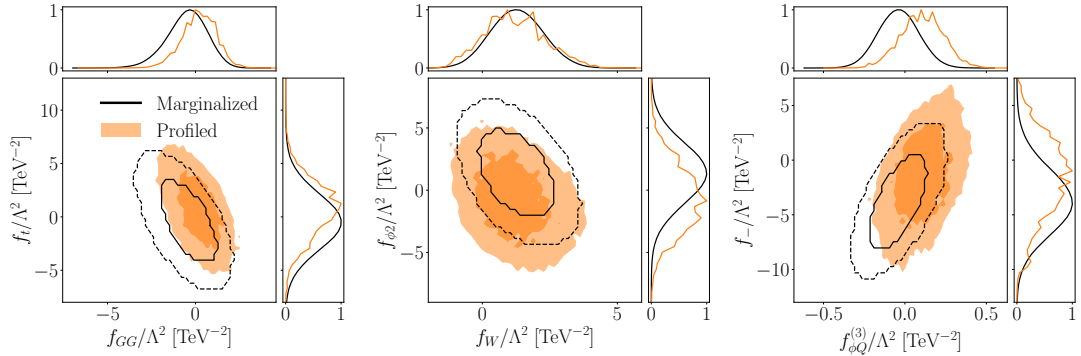
Figure 4.5: Comparison of 2-dimensional correlations of profiled and marginalized likelihoods.

rates and especially sensitive to theory uncertainties. Finally, we show the correlation between f_- and $f_{\phi Q}^{(3)}$ and observe the usual correlation from the sizeable range of kinematic di-boson measurements [167].

Finally, we can check for alternative maxima in the likelihood and find that f_+ is the only WC exhibiting a non-trivial second mode. This can be understood from the f_+ vs f_- plane. By a numerical accident, the SMEFT corrections to all Higgs production and decay processes vanish in the SM-maximum and also close to the point $f_-/\Lambda^2 = -3$ and $f_+/\Lambda^2 = 2.7$. The only measurement which breaks this degeneracy is $H \to Z\gamma$, with limited statistical power. In the f_+ axis, the position of the maximum is fully determined by $H \to \gamma\gamma$, which is measured precisely enough to resolve the two modes, while in the f_- axis the constraints can not distinguish the second maximum from the SM point.

Given the consistency condition of the SMEFT approach, we should not compare the two modes at face value, even though the Bayesian setup would allow for this. On the other hand, we need to confirm that this choice of modes does not affect other parameters in a significant manner once it is embedded in the 18-dimensional space. In Fig. 4.6 we show what happens if we restrict our parameter analysis to either the SM-mode or the second mode. To this end we run Markov chains mapping out both modes and then separate the samples through the condition $f_+/\Lambda^2 \lessgtr 2$. We see that choosing the second mode in f_+ has a small effect on f_-, pushing the best-fit closer to $f_- = -3$, but none of the other Wilson coefficients is affected. We also confirmed that both modes are of equal height by choosing a Breit-Wigner proposal function, which ensures that the Markov chains can move large distances, helping each individual chain to jump between both modes.
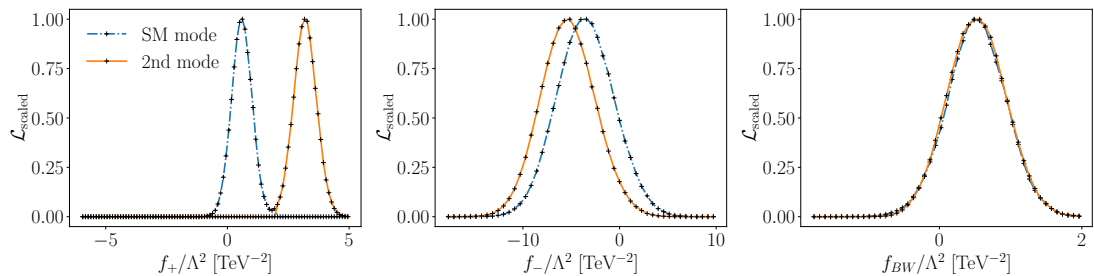

Figure 4.6: Marginalized likelihoods for the SM-like and the second mode in f_+, again for the 18-dimensional analysis.
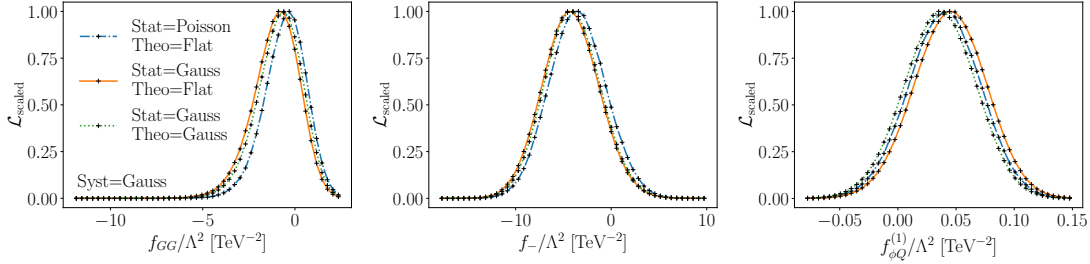
35

Figure 4.7: Marginalized likelihoods for different uncertainty modeling. The SFITTER default is a Poisson likelihood with flat theory uncertainties and Gaussian systematics (blue dot-dashed).

Uncertainties and correlations

After confirming that the slight differences between the profile and marginalization approaches are related to the treatment of uncertainties, we can check the impact of the SFITTER-specific uncertainty treatment. By default, and as explained earlier, we construct the exclusive likelihood with flat theory uncertainties and Gaussian systematics. By switching all uncertainties to Gaussian distributions we construct the completely Gaussian likelihood shown in Fig. 4.7. If we marginalize over the different uncertainties, the central limit theorem guarantees that for enough different uncertainties the results will be identical. The exact level of agreement between different uncertainty models depends on the dataset and the size of the individual uncertainties and can not be generalized. For instance, sizeable differences will appear when an outlier measurement generates a tension in the global analysis. Such a tension can be accommodated more easily using a single flat uncertainty with its reduced cost in the likelihood value.

Because the main difference between profiling and marginalizing over uncertainties appears for the flat theory uncertainties, the results from Fig. 4.7 motivate the question how relevant the theory uncertainties really are for the Run 2 dataset analyzed in Ref. [36]. We show three 1-dimensional likelihoods in Fig. 4.8 and indeed find that after marginalizing over all nuisance parameters and over all other Wilson coefficients the theory uncertainties do not play any visible role. Obviously, this statement is dependent on a given dataset, on the operators we are looking at, and on the assumed uncertainties, and it clearly does not generalize to all global Run 2 analyses.

The last effect we need to study is the impact of correlations between the different uncertainties. In Fig. 4.9 we show what happens with the 1-dimensional marginalized likelihoods when we switch off all correlations between systematic uncertainties of the
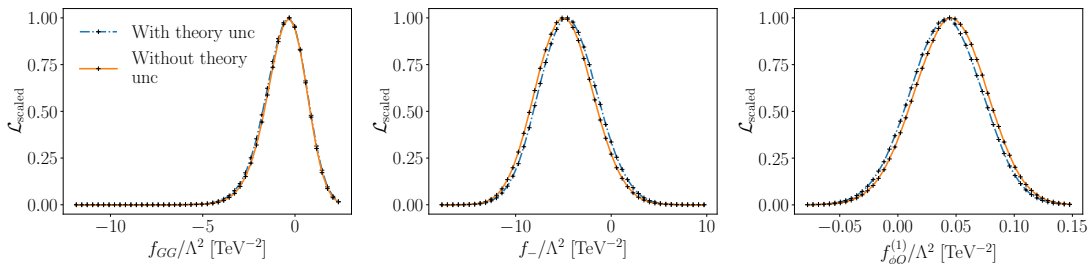

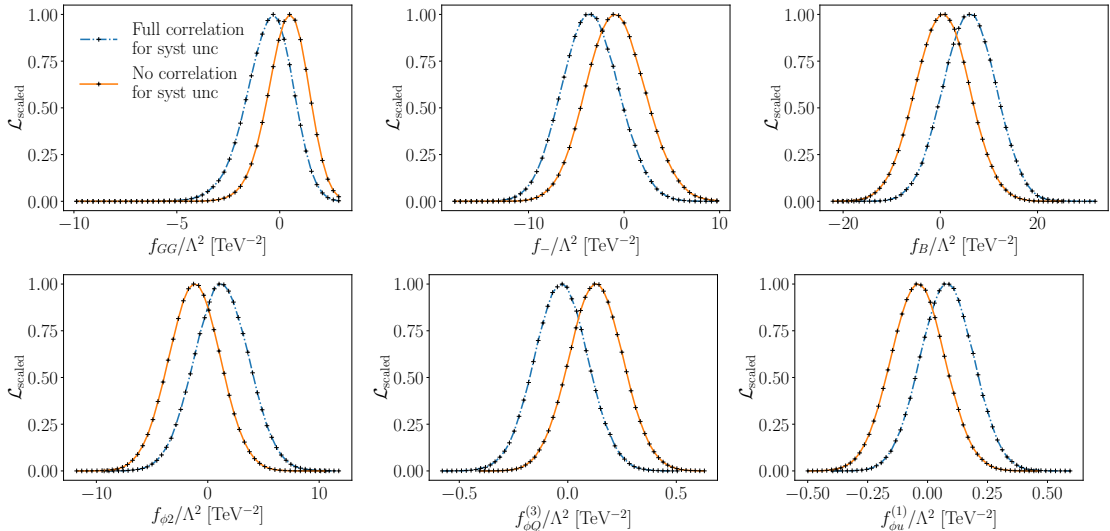Figure 4.8: Marginalized likelihoods with and without theory uncertainties.

Figure 4.9: Marginalized likelihoods with and without correlations between systematic uncertainties of the same category.

same kind. We see that the correlations have a much larger impact than anything else we have studied in this section. While the size of the uncertainties do not change much, the central values essentially vary freely within one standard deviation. An analogous effect was observed in Ref. [162]. We can not emphasize enough that all statements about the validity of different approximations do not generalize to new, incoming measurements, as we will see in the following section. However, something that will not change is the key relevance of correlations as indicated by Fig. 4.9.

4.3 Updated dataset

After the detailed comparison of a profile likelihood and Bayesian SFITTER approach we can, in principle, apply the numerically simpler Bayesian approach to update the SMEFT analysis of the Higgs-electroweak sector with a series of new Run 2 results. As a first step, we introduce the set of new kinematic measurements entering the updated SFITTER analysis. We focus on an improved treatment of correlated uncertainties.

4.3.1 WW resonance search

Once we notice that especially boosted kinematics with large momentum transfer through Higgs interactions play a key role in SMEFT analyses [167, 169], it is clear that the reinterpretation of VH and VV resonance searches should be extremely useful for a global SMEFT analysis [36, 37]. To the best of our knowledge, SFITTER is currently the only global analysis framework which includes these kinds of signatures.

First, we add the ATLAS search for resonances in the semi-leptonic VV final state [168], as briefly discussed in Ref. [2]. We only use the WW 1-lepton category in the merged Drell-Yan and gluon-fusion high-purity signal region,

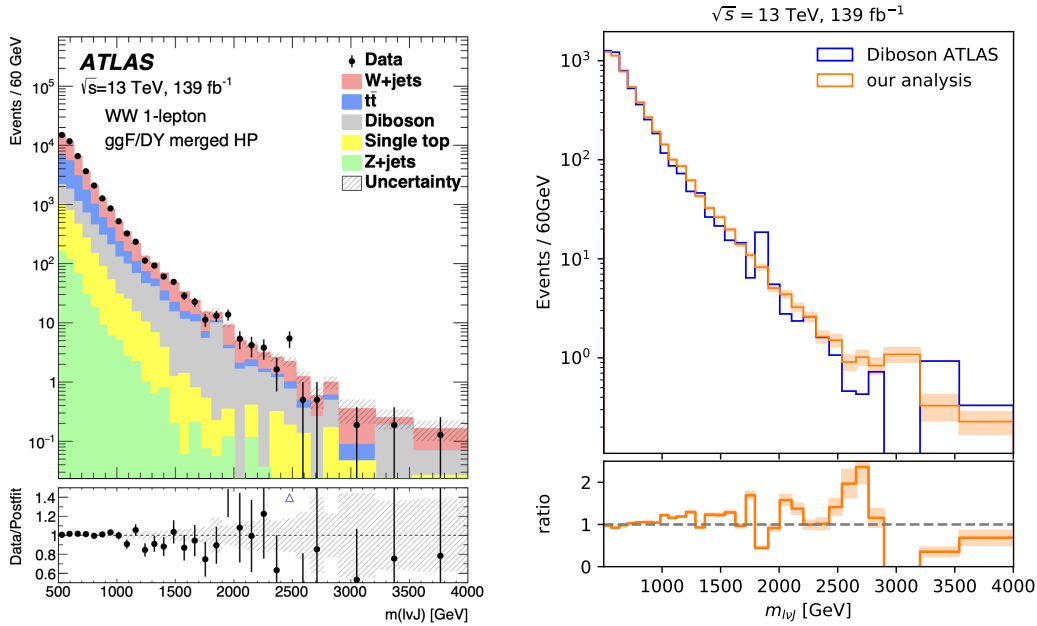$$pp \to W^+ W^- \to \ell^+ \nu_\ell \, jj + \ell^- \bar{\nu}_\ell \, jj \ . \tag{4.15}$$

Figure 4.10: Left: measured m_{VV} distribution [168]. Right: comparison between ATLAS results and our SM background estimate. The orange band shows the statistical uncertainty from the Monte Carlo generation.

Our signal consists of W^+W^- production modified by SMEFT operators. We neglect SMEFT effects in the leading W+jets and $t\bar{t}$ backgrounds. We include all other $W_{\ell\nu}V_{jj}$ and $Z_{\ell\ell}V_{jj}$ channels as SM-backgrounds and verified that SMEFT corrections to the other di-boson channels are sufficiently suppressed by the analysis setup.

The signal is simulated using `Madgraph5` [139], `Pythia8` [140], `FastJet` [141], and `Delphes` [142] with the standard ATLAS card at leading order and in the SM and requiring the lepton pair to come from an intermediate on-shell $W^\pm$. The hadronic W-decay is simulated using `Pythia8`. Fat jets are identified using the default categorization in `Delphes` and ignoring the cut on the D_2 variable. The complete SM-rate is compared to the left panel of Fig. 4.10, taken from Ref. [168]. We reproduce the event selection based on the analysis cuts listed in Tab. 2 of Ref. [168]. No re-calibration of energy scales or fat-jet invariant mass windows is required, but we adjust the histogram entries by a factor 1.606 to match the ATLAS normalization of the di-boson background and accommodate efficiencies and higher-order corrections [170]. In the right panel of Fig. 4.10 we show the final m_{WW} distribution obtained with this procedure. Finally, we extract the statistical and systematic uncertainty from the ATLAS analysis, as shown in the lower panel in Fig. 4.10. Whenever backgrounds are estimated from control regions, the Gaussian systematic uncertainties are smaller than the Poisson-shaped statistical uncertainties in the signal region.

To include the VV channel in our SMEFT analysis we re-bin the original distribution such that we have a minimum of five observed events per bin. The kinematic distribution we use in SFITTER is shown in the left panel of Fig. 4.11. Here all statistical uncertainties are treated as uncorrelated and added in quadrature, the same for the systematic background uncertainties linked to Monte Carlo statistics, while other systematic uncertainties are conservatively treated as fully correlated and consequently added linearly. Finally, we add a 80% theory uncertainty on the signal predictions in all bins and assuming no
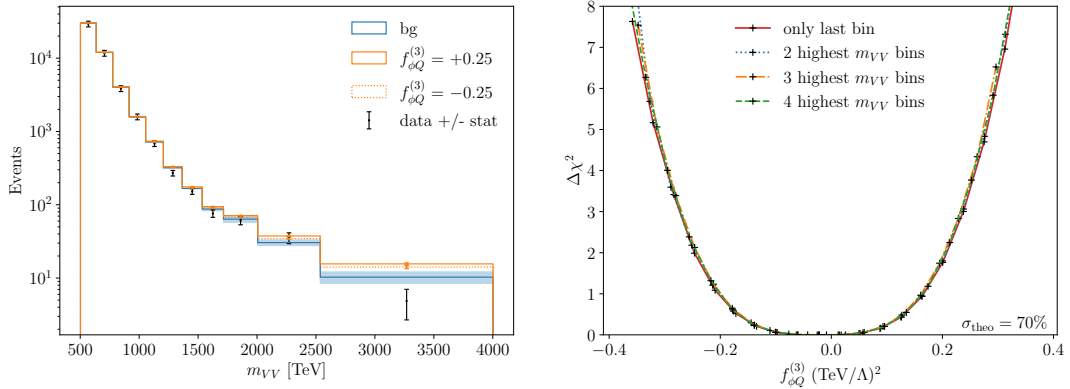
Figure 4.11: Left: re-binned m_{WW} distribution for the semi-leptonic WW analysis implemented in SFITTER. We show the complete continuum background, including statistical and systematic uncertainties, and the effect of a finite Wilson coefficient $f_{\phi Q}^{(3)}$. Right: toy analysis for the same WC using different numbers of bins.

correlation among them. Of this 70% account for the uncertainties in our SMEFT Monte Carlo predictions and 10% for V+jets and single-top modeling.

In the right panel of Fig. 4.11 we show the limit in terms of the Gauss-equivalent

$$\Delta \chi^2 = \chi^2 - \chi^2_{\min} = -2 \log \mathcal{L} + 2 \log \mathcal{L}_{\max} \, , \tag{4.16}$$

extracted from different bins of the measured m_{WW} distribution. We see that the likelihood maximum slightly deviates from the SM point $f_{\phi Q}^{(3)} = 0$, and the last bin completely dominates the likelihood distribution. This is expected for momentum-enhanced operators which modify the tails of momentum distributions, as systematically analyzed in Ref. [167]. We will discuss the effect of the under-fluctuation in the last bin in more detail in Sec. 4.4.1.

4.3.2 WH resonance search

Complementing the dataset of Ref. [36] we include two new resonance searches, one described in Ref. [2] and another ATLAS analysis looking for

$$pp \to WH \to \ell \bar{\nu}_\ell \, b\bar{b} \tag{4.17}$$

at high invariant masses [171]. We focus on WH production with one b-tag, because it includes the best kinematic measurement at high m_{VH}. This analysis applies cuts on the WH topology and requires exactly one single-b-tagged fat jet. In the merged category the b-tags are part of a fat jet.

We generate di-boson events for the combined di-boson channels with lepton-hadron decays

$$pp \to W_{\ell\nu}W_{jj}, \; W_{\ell\nu}Z_{jj}, \; Z_{\ell\ell}W_{jj}, \; Z_{\ell\ell}Z_{jj} \, , \tag{4.18}$$

again using the `Madgraph5-Pythia8-FastJet-Delphes` chain with the standard ATLAS card at leading order. They can be compared to the grey di-boson background in the
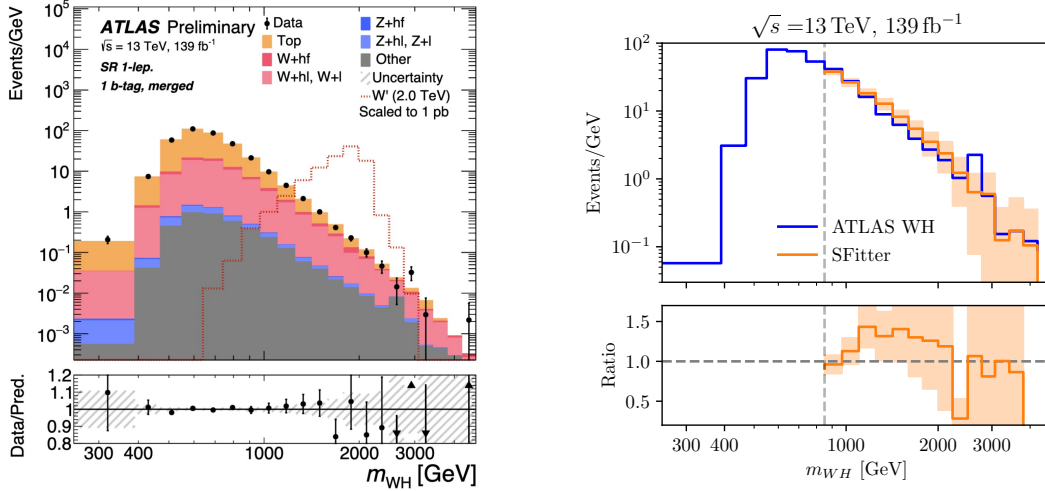
Figure 4.12: Left: measured m_{WH} distribution [171]. Right: comparison between the the ATLAS results and our SM background estimate. The orange band shows the statistical uncertainty from the Monte Carlo generation.

left panel of Fig. 4.12, including the *b*-tagging and corresponding mis-tagging. After adjusting the m_{WH}-independent efficiency factor we find the agreement illustrated in the right panel of Fig. 4.12. We apply the same efficiency factor for the WH signal and then use the reweighting module in `Madgraph5` to estimate the SMEFT rates. The *W*-decay to electrons or muons is included through `Madgraph5`, while the Higgs decay to $b\bar{b}$ pairs is simulated by `Pythia8`. We neglect SMEFT corrections to the $t\bar{t}$ and W/Z+jets backgrounds, assuming that the targeted phase space region favors the Higgs signal. Having to make this assumption is unfortunate, but we emphasize that the number of experimental measurements should prevent us from falling for SMEFT corrections canceling between the different signals and backgrounds.

To define a meaningful measurement for our global analysis we have to merge bins of the original distribution such that at least three observed events appear per bin. In Fig. 4.13, we show the actually implemented distribution for the complete SM background and
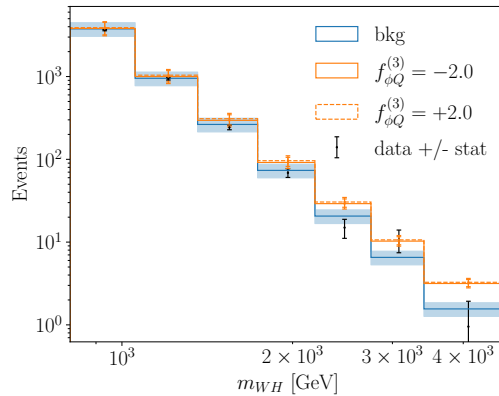

Figure 4.13: Re-binned m_{WH} distribution implemented in SFITTER, including statistical and systematic uncertainties. We show the complete continuum background and the effect of a finite Wilson coefficient $f_{\phi Q}^{(3)}$.
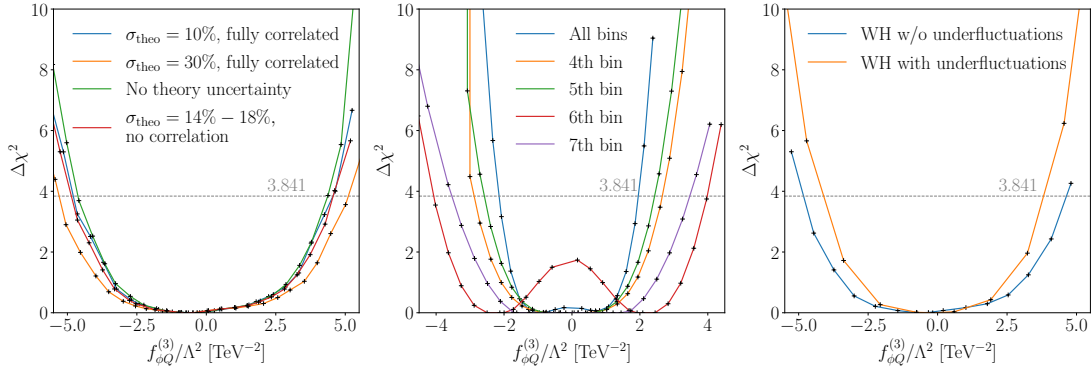
40

Figure 4.14: Log-likelihood for a 3-parameter analysis of the WH search as a function of $f_{\phi Q}^{(3)}$. We vary the theory uncertainties and their correlation (left), the number of bins included with uncorrelated theory uncertainties for a 1-dimensional analysis (center), and the treatment of under-fluctuations (right).

including a finite WC $f_{\phi Q}^{(3)}$. For each bin we include a statistical uncertainty following a Poisson distribution and a Gaussian systematic uncertainty, as reported by ATLAS. In addition, we include a 13% theory uncertainty also reported by ATLAS and a theory uncertainty between 1% and 4% per bin from our SMEFT predictions, but neglecting correlation between various bins.

We can check some of our assumptions on the way we model theory uncertainties from a three-parameter analysis with $f_{\phi Q}^{(3)}$, f_W and f_{WW}. Neglecting the correlations in the theory uncertainties is justified by the left panel of Fig. 4.14. It shows the Gauss-equivalent $\Delta \chi^2$ for varying the theory uncertainties with different correlations; the orange and green lines represent a 10% and 30% theory uncertainty, fully correlated. The green line shows results without theory uncertainty, and the red line assumes our SMEFT theory uncertainty without correlations. These results are very close to each other, so we can ignore correlations in the theory uncertainties from the EFT prediction.

The central panel compares constraints from the 3-parameter analysis from the entire m_{WH} distribution and only including one bin at a time. The limit improves sharply when the 4th and 5th bins are included. This can be understood from Fig. 4.13, where both of these bins show significant under-fluctuations. In the right panel of Fig. 4.14 we show that by removing under-fluctuations from the global analysis by setting all measured values to the number of events expected from the SM we lose constraining power. Again, demonstrating that our analysis strongly benefits from under-fluctuations.

4.3.3 ZH resonance search

The second boosted VH analysis we re-interpret in terms of SMEFT is a CMS resonance search in the process [172]

$$pp \rightarrow ZH \rightarrow e^+ e^- \, b\bar{b} \,. \tag{4.19}$$

We include the non-vector boson fusion (VBF) category with ≤ 1 b-tags and with two b-tags. We find that the two-b category is more constraining than the $\leq 1b$ category. This can happens because the relative size of the SMEFT correction prefers this category.
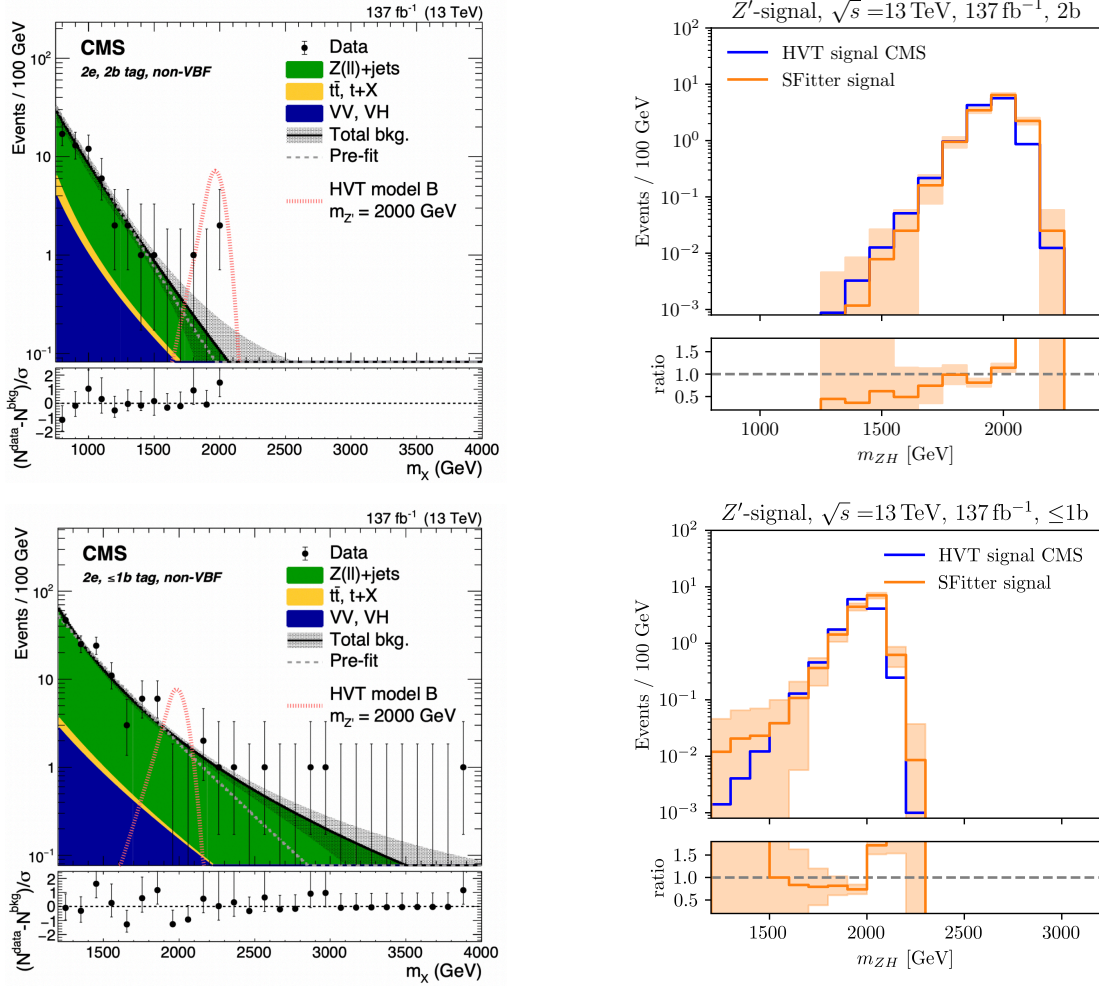
Figure 4.15: Left: measured m_{ZH} distributions for the two b-tagging categories [172]. Right: comparison between the Z' signal quoted by CMS and our estimate. The orange bands show the statistical uncertainty from the Monte Carlo generation.

To determine the number of b-tags in an event, we look at the corresponding fat jet and the number of b-quarks inside the jet.

We validate our analysis simulating events for Z' peak in the heavy vector triplet (HVT), that is used by CMS to illustrate a possible signal,

$$pp \to Z' \to Z_{\ell\ell}H_{bb} .\tag{4.20}$$

This signal has the advantage that it is localized in m_{ZH} and simulated at leading order using `Madgraph5`, which means it is easier to use for calibration than a continuum background. Again, we use `Madgraph5`, `Pythia8`, `FastJet`, and `Delphes` with the standard CMS card at leading order. The combined sample is then compared to the HVT peak shown in Fig. 4.15. We extract the experimental efficiencies after scaling the invariant mass by the same factor 1.05 for both categories. The right panels in Fig. 4.15 show the simulated Z' signal for the two categories, compared with the quoted CMS distributions.

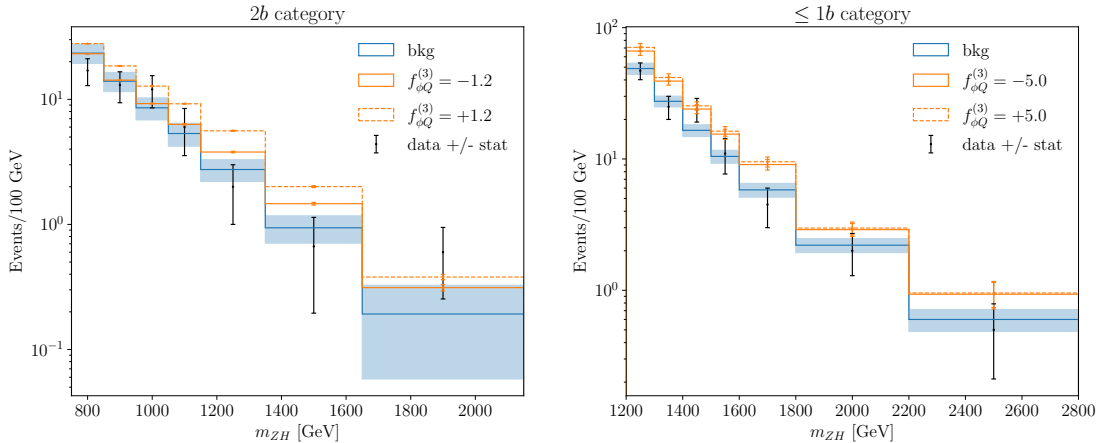The SMEFT signal in the ZH channels is then computed using the same efficiencies

Figure 4.16: Re-binned m_{ZH} distributions for the 2b category (left) and the $\leq 1b$ category implemented in SFITTER, including statistical and systematic uncertainties. We show the complete continuum background and the effect of a finite Wilson coefficient $f_{\phi Q}^{(3)}$.

and the reweighting module in `Madgraph5`. The Z-decays are included in the `Madgraph5` simulation, while the Higgs decays are simulated in `Pythia8`. As before, we ignore SMEFT effects on the $t\bar{t}$ background.

Also for the CMS ZH channel we need to re-bin the m_{ZH} distribution to define a meaningful set of measurements, now with at least two events per bin and separately for the two categories. The results are shown in Fig. 4.16. For each bin we include the systematic and statistical uncertainties from Ref. [172]. In addition, we include different theory uncertainties per bin from the SMEFT prediction and event generation in `Madgraph5`. As discussed in detail for the ATLAS WH analysis, we neglect the correlation between bins.

4.3.4 Boosted Higgs production

Boosted Higgs production, in association with one or more hard jets,

$$pp \to Hj(j) \,, \tag{4.21}$$

has been known to distinguish between a top-induced Higgs-gluon-gluon coupling and the corresponding dimension-6 operator for a long time [174, 175]. It has therefore been suggested as a channel to measure the dimension-6 WC f_{GG} in the presence of a modified top Yukawa coupling f_t [176–179], where it competes with channels like the off-shell Higgs production [180, 181]. In the SFITTER Higgs analysis it can be added to the set of measurements to provide complementary information to the total Higgs production rate. We take the measurement of the Higgs p_T distribution in the $\gamma\gamma$ channel by ATLAS [173].

The main contribution to boosted Higgs production comes from the partonic channel $gg \to Hg$, with subleading corrections from $gg \to Hgg$. This allows us to include SMEFT corrections to $gg \to Hg$ only. They can be separated into rescalings of the top Yukawa coupling, for instance via $\mathcal{O}_{u\phi,33}$, corrections to the top-gluon coupling from $\mathcal{O}_{tG}$, and the effective Higgs-gluon interaction induced by $\mathcal{O}_{GG}$.
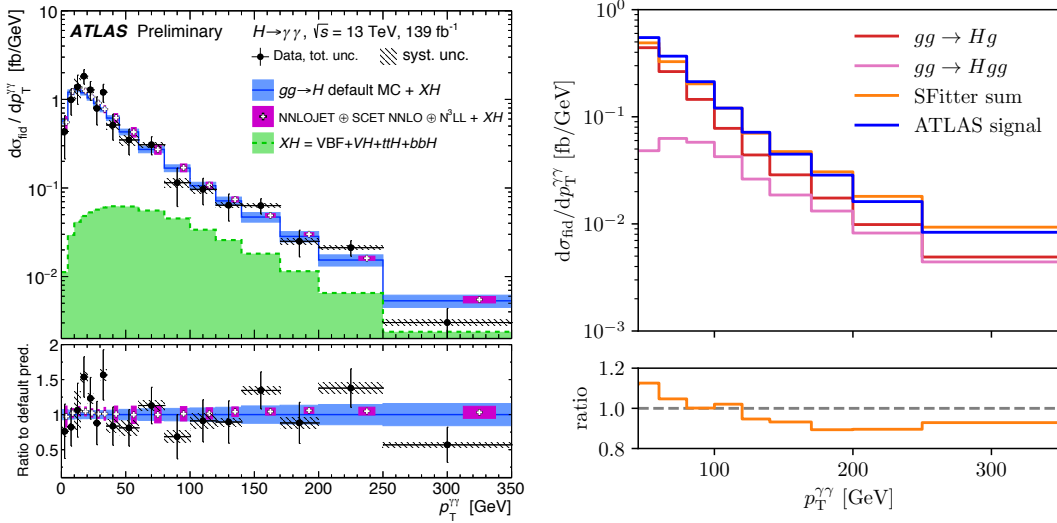
43

Figure 4.17: Left: measured $\mathrm{d}\sigma_{\mathrm{fid}}/\mathrm{d}p_{\mathrm{T}}^{\gamma\gamma}$ distribution [173]. Right: comparison between the the ATLAS distribution and our SM estimate summing contributions from $gg \to Hg$ and $gg \to Hgg$.

Because these effective vertices enter also $t\bar{t}H$ production, these operators lead to a non-trivial interplay in the global analysis. Moreover, as discussed in Sec. 4.3.5 below, f_{tG} is well-constrained by top pair production $pp \to t\bar{t}$. In fact, it constitutes the most significant contact between global top and Higgs analyses [39, 40].

We calibrate the boosted Higgs analysis simulating the SM signal for the partonic sub-channels $gg \to Hg$ and $gg \to Hgg$ using `Madgraph5`. The gluon-initiated channels are simulated at 1-loop, while the quark-initiated one at tree level. For the one-loop simulation we use a fixed renormalization scale $\mu_R = m_H$. This setup is also used for the SMEFT simulations. Figure 4.17 shows the comparison between our simulation and the SM signal estimate provided by ATLAS. We use the same binning as in the original distribution, but omit the bins with $p_{T,\gamma\gamma} < 45$ GeV.

The simulation of SMEFT effects is tackled with different methods. The effect of a shifted top Yukawa is just a rescaling of the SM cross section, that can be easily computed analytically,

$$\frac{\sigma_{\mathrm{SMEFT}}}{\sigma_{\mathrm{SM}}} = \left(1 - \frac{f_t}{\sqrt{2}} \frac{v^2}{\Lambda^2}\right)^2 . \tag{4.22}$$

Second, $\mathcal{O}_{tG}$ also enters the top loops, but induces a different Lorentz structure compared to the SM amplitude. Its contributions are simulated independently using SMEFT@NLO [182] in `Madgraph5`. In the event generation, the EFT operator is renormalized at $\mu_{\mathrm{EFT}} = \mu_R = m_H$.

Finally, $\mathcal{O}_{GG}$ enters at the tree level. Because the pure interference between tree and loop diagrams can not be generated directly in `Madgraph5`, we choose to simulate both the linear and the squared term with a modified `loop_sm` universal FEYNRULES output (UFO) model, where the point-like Higgs-gluon vertices are mimicked by sending the bottom quark mass and Yukawa coupling to 15 TeV. We verified that any value larger
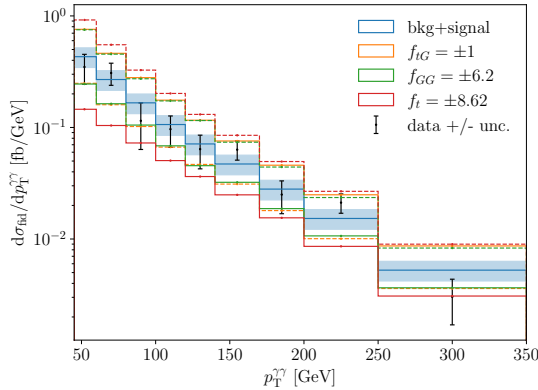
Figure 4.18: Reconstructed $p_{T,H}$ distribution implemented in SFITTER, including statistical and systematic uncertainties as well as additional uncertainties on our prediction. We show the complete continuum of signal and background and the effect of three finite WCs f_t, f_{tG} and f_{GG}. The negative values are represented by dashed lines and the positive values by solid lines.

than 10 TeV gives equivalent results. This way the simulation is formally at one loop for all terms. The results of this approximation were cross-checked against the analytic results in Refs. [174, 175] for the interference and against the tree-level simulation for the pure square.

The mixed quadratic terms, i.e. the interferences between two operators, can be computed analytically for the combination of $\mathcal{O}_{tG}$ or $\mathcal{O}_{GG}$ with a shifted Yukawa coupling. The combination of f_{tG} and f_{GG} needs to be simulated independently, in our case using using SMEFT@NLO and the reweighting module in `Madgraph5`.

In Fig. 4.18 we show the impact of four relevant SMEFT coefficients on the kinematic distribution we implement in SFITTER. For each bin we include the systematic and statistical uncertainties from Ref. [173], as well as an additional 20% theory uncertainty reflecting the scale uncertainty on the SMEFT prediction.

4.3.5 From the top

From the combined top-Higgs analyses [39, 40] we know that the Higgs-gauge sector and the top sector can not be treated completely independently. The two operators

$$\mathcal{O}_{u\phi,33} = \phi^\dagger\phi \, \bar{Q}_3\tilde{\phi}u_{R,3} \qquad \text{and} \qquad \mathcal{O}_{tG} = ig_s(\bar{Q}_3\sigma^{\mu\nu}T^A u_{R,3}) \, \tilde{\phi}G^A_{\mu\nu} \qquad (4.23)$$

contribute to top pair and associated $t\bar{t}H$ production and are, at the same time, crucial to interpret gluon-fusion Higgs production, together with the Higgs-related operator $\mathcal{O}_{GG}$, as discussed above. By the definition of top-sector and Higgs-sector SMEFT analyses in SFITTER, $\mathcal{O}_{tG}$ is covered by the top analysis, while we keep $\mathcal{O}_{u\phi,33}$ as part of the Higgs analysis, together with a complete treatment of $t\bar{t}H$ production. This means we can include the limits on f_{tG} from the dedicated SFITTER analysis of the top sector [38] using its 1-dimensional profile likelihood. We implement these constraints as an external measurement or prior. The corresponding profile likelihood is shown in Fig. 4.19. It consists of 100 data points which are dense enough that we can linearly interpolate between them.

We choose the range in f_{tG} to cover extremely small log-likelihoods, to avoid numerical issues in the combined analysis. Still, while it is very unlikely to occur, we also want to describe points outside of this range, so we extrapolate the log-likelihood further with two quadratic fits; one fitted to negative WCs and one fitted to positive WC. A quadratic fit in this context means exponentially suppressed Gaussian tails.

4.3.6 Rates and signal strengths

In addition to the new kinematic measurements above, we update the set of Higgs rate measurements of Ref. [36], adding those listed in Tab. 4.1. The two $H \to \tau\tau$ and three out of four $H \to$ inv measurements are completely new constraints, while the others update results included in our previous analysis. The first column indicates which production channels were implemented in SFITTER. We do not always use all the channels covered in a given ATLAS or CMS paper, if some of them are clearly subleading or some of them appear impossible to implement in the necessary details. Production channels in parentheses are numerically subleading, but were retained nevertheless.

The systematic and statistical uncertainties of the new measurements are typically smaller compared to the older ones. On the other hand, we attempt a more comprehensive
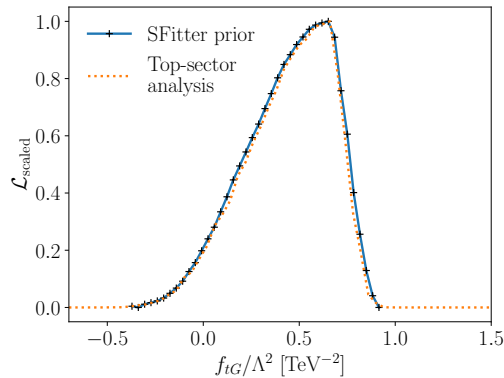

Figure 4.19: Profile likelihood for f_{tG} from the SFITTER top-sector analysis [38].

Production	Decay	ATLAS	CMS
All	$H \to \gamma\gamma$	[183]	[184]
ZH	$H \to$ inv	[185]	[186]
VBF (ggF, VH)	$H \to$ inv	[187]	
VBF (ggF, ZH, $t\bar{t}H$)	$H \to$ inv		[188]
All	$H \to \tau\tau$	[189]	
VH	$H \to \tau\tau$		[190]
ggF, VBF	$H \to WW$	[171]	
ggF, VBF, VH	$H \to WW$		[191]
WH, ZH	$H \to b\bar{b}$	[192]	
ggF, VBF (VH, ttH)	$H \to \mu\mu$		[193]

Table 4.1: List of the new Run 2 Higgs measurements included in this analysis, we denote $V = W, Z$.

and conservative estimate of the theory uncertainties, given the available information. In Ref. [36] we typically discarded many theory uncertainties on the signal quoted in the actual papers and replaced them with the leading uncertainty on the complete signal prediction from the Higgs cross section working group (HXSWG) [194–196], added linearly as expected for uncorrelated flat uncertainties combined by profiling. In our new, comprehensive treatment, all theory uncertainties quoted by the analyses are retained. We include them separately and combine them. In addition, we include the uncertainties reported by the HXSWG [194–196] as the uncertainty on our SFITTER prediction, again split by contribution and ready to be profiled over or marginalized.

We illustrate the implementation procedure in some more detail only for the recent Run-2 $H \to WW$ analysis by CMS [191]. Among the results presented, we implement the four signal strength measurements. Because they are reported for individual production modes (and not only in the simplified template cross sections (STXS) binning), they can be directly compared to the known expressions for Higgs production rates in the SMEFT, without re-deriving. These have been long implemented in SFITTER for the main Higgs production channels (ggF, VBF, WH, ZH, ttH) and decays ($b\bar{b}$, WW, gg, $\tau\tau$, ZZ, $\gamma\gamma$, $Z\gamma$, $\mu\mu$). A re-derivation of the SMEFT expression can also be avoided in cases where the final results are not given for specific production channels, but the expected signal contribution from each production channel is provided.

The key ingredient to SFITTER is a detailed breakdown of all uncertainties. This is crucial in order to obtain the best possible approximation of the full experimental likelihood. For Ref. [191] we consider different uncertainties for each production channel, that are reported in the paper and in the corresponding HepData entry.

The statistical uncertainty is taken from the experimental paper, symmetrized and implemented as Poisson or Gaussian distribution. For experimental systematics, SFITTER provides 31 predefined categories of Gaussian uncertainties, correlated across measurements and, where appropriate, across experiments. All uncertainties belonging to the same category are added in quadrature. The categories used to implement the CMS analysis cover luminosity, detector effects, lepton reconstruction, and b-tagging. Detector effects combine the jet energy scale and resolution uncertainties, as well as the missing transverse momentum scale uncertainty. Whenever the experimental papers quote significant uncertainties that do not fit any predefined category, we add them as an uncorrelated Gaussians, but this is not the case for the analysis of Ref. [191].

Theoretical uncertainties are typically implemented with flat uncorrelated likelihoods. One exception is the Monte Carlo statistics uncertainty, which we usually treat as an uncorrelated Gaussian. The CMS analysis quotes five theoretical uncertainties, that are all introduced independently. In addition, we have six theoretical uncertainties on the SFITTER prediction: three on the production rate and three on the decay branching ratio, following the HXSWG prescription [194–196].

As a final step we compare the systematic uncertainties quoted on the final result with the sum of the uncertainties implemented in SFITTER. If we are missing information for example on the correlations, our implementation might not be conservative, so we introduce an additional uncorrelated Gaussian uncertainty to compensate. This happens for the CMS reference analysis in the ZH channel. For this measurement we implement two uncorrelated Gaussian uncertainties, three correlated Gaussian uncertainties, plus the eleven flat uncertainties.
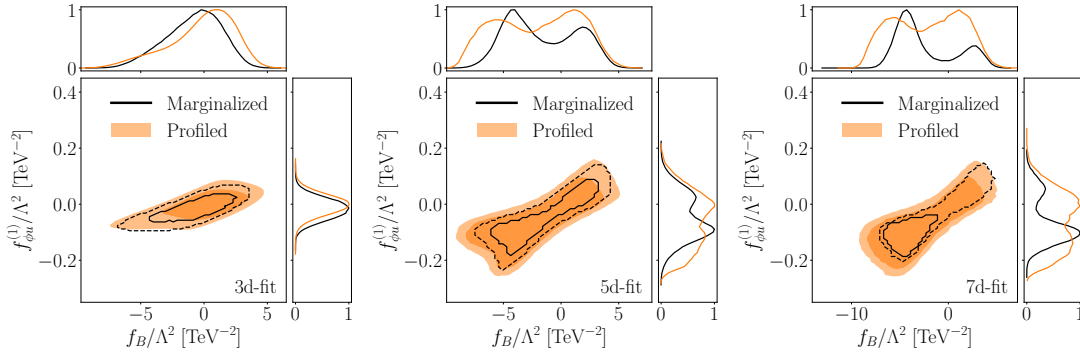
Figure 4.20: SFITTER analysis with different SMEFT models describing the full Run 2 dataset, including the boosted WW production.

4.4 Global SFitter analysis

After validating the marginalization technique in SFITTER and introducing a set of promising new observables, we can provide the final global analysis of the Higgs and electroweak sector after Run 2, including the leading link to the top sector. To be conservative, we will compare all our results with a profile likelihood treatment. We will find and explain differences of the two methods facing the same extended dataset.

4.4.1 Marginalization vs profiling complications

While in Sec. 4.2 we have found that for the dataset of Ref. [36] the marginalization and profiling approaches lead to, essentially, identical results, one analysis implemented in SFITTER as part of Ref. [2] actually leads to significant differences. The data driving this separation of profiling and marginalization is the m_{WW} distribution measured by ATLAS [197], shown in the left panel of Fig. 4.11. It has the unique feature of a sizeable under-fluctuation in the last bin.

Such an under-fluctuation is challenging to accommodate in the SMEFT. First, under-fluctuations can only be explained by operators with large interference terms, where the WCs have to be carefully tuned to be large enough to explain a sizeable effect and small enough to not be dominated by dimension-6 squared contributions. Second, a localized under-fluctuation in only one bin of one kinematic distribution requires a subtle balance of several WCs, to control all other bins in all other di-boson and VH channels.

In Fig. 4.20 we show low-dimensional analyses of the full Run 2 dataset including the WW kinematics shown in Fig. 4.11, constraining three, five and seven Wilson coefficients. For the three parameters $\{f_B, f_{\phi u}^{(1)}, f_W\}$ we see that the maximum of the likelihood is perfectly compatible with the SM. The reason is that the SMEFT model is not flexible enough to accommodate the under-fluctuation, so we only encounter the issue when we look at the value of the likelihood in the maximum. Adding first $\{f_{\phi Q}^{(1)}, f_{\phi Q}^{(3)}\}$ and then $\{f_{\phi d}^{(1)}, f_{3W}\}$ to the SMEFT model allows us to accommodate the under-fluctuation, leading to a second likelihood maximum.

When we compare the two likelihood maxima, differences between the profiling and the marginalization appear. This is not surprising, given that the two methods ask different questions. By definition, the profile likelihood identifies the most likely parameter point,
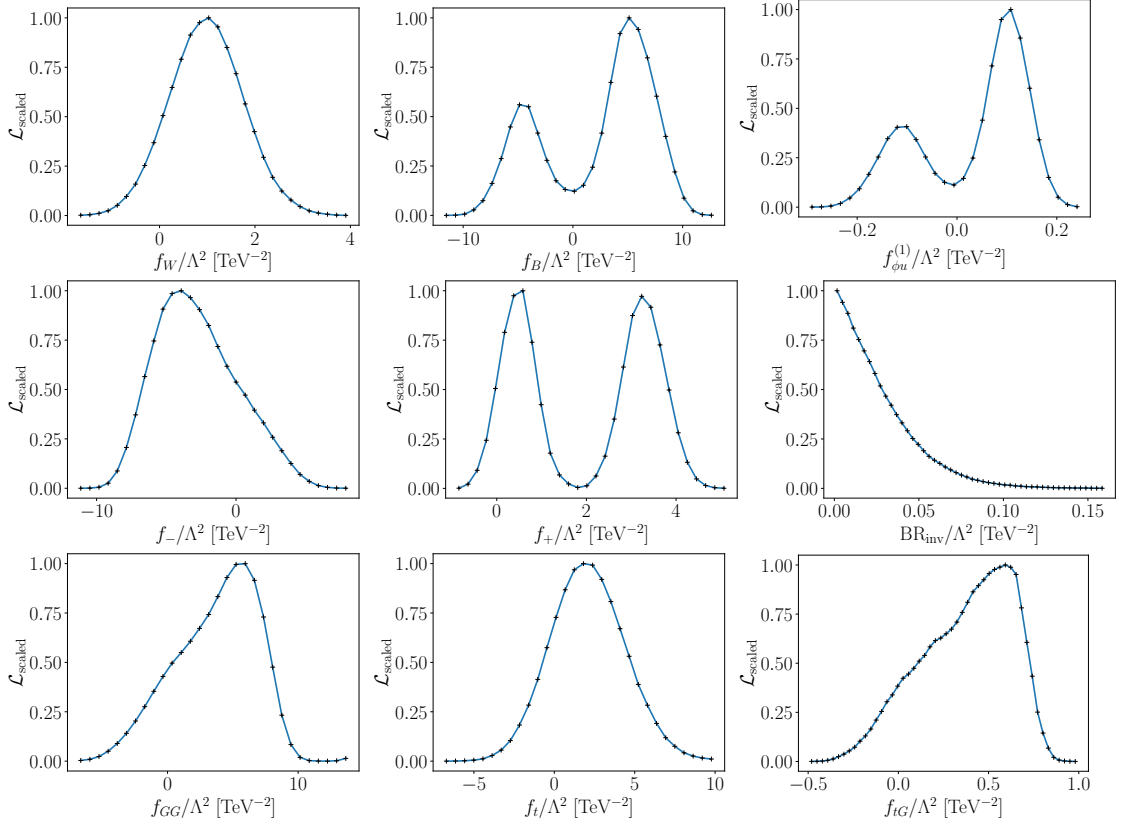
Figure 4.21: Set of marginalized likelihoods for the 21-dimensional SFITTER analysis including the full set of measurements.

which according to Fig. 4.20 is close to the SM point, $f_B \approx 0 \approx f_{\phi u}^{(1)}$. This does not change when we increase the operator basis or expressivity of the SMEFT model. The marginalization adds volume effects in the space of Wilson coefficients, and they increasingly prefer the non-SM maximum once the SMEFT model is flexible enough to explain the under-fluctuation. Consequently, the marginalized analysis proceeds to challenge the SM in favor of an alternative SMEFT parameter point.

4.4.2 Full analysis

After identifying and understanding the issue with marginalized likelihoods for the updated dataset we now perform the full, 21-dimensional parameters analysis on all available data. The theory framework is defined by the Lagrangian in Eq. (2.3). The dataset consists of all measurements from Ref. [36], combined with the new and updated channels described in Sec. 4.3. We will discuss the standard profile likelihood results below, in a first step we focus on the marginalization. In Fig. 4.21 we show a set of 1-dimensional marginalized likelihoods. In the first row we show three WCs affected by the under-fluctuation in m_{WW}, as discussed in the previous Sec. 4.4.1. While the marginalized likelihood for f_W follows a standard single-mode distribution, those for f_B and $f_{\phi u}^{(1)}$, for example, show two distinct modes accommodating the observed under-fluctuation.

In the second row we show the alternative maximum in f_+ we already observed for the dataset from Ref. [36] and which we discuss in Fig. 4.6 of Sec. 4.2. For the final

SFITTER result we will remove the second maximum as an expansion around the wrong SMEFT limit. We also see that the invisible Higgs width is strongly constrained, even after we account for a modified Higgs production process rather than assuming SM Higgs production combined with the exotic invisible Higgs decay.

In the last row we show the effect of including $\mathcal{O}_{tG}$ in the Higgs analysis. Comparing the limit on f_{tG} to its prior in Fig. 4.19 we see that this parameter gains essentially nothing from the Higgs measurements, but it will broaden the limits on the correlated parameter f_{GG} affecting gluon-fusion Higgs production.

To follow up on the discussion of Fig. 4.20 we show a more complete set of 2-dimensional marginalized likelihoods related to the m_{WW} under-fluctuation in Fig. 4.22. In the full analysis the correlation does not just affect $f_{\phi u}^{(1)}$, but the full range of gauge-fermion operators. This is expected from the argument that we need to carefully tune many WCs to accommodate a deviation in a single di-boson process in a single bin of the high-invariant-mass distribution. As mentioned before, the apparent signal for physics beyond the Standard Model is an artifact of the marginalization and its volume effects, and can not be reproduced with the profile likelihood. Note that this does not mean the marginalization is wrong or wrongly done, this difference just reflects the two methods asking different questions.

To study the impact of the critical WW-resonance analysis on our global analysis we show a set of marginalized likelihoods with and without this analysis, i.e. with and without the entire m_{WW} distribution. Obviously, removing this distribution also removes the secondary maximum structure, as we immediately see in Fig. 4.23. Removing the entire distribution replaces the marginalized likelihoods for f_B and $f_{\phi u}^{(1)}$ by their broad envelopes, still correlated, but without the distinctive maxima. For f_W the additional observable has limited impact, for $f_{\phi d}^{(1)}$ is leads to a smaller uncertainties combined with a shifted maximum, and for f_{3W} the WW-analysis provides key information.

Finally, in Fig. 4.24 we compare the 1-dimensional marginalized likelihoods with the corresponding profile likelihoods for a set of WCs. For f_B and $f_{\phi u}^{(1)}$ we see the difference in the treatment of the secondary likelihood maximum, while f_W serves as an example for the many parameters where the two methods give the same results, as discussed in detail in Sec. 4.2 and Fig. 4.2. Indeed, the results from the two methods only disagree when the likelihoods develop secondary maxima.
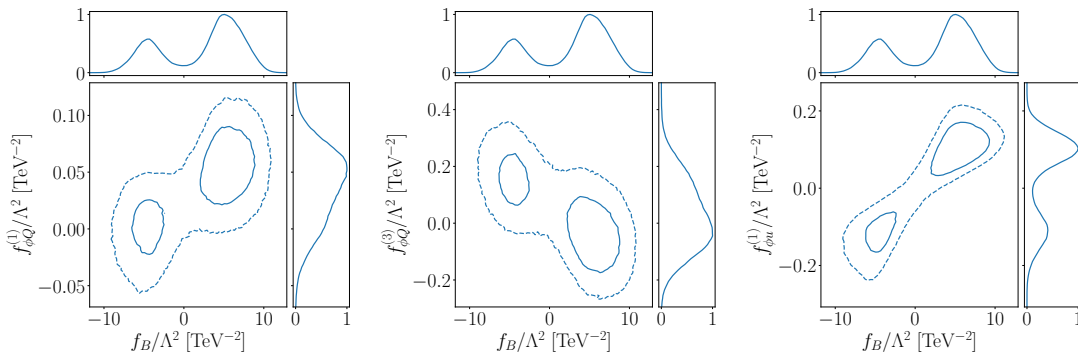

Figure 4.22: Set of marginalized correlations for the 21-dimensional SFITTER analysis including the full set of measurements. The solid and dashed lines show $\Delta\chi^2 = 2$ and 7 respectively.
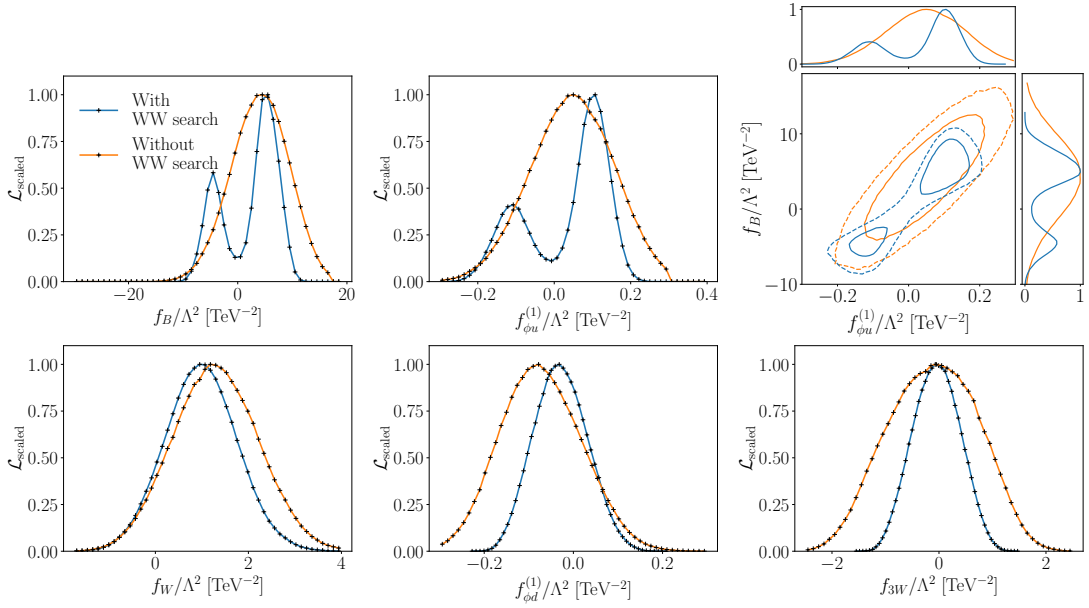
Figure 4.23: Set of marginalized likelihoods for the 21-dimensional SFITTER analysis with and without the ATLAS WW resonance search altogether.

Moving on with the effects observed in Fig. 4.21 we can look at the top-Higgs sector with f_{GG}, f_t, and the added f_{tG}. These three WCs are constrained by the Higgs production in gluon fusion, associated top-Higgs production, and top pair production through the prior shown in Fig. 4.19. We have already seen that this prior is practically identical to the final outcome in Fig. 4.21. Nevertheless, we can ask what the impact of the boosted Higgs production process is, given that it should provide a second measurement of the three WCs with different relative weights. In Fig. 4.25 we show the results of the 21-dimensional SFITTER analysis with and without the new boosted Higgs measurement introduced in Sec. 4.3.4. Unfortunately, the likelihood distributions are similar, corresponding to our expectation from the limited statistics of this measurement and the limited range in $p_{T,H}$, where significant differences can only be expected for $p_{T,H} > 250$ GeV [180], and even for this kinematic range it is not clear how well the measurement separates effects from f_{GG} and f_{tG}, while the f_t measurement is completely dominated by $t\bar{t}H$ production.

Even though completely justified, the only visible effect of including f_{tG} in the Higgs analysis is to wash out the limit on f_{GG}. In Fig. 4.26 we first show the change on the 1-dimensional marginalized likelihood of f_{GG} when we remove f_{tG} from the SFITTER
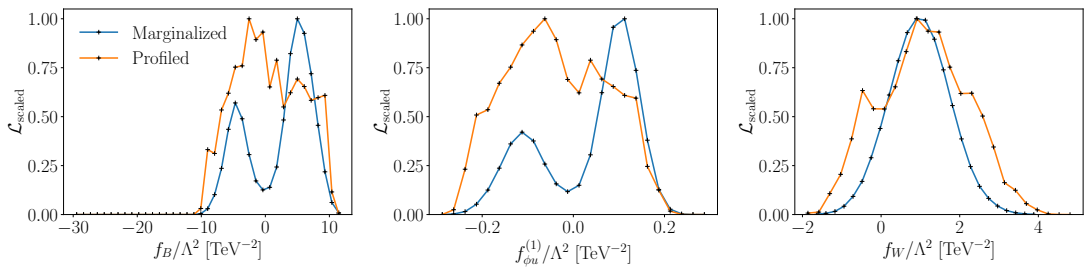

Figure 4.24: Set of marginalized and profiled likelihoods for the 21-dimensional SFITTER analysis with the ATLAS WW resonance search.
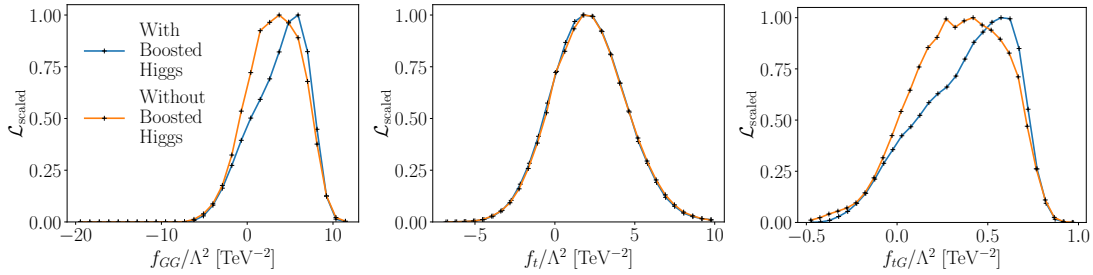
Figure 4.25: Set of marginalized likelihoods for the 21-dimensional SFITTER analysis with and without the boosted Higgs analysis.

analysis. Indeed, the measurement of f_{GG} becomes much better. This is explained by the strong correlation between f_{GG} and f_{tG} shown in the right panel.

After the in-depth discussion of all features we show the 68% and 95%CL limits from the 21-dimensional SFITTER analysis with the full updated dataset in Fig. 4.27. To extract these limits we start with the respective 1-dimensional marginal or profile likelihood, identify the maximum, and move outward keeping the likelihood values on the left and the right border of the integral the same. If there exists an additional peak, we compute the integral under the likelihood for the part of the curve above a given likelihood threshold. The 68% and 95%CL error bars are then defined the same way for the marginal and profile likelihood.

The profile likelihood results in Fig. 4.27 provide an update of the limits shown in Fig. 4.2 [36]. We emphasize that this update does not automatically mean an improvement of the limits, because of our more comprehensive uncertainty treatment, the added operator $\mathcal{O}_{tG}$, and the now measured Yukawa coupling f_μ. Computing the uncertainties on the Wilson coefficients which are all in agreement with the Standard Model at least for the profile likelihood approach, we remove modes around non-SM likelihood maxima. Those appear through sign flips in Yukawa couplings and in f_+ and would require order-one effects from new physics. We safely assume that new physics with this kind of effects would have been observed somewhere already.

In Fig. 4.27 we see that all results from the marginalization and profiling approach are consistent with each other. The only kind-of-significant deviation appears in f_B and
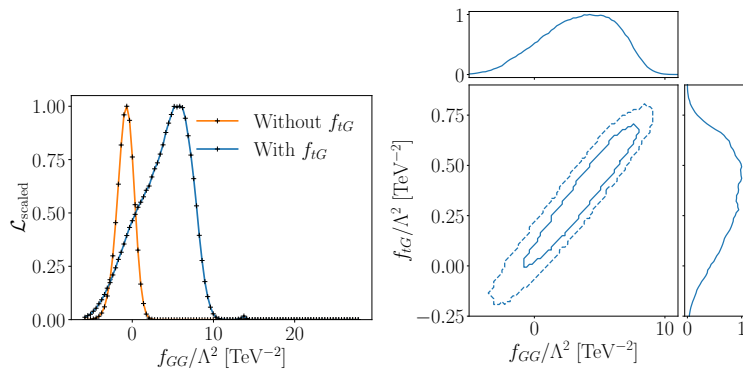

Figure 4.26: Left: marginalized likelihoods for the SFITTER analysis with and without f_{tG}, using the same dataset; Right: marginalized correlation for the 21-dimensional SFITTER analysis.
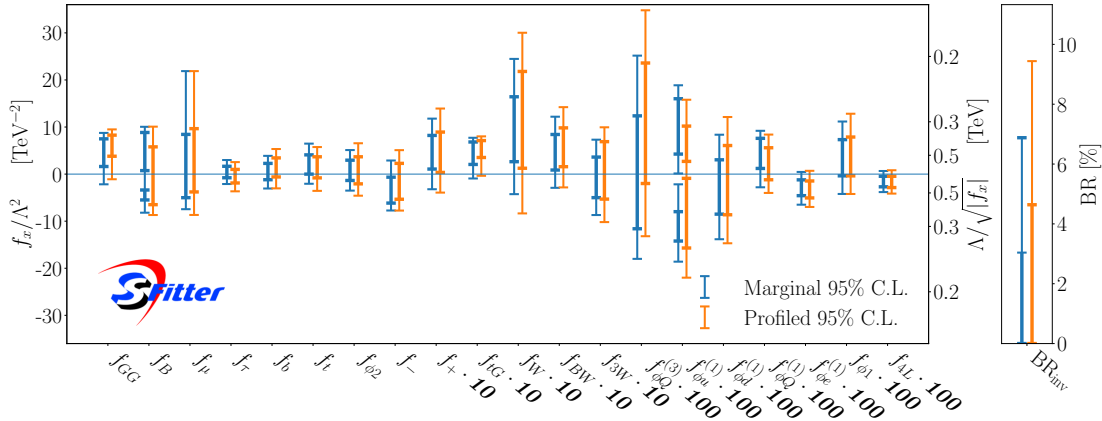
Figure 4.27: Comparison of 21-dimensional SFITTER analysis with all updated measurements included. We show the 68% and 95%CL error bars from consistent marginalization and profile likelihood treatments of all nuisance parameters and WCs.

the correlated gauge-fermion operators like $f_{\phi u}^{(1)}$. The reason for this discrepancy can be traced back to an under-fluctuation in the m_{WW} measurement and actual differences between the likelihood and Bayesian approaches.

Projected limits for the high-luminosity LHC (HL-LHC) are shown in Appendix A. Appendix B gives the numerical values of the intervals presented in Fig. 4.27.

4.5 Outlook

Global SMEFT analyses are the first step into the direction of interpreting all LHC data on hard scattering process in a common framework. They allow us to combine rate and kinematic measurements from the Higgs-gauge sector, the top sector, jet production, exotics searches, even including parton densities and flavor physics. They can be considered improved bin-wise analyses of LHC measurements, but with a consistent effective theory framework. This framework allows us to provide precision predictions matching the precision of the data we analyze, and it ensures that their result is relevant fundamental physics. Because any realistic effective theory description involves a truncation in dimensionality, SMEFT results always have to be considered in relation to the fundamental physics models they represent.

From a brief look at the analyzed data we know that our SMEFT analysis of the electroweak gauge and Higgs sector will not describe established anomalies, but serve as a consistent, global limit-setting tool. This makes it even more important to treat all uncertainties, statistical, systematic, and theory, completely and consistently. Technically, this leads us directly to the question if we want to use a profile likelihood or a Bayesian marginalization treatment. Because the two methods ask different questions, it is not at all clear that technically correct analyses following the two approaches lead to the same results. We have shown, for a first time, what the current challenges in global LHC analyses are and how the two methods do turn up slight differences.

We have started with an in-depth discussion of the current challenges in the Higgs and electroweak data and the corresponding validation of the marginalization in SFITTER, in

comparison to our classic profile likelihoods. Using the established dataset of Ref. [36] we have shown that the two methods give extremely similar results. We have also found that for this dataset the exact treatment of the theory uncertainties is not a leading problem, while a correct treatment of correlations of the measurements and the uncertainties is crucial.

Next, we have updated this dataset, including a set of kinematic di-boson measurements and boosted Higgs production. These measurements allow us to constrain operators with a modified Lorentz structure especially well. Kinematic distributions from di-boson resonance searches probe the largest momentum transfers of our SFITTER dataset, but their interpretation in terms of SMEFT operators requires significant effort. A systematic publication of the corresponding likelihood by ATLAS and CMS would fundamentally change the appreciation for these analyses, from failed resonance searches to the most exciting SMEFT results.

Accidentally, the updated dataset also leads to differences in the marginalization and profiling treatments of the same exclusive likelihood. The measurement driving this difference is an under-fluctuation in the tail of the kinematic m_{WW} distribution. Under-fluctuations are difficult to reconcile with SMEFT analyses, because they require a balance between linear and squared operator contributions. To complicate things, a sizeable number of kinematic distributions probes large momentum transfer, all consistent with the Standard Model. For a small number of WCs one under-fluctuation will just lead to a poor log-likelihood value in the SM-like likelihood maximum. A larger number of WCs defines a powerful model which accommodated this deviation. For the final result, the complex correlations between WCs lead to volume effects in the marginalization, which, expectedly, separated the final profile likelihood and marginalized results.

From UV models to SMEFT and back?

The SMEFT global analysis framework established in Chaps. 3 and 4 can be extended to perform UV model analyses.

In this chapter, we perform a global analysis for the heavy vector triplet (HVT) model through a SMEFT framework. The essential piece that makes this possible is the matching of the model onto the SMEFT at one-loop level, which is derived using functional methods. The matching at one-loop level introduces an unphysical matching scale, which we argue should be treated as a theory uncertainty, i.e. varied within a range and profiled over. This matching uncertainty is shown to have a great impact on the limits set on one of the UV model parameters. Finally, we present the results of our global analysis in the HVT model space obtained through a SMEFT framework. We discuss the impact of high kinematic distributions and the complementarity between limits from direct searches and those set through a SMEFT framework.

Note that, because this study was technically published before the one in Chap. 4, the basis is reduced ($f_{tG} = f_\mu = 0$) and all the results use the profiling treatment.

The research presented in this chapter has been published in Ref. [2]. The work was conducted in collaboration with Ilaria Brivio, Sebastian Bruggisser, Wolfgang Kilian, Michael Krämer, Michel Luchmann, Tilman Plehn, and Benjamin Summ. All figures and tables as well as a significant part of the text are identical to the content of this publication.

5.1 Introduction

The Higgs discovery [4,5] and many measurements of the Higgs Lagrangian [159] indicate that the SM with its single, weakly interacting Higgs boson might well be the correct effective theory around the electroweak scale. However, the SM is extremely unlikely to be the full story. Many theoretical considerations, including electroweak baryogenesis, dark matter, or neutrino mass generation, point to an extended electroweak or scalar sector. To avoid a bias through a specific, pre-selected signal hypothesis, modern LHC searches for BSM physics are often conducted in the SMEFT [160]. Because of its vast operator landscape, the corresponding experimental searches [198, 199] and global analyses [36, 40–42, 47, 48, 107] provide a comprehensive probe of rates and kinematic patterns in LHC processes.

One of the complications of SMEFT analyses of LHC data is that the effective theory truncated at dimension six has a limited validity range, and that LHC measurements span

a large energy range. Moreover, even if we assume the SMEFT to be generally valid, it is not clear how much information on a full BSM model is lost when we confront it with LHC data via a truncated SMEFT Lagrangian rather than the original full model. Combining these questions, it is instructive to consider concrete, albeit simplified, BSM models and examine the limits extracted through a SMEFT interpretation matched to these models in comparison with the constraints obtained from direct searches [41, 94–97, 200–203].

The naive expectation behind SMEFT analyses is that we can use the complete, correlated information on the Wilson coefficients (WCs) from a global analysis and derive limits on any BSM model through matching. However, if the BSM scale is not sufficiently well-separated from the electroweak (EW) scale, an interpretation based on the SMEFT Lagrangian truncated at dimension six will likely give inaccurate results [204, 205]. The theory uncertainties related to the matching to full models are usually not accounted for in global analyses, which instead take their Lagrangian as a fixed interpretation framework. In general, limits derived on BSM models through a SMEFT framework using the same data and with all uncertainties accounted for will differ from limits derived on the full model directly, where the former can be significantly weaker or stronger than the latter.

This work aims at exploring the complementarity of the two analysis strategies and at highlighting general aspects that emerge when the SMEFT results are related to a concrete BSM scenario. We address this question for a global analysis of electroweak, di-boson and Higgs measurements, matching the relevant WCs to the UV-model at one loop, using functional matching methods. We use the SFITTER framework and include a proper estimate of a new and non-negligible theory uncertainty from the variation of the matching scale. As a UV-model we use a triplet-extended gauge sector [200, 206–209] a standard scenario when it comes to motivating the SMEFT approach to the Higgs and electroweak sector. Such a triplet model can be linked for instance to the weakly coupled gauge group $SU(3) \times SU(2) \times SU(2) \times U(1)$ [210] or deconstructed extra dimensions [211].

The chapter is organized as follows: in Sec. 5.2 we review the basics of functional one-loop matching, we define the gauge triplet model under study, and we provide details about the SFITTER setup. In Sec. 5.3 we discuss the decoupling limit of the new heavy states and the relevance of the matching scale choice. The impact of these two aspects on the global analysis is illustrated via simplified fits. In Sec. 5.4 we present the results of a global fit to the full vector triplet model, based on the dimension-6 SMEFT Lagrangian, and compare our results with limits obtained from direct searches. We conclude in Sec. 5.5.

5.2 Basics

In this section, we briefly review the one-loop matching procedure, the UV-model, as well as the SFITTER setup.

5.2.1 One-loop matching: generic approach

The methods of constructing and matching effective-field theories [51, 212] have been in use for more than four decades [213–216]. Generic expressions for the low-energy effective action of a gauge theory at the one-loop order were derived in the 80s [217]. More recently, the approach has been further explored, particularly within the context of SMEFT [144–157].

We consider a UV model which can be defined in terms of light fields ψ and heavy fields Ψ, and which supports a perturbative expansion based on a local Lagrangian. Heavy fields are characterized by the condition that the support of their spectral functions vanishes below a certain threshold. We may identify the threshold with a mass M, typically the lightest mass that belongs to the heavy spectrum. The remaining fields are understood as light fields.

The UV model is expressible in terms of an effective action $\Gamma_{\mathrm{UV}}[\psi, \Psi]$, the generating functional of its one-particle irreducible (1PI) vertex functions. If fields of spin higher than $1/2$ are involved, or if global symmetries are present, it is constrained to be a solution of a Slavnov-Taylor identity. By assumption, Γ_{UV} is calculable in a loop expansion from a local Lagrangian $\mathcal{L}_{\mathrm{UV}}(\psi(x), \Psi(x))$ with a finite number of fields and parameters. The parameters depend on the choice of a regularization and renormalization scheme and are redefined order by order by suitable renormalization conditions. This includes resolving inherent ambiguities associated with field reparameterizations, such as wave-function renormalization and terms vanishing by equations of motion.

The EFT is likewise expressible in terms of an effective action $\Gamma_{\mathrm{EFT}}[\psi]$, a functional of the light fields only. Again, we assume that a perturbative loop expansion is possible, and that it can be computed from a local Lagrangian $\mathcal{L}_{\mathrm{EFT}}(\psi(x))$. The number of parameters of $\mathcal{L}_{\mathrm{EFT}}$ is intended to be finite, but it increases without bounds with the accuracy that we want to implement via matching conditions. To keep the EFT parameter set manageable, we have to define an organizing principle which amounts to a series of approximations, and a prescription to truncate this series at a certain order.

To find the EFT Lagrangian iteratively, one introduces the one-light-particle irreducible (1LPI) effective action $\Gamma_{\mathrm{L,UV}}[\psi]$. Formally, this is a double Legendre transform of $\Gamma_{\mathrm{UV}}[\psi, \Psi]$; in practice, it amounts to absorbing a maximal set of independent heavy-field propagators in the skeleton expansion of S-matrix elements. This results in redefined light-field effective vertices. By contrast, the light-field propagators are kept explicit. In general they still carry a mixture of light and residual heavy degrees of freedom, depending on the precise definition of the original UV model. Like the original effective action, $\Gamma_{\mathrm{L,UV}}[\psi]$ depends on conventions regarding renormalization and handling the equations of motion. In terms of this entity, the matching condition reads

$$\Gamma_{\mathrm{L,UV}}[\psi] = \Gamma_{\mathrm{EFT}}[\psi] + \Delta\Gamma[\psi] . \tag{5.1}$$

The matching error $\Delta\Gamma[\psi]$ describes a set of vertex-function corrections $\Delta\Gamma_i(x)$ that are not calculable from a local Lagrangian involving light fields only. The matching procedure succeeds if, in momentum space, all contributions to this error are sufficiently power-suppressed at low energy,

$$\Delta\Gamma_i(p) < c|p|^k , \tag{5.2}$$

where p is any light-particle mass or momentum component.

At the tree level, the 1LPI effective action $\Gamma_{\mathrm{L,UV}}^{(0)}[\psi]$ of the UV model can be derived by simple variable changes, applying the equations of motion. Unless the ψ multiplets are incomplete under a symmetry, the result satisfies the tree-level Slavnov-Taylor identity with only light fields taken into account. The tree-level effective action $S_{\mathrm{EFT}}[\psi] = \Gamma_{\mathrm{EFT}}^{(0)}[\psi]$ is evaluated, to arbitrary order, by means of a momentum-space Taylor expansion of the 1LPI effective action on the l.h.s. of Eq. (5.1). In this expansion, residual heavy degrees of freedom are naturally removed from the tree-level light-field propagators. The latter

assume their canonical tree-level form while any extra terms are shifted to the interaction part of $S_{\text{EFT}}[\psi]$.

The operator content of the tree-level effective action $S_{\text{EFT}}[\psi]$ can be determined independently by algebraic methods. Their coefficients are fixed by a term-by-term comparison with the vertices of $\Gamma^{(0)}_{\text{L,UV}}$. The symmetries are preserved in this expansion if covariant derivatives are used consistently. At one loop, new contributions to the UV effective action arise which are generically non-local, and can be formally summarized as

$$\Gamma^{1\ell}_{\text{UV}}[\psi, \Psi] = ic_s \operatorname{Tr} \log \left(-\frac{\delta^2 S_{\text{UV}}[\psi, \Psi]}{\delta^2(\psi, \Psi)} \right) , \qquad (5.3)$$

where the trace is integrated over all field components at all space-time points and c_s accounts for the statistics of the fields that are integrated over. This evaluates to the sum of all one-loop Feynman graphs with external fields attached. In expressions of this kind, the external field insertions act as bookkeeping devices, or background fields [218–226]. This allows for employing gauges and conventions that distinguish between internal and external lines, a generic feature of working with 1PI vertex functions. This means in particular that, with respect to the background fields, a manifestly gauge-invariant effective action can be computed [227, 228]. The trace is in general UV divergent and requires the application of a regularization scheme and the addition of local counterterms, such as dimensional regularization and minimal subtraction.

To match the UV model to the EFT at the one-loop order, we have to evaluate Eq. (5.1) again. Initially,

$$\Delta\Gamma^{1\ell}[\psi] = ic_s \operatorname{Tr} \left[\log \left(-\frac{\delta^2 S_{\text{UV}}[\psi, \Psi]}{\delta^2(\psi, \Psi)} \right) - \log \left(-\frac{\delta^2 S^{(0)}_{\text{EFT}}[\psi]}{\delta^2 \psi} \right) \right]\Bigg|_{\Psi=0} , \qquad (5.4)$$

where the formal trace includes the integral over all one-loop diagrams which are 1LPI and do not contain open external Ψ lines. Because $S^{(0)}_{\text{EFT}} = \Gamma^{(0)}_{\text{EFT}} = \Gamma^{(0)}_{\text{L,UV}} + \mathcal{O}(|p|^k)$, the difference is well-behaved in the infrared (IR). Loops of canonical light propagators only would exactly cancel between the two terms, but since the light-field propagators need not coincide between the two Lagrangians, we have to be careful to take all terms into account. In any case, due to the IR cancellation the one-loop functional Eq. (5.4) again admits a Taylor expansion up to the order of the previous tree-level truncation. The result can be expressed as a finite set of local terms that modify the coefficients of terms which are already present in the generic effective Lagrangian of the tree-level EFT. They are absorbed in $S_{\text{EFT}}[\psi]$,

$$S^{1\ell}_{\text{EFT}}[\psi] = -\Delta\Gamma^{1\ell}[\psi]\Big|_{\text{local, truncated}} , \qquad (5.5)$$

and disappear from Eq. (5.4). In effect, the remainder still contains all non-local parts of the matching error but satisfies Eq. (5.2), to one-loop order.

By the same reasoning, the difference in Eq. (5.4) is not well-behaved but divergent in the UV, and therefore requires regularization and renormalization. The renormalization conditions are given by the matching conditions themselves and thus indirectly refer to the renormalization conditions of the UV model. All free parameters of the EFT are fixed, order by order, in terms of the original parameters of the UV model. Nevertheless, a practical scheme such as dimensional regularization with minimal subtraction may

introduce an intermediate renormalization which depends on an arbitrary scale μ_R. The implications of this additional mass scale will be discussed in detail below.

In analogy with the tree-level matching procedure, in order to manifestly preserve the symmetries of the theory one should consistently work with covariant derivatives in the one-loop matching calculation, as discussed in the following subsection. However, due to the presence of UV divergences in the matching conditions the Slavnov-Taylor identity need not be compatible with a local Taylor expansion of the one-loop vertex functions, and the separation of the UV effective action into a gauge-invariant low-energy effective action and a remainder like in Eq. (5.1) may fail [217, 229, 230]. In the current chapter, we assume that such an obstruction does not critically affect our argument.

5.2.2 One-loop matching: implementation

Instead of constructing the difference in Eq. (5.4) in terms of Feynman graphs explicitly, the subtraction may be accounted for in the integrand by employing the method of regions [231–233]. The matching correction (Eqs. (5.4) and (5.5)) is replaced by

$$S_{\text{EFT}}^{1\ell}[\psi] = ic_s \operatorname{Tr} \log \left(-\frac{\delta^2 S_{\text{UV}}[\Psi, \psi]}{\delta(\Psi, \psi)^2} \right) \bigg|_{\text{hard}}. \tag{5.6}$$

The label 'hard' has to be understood in the following way: the functional trace is computed in momentum space. Two different regions are of interest in the matching, the hard and the soft region. If q denotes the typical size of a loop momentum, the hard region is defined by $q \sim M \gg m$, whereas the soft region is defined by $q \sim m \ll M$. Here m stands for the typical mass scale of the light sector. As discussed above, only the hard region is relevant while in the soft region the matching integral is well behaved. It has been shown that the tree-level induced EFT contribution to the matching cancels the soft region contributions from the UV-theory in the difference in Eq. (5.4) [149, 234]. Therefore, the integrands of the loop integrals in Eq. (5.6) are expanded only in the hard region. The evaluation of the functional trace then reduces to computing integrals of the form

$$\int \frac{\mathrm{d}^d q}{(2\pi)^d} \frac{q^{\mu_1} \dots q^{\mu_{2n_c}}}{(q^2 - M_{i_1}^2)^{n_1} \dots (q^2 - M_{i_m}^2)^{n_m} (q^2)^{n_0}}. \tag{5.7}$$

Here, all masses $M_{i_1}, \dots, M_{i_m}$ are of the order of M. This implies that the dependence of Eq. (5.6) on any external momentum or mass $|p|$ is analytic, and no logarithms of the form $\log(m/|p|)$ or $\log(|p|/M)$ can appear. The only logarithm possible is $\log(M/\mu_R)$, and to avoid large logarithms in the relation between EFT and UV parameters we need to choose $\mu_R \sim M$.

Apart from the prescription 'hard', the second derivatives of the UV-action evaluated at the background field configurations appear in the matching. To derive a universal result these derivatives are split into a part that contains the gauge-kinetic term of the field and its mass term, generating the propagator of the field, and a pure interaction contribution that appears in the final result. For the field ψ this latter piece is given by

$$X_{\psi\psi} = -\frac{\delta^2 S_{\text{UV,int.}}}{\delta\psi^2}, \tag{5.8}$$

where only the interaction part of the action excluding the interactions with gauge bosons through the covariant derivative appears. The interactions with the gauge bosons are included in the propagator part of the functional derivative, which allows for an evaluation in which only gauge covariant objects appear at every step and the final result is manifestly gauge invariant. The price to be paid for this manifest gauge covariance is that every occurrence of a covariant derivative has to be shifted by a loop momentum in the evaluation of the functional trace in Eq. (5.6). We therefore have to parameterize Eq. (5.8) as

$$X_{\psi\psi} = U_{\psi\psi} + iD_\mu Z_{\psi\psi}^\mu + iZ_{\psi\psi}^{\dagger\mu}D_\mu + \dots, \tag{5.9}$$

where D_μ is the covariant derivative of the UV-model. The quantities $U_{\psi\psi}, Z_{\psi\psi}^\mu$ and $Z_{\psi\psi}^{\dagger\mu}$ only depend on covariant derivatives through commutators whereas the explicit covariant derivatives appearing in Eq. (5.9) are so-called open covariant derivatives that act on everything to their right. The ellipsis denotes terms with further open covariant derivatives. Importantly, contributions with one open covariant derivative arise at dimension six whenever there is a scalar field charged under the gauge group and therefore they contribute to the matching through the presence of the Higgs field. Consequently, for our matching computations we use an extension of the results of Ref. [151], adding gauge bosons and the heavy resonance of our model. Since the gauge boson fluctuations appear in loops they have to be gauge fixed. This gauge fixing does not disturb the manifest gauge invariance at the level of the background fields and the gauge-fixing parameter can be chosen at convenience. Choosing Feynman gauge allows for easy incorporation of these operators into the results of Ref. [151], since we can treat gauge bosons like scalar fields with an extra index. Care has to be taken to account for the overall sign in the propagator. For the resonance this choice is not available since it does not have a gauge-fixing term and some operators with up to two open covariant derivatives have to be computed for the matching.

5.2.3 Heavy vector triplet (HVT)

The UV model we study in this chapter is a gauge-triplet extension of the Standard Model [200, 206–209]. In the unbroken electroweak phase, the Lagrangian reads

$$\begin{aligned}
\mathcal{L} = \mathcal{L}_{\text{SM}} &- \frac{1}{4}\widetilde{V}^{\mu\nu A}\widetilde{V}_{\mu\nu}^A - \frac{\tilde{g}_M}{2}\,\widetilde{V}^{\mu\nu A}\widetilde{W}_{\mu\nu}^A + \frac{\tilde{m}_V^2}{2}\widetilde{V}^{\mu A}\widetilde{V}_\mu^A \\
&+ \sum_f \tilde{g}_f\,\widetilde{V}^{\mu A}J_\mu^{fA} + \tilde{g}_H\,\widetilde{V}^{\mu A}J_\mu^{HA} + \frac{\tilde{g}_{VH}}{2}\,|\phi|^2\widetilde{V}^{\mu A}\widetilde{V}_\mu^A\,,
\end{aligned} \tag{5.10}$$

where $\widetilde{V}_\mu^A$ is a new, massive vector field transforming as a triplet of $SU(2)_L$, $\widetilde{W}_\mu^A$ are the SM weak gauge bosons, and ϕ is the SM Higgs doublet. The kinetic term of the vector field includes a covariant derivative,

$$\widetilde{V}_{\mu\nu}^A = \widetilde{D}_\mu\widetilde{V}_\nu^A - \widetilde{D}_\nu\widetilde{V}_\mu^A \quad \text{with} \quad \widetilde{D}_\mu\widetilde{V}_\nu^A = \partial_\mu\widetilde{V}_\nu^A - g_2 f^{ABC}\widetilde{W}_\mu^B\widetilde{V}_\nu^C\,. \tag{5.11}$$

where A, B, C are $SU(2)_L$ indices and the covariant derivative carries a tilde to indicate that it contains the fields $\widetilde{W}_\mu^A$. The currents coupling the heavy vector to the SM-fields are given by

$$J_\mu^{lA} = \bar{l}_i\gamma_\mu t^A l_j\,\delta^{ij}\,, \qquad J_\mu^{qA} = \bar{q}_i\gamma_\mu t^A q_j\,\delta^{ij}\,, \qquad J_\mu^{HA} = \phi^\dagger i\overleftrightarrow{D}_\mu^A\phi\,, \tag{5.12}$$

with l, q being the SM lepton and quark doublets, $t^A = \sigma^A/2$ the $SU(2)$ generators and σ^A the Pauli matrices. i, j are flavor indices and the Lagrangian is defined in a flavor-symmetric limit. In the Higgs current, $(\phi^\dagger i \overleftrightarrow{D}^A_\mu \phi) = i\phi^\dagger t^A (D_\mu\phi) - i(D_\mu\phi^\dagger)t^A\phi$. As pointed out in [234], the theory can not be quantized in a self-consistent way for $\tilde{g}_{VH} < 0$.

The gauge mixing described by the triplet model is familiar from the general case of extra-$U(1)$ bosons [235]. A special feature is the explicit $\widetilde{V}$-mass term, which would have to be generated by some kind of symmetry breaking and likely involve additional fields; we ignore these additional fields, for instance in their effect on $\tilde{g}_M$. The Higgs doublet ϕ is yet to develop a vacuum expectation value (VEV), which means we are working in the unbroken electroweak phase. Underlying this choice is the assumption that a SMEFT expansion for the EFT exists. This is the case unless there are additional sources of electroweak symmetry breaking, or a heavy particle obtains all of its mass from the Higgs VEV [236]. Even in the weakly coupled UV-completion of the triplet model there are no additional sources of electroweak symmetry breaking, because the additional scalar breaks $SU(2) \times SU(2)$ to $SU(2)_L$ and leaves the electroweak symmetry completely intact.

To remove the kinetic mixing, we can re-define the SM-gauge field as [207, 208]

$$W^{\mu\nu A} = \widetilde{W}^{\mu\nu A} + \tilde{g}_M \widetilde{V}^{\mu\nu A} = \partial^\mu(\widetilde{W}^{\nu A} + \tilde{g}_M \widetilde{V}^{\nu A}) - \partial^\nu(\widetilde{W}^{\mu A} + \tilde{g}_M \widetilde{V}^{\mu A}) + \cdots \quad (5.13)$$

For the triplet field we only allow for a re-scaling, $\widetilde{V}^{\mu A} = \alpha V^{\mu A}$, so that the triplet mass does not get transferred into the SM-gauge sector. The triplet mass also fixes the phase of the real vector field $\widetilde{V}^A_\mu$, such that α has to be real. Requiring a canonical normalization of the new kinetic term $V^{\mu\nu A}V^A_{\mu\nu}$ we find $\alpha^2 = 1/(1 - \tilde{g}^2_M)$. This relation requires $\tilde{g}_M \neq \pm 1$, to ensure a valid model with a propagating heavy vector. Furthermore, as we will see in Sec. 5.3, we need to require $|\tilde{g}_M| < 1$ for the squared pole mass of the resonance to be positive. The final form of the gauge field re-definition in Eq. (5.13) becomes

$$\widetilde{W}^{\mu A} = W^{\mu A} - \frac{\tilde{g}_M}{\sqrt{1 - \tilde{g}^2_M}} V^{\mu A} \qquad \text{and} \qquad \widetilde{V}^{\mu A} = \frac{1}{\sqrt{1 - \tilde{g}^2_M}} V^{\mu A} \,, \qquad (5.14)$$

and brings the Lagrangian into the form

$$\begin{aligned}
\mathcal{L} = \mathcal{L}_{\text{SM}} &- \frac{1}{4}V^{\mu\nu A}V^A_{\mu\nu} + \frac{m^2_V}{2}V^{\mu A}V^A_\mu \\
&+ \sum_f g_f \, V^{\mu A}J^{fA}_\mu + g_H V^{\mu A}J^{HA}_\mu + \frac{g_{VH}}{2}\,|H|^2 V^{\mu A}V^A_\mu \\
&+ \frac{g_{3V}}{2}f^{ABC}\,V^{\mu A}V^{\nu B}V^C_{\mu\nu} - \frac{g_{2VW}}{2}f^{ABC}\,V^{\mu B}V^{\nu C}W^A_{\mu\nu} \,, \qquad (5.15)
\end{aligned}$$

which has the same structure as Eq. (5.10), but additional triple and quartic gauge couplings between the weak and triplet sectors. The Lagrangian parameters are related through

$$m^2_V = \frac{\tilde{m}^2_V}{1 - \tilde{g}^2_M}\,, \qquad\qquad g_H = \frac{\tilde{g}_H + g_2\tilde{g}_M}{\sqrt{1 - \tilde{g}^2_M}}\,, \qquad\qquad g_f = \frac{\tilde{g}_f + g_2\tilde{g}_M}{\sqrt{1 - \tilde{g}^2_M}}\,,$$

$$g_{VH} = \frac{2\tilde{g}_{VH} + g^2_2\tilde{g}^2_M + 2g_2\tilde{g}_H\tilde{g}_M}{2(1 - \tilde{g}^2_M)}\,, \qquad g_{3V} = -\frac{2g_2\tilde{g}_M}{(1 - \tilde{g}^2_M)^{1/2}}\,, \qquad g_{2VW} = \frac{g_2\tilde{g}^2_M}{1 - \tilde{g}^2_M}\,,$$
$$(5.16)$$

where g_2 denotes the $SU(2)_L$ gauge coupling. The heavy vector triplet couples to the weak gauge bosons not only via the $g-$couplings in Eq. (5.15), but also through the non-abelian component of the covariant derivative Eq. (5.11), that leads to interaction terms of the form $(\partial V)VW$ and $VVWW$. These interactions are weighted by the weak gauge coupling, and therefore are present even if $g_i\,(\tilde{g}_i) \equiv 0$.

Matching expressions at tree-level

Matching the heavy vector triplet model defined in Eq. (5.10) at tree level onto the Warsaw basis, we obtain

$$C_{\phi\Box} = -\frac{3}{8}\frac{(\tilde{g}_H + g_2\tilde{g}_M)^2}{\tilde{m}_V^2}$$

$$C_{\phi l,ij}^{(3)} = \bar{C}_{\phi l}^{(3)}\delta_{ij} = -\frac{1}{4}\frac{(\tilde{g}_l + g_2\tilde{g}_M)(\tilde{g}_H + g_2\tilde{g}_M)}{\tilde{m}_V^2}\delta_{ij}$$

$$C_{\phi Q,ij}^{(3)} = \bar{C}_{\phi q}^{(3)}\delta_{ij} = -\frac{1}{4}\frac{(\tilde{g}_q + g_2\tilde{g}_M)(\tilde{g}_H + g_2\tilde{g}_M)}{\tilde{m}_V^2}\delta_{ij}$$

$$C_{ll,ijkl} = \bar{C}_{ll}\delta_{ij}\delta_{kl} + \bar{C}_{ll}'\delta_{il}\delta_{kj} = \frac{1}{8}\frac{(\tilde{g}_l + g_2\tilde{g}_M)^2}{\tilde{m}_V^2}(\delta_{ij}\delta_{kl} - 2\delta_{il}\delta_{kj})$$

$$C_{f\phi,ij} = -\frac{(Y_f)_{ij}}{4}\frac{(\tilde{g}_H + g_2\tilde{g}_M)^2}{\tilde{m}_V^2} \qquad (f = e, u, d). \quad (5.17)$$

These results were also derived e.g. in Refs. [200, 206, 209, 237]. The full expressions for the one-loop matching were derived in [2] for the first time and are provided at Ref. [158].

5.2.4 SFitter setup

The SFITTER framework [120] has been long employed for global analyses of LHC measurements in the context of Higgs couplings and EFTs [36–38, 50, 128, 238], including a comprehensive study of an analysis in terms of Higgs couplings and its UV-completion [124]. The approach is unique in that it allows a comprehensive treatment of uncertainties: SFITTER uses a likelihood set up that includes a broad set of statistical, systematic, and theory uncertainties. Statistical and most systematic ones are described by a Poisson- or Gauss-shaped likelihood. Theoretical uncertainties lack a frequentist interpretation, and are described by flat likelihoods in SFITTER, corresponding to a range of equally likely theory predictions. An important difference between employing a flat likelihood compared to a Gaussian one is that the uncorrelated profile likelihood adds the uncertainties from the flat distributions linearly, while Gaussian error bars are added in quadrature. The profile likelihood combination of a flat and a Gaussian uncertainty gives the well-known RFit prescription [132]. Correlations among certain classes of systematic uncertainties are also included.

From the technical point of view, the new aspect of the SFITTER analysis presented in this chapter is the translation of the SMEFT likelihood into the parameter space of the UV model. In the fit, all observables are parameterized in the SMEFT using the operator set provided in Tab. 2.4, that is based on the Hagiwara, Ishihara, Szalapski, and Zeppenfeld (HISZ) basis [99]. All SMEFT predictions are at LO in quantum chromodynamics (QCD) and scaled by the same corrections as the SM-rates used for the actual experimental analysis. Terms obtained from squaring amplitudes with one operator insertion, that

are quadratic in the WCs, are retained. The WCs are then expressed in terms of $\tilde{g}_i$ parameters of the UV model, Eq. (5.10), using the one-loop matching expressions onto the Warsaw basis provided in Ref. [158] and the Warsaw-to-HISZ basis translation in Sec. 3.4.2. In this way, the likelihood can be directly sampled in the parameter space of the UV model.

In addition, we employ a new likelihood sampling method [1] compared to previous SFITTER analyses, that ensures a much more efficient sampling close to the SM point, where all WCs vanish. By contrast, the previous sampling method was optimized for the detection of potential secondary maxima in the likelihood, by giving higher weight to the edges of the parameter space.

Dataset

The SMEFT analysis presented in this work builds directly on the dataset employed in Ref. [36], which includes electroweak precision observables (EWPO) at LEP (14 measurements), Higgs measurements (275) and di-boson measurements at the LHC (43). The latter contain results from both Run 1 and Run 2 [37]. In addition, we include differential measurements from three resonance searches by ATLAS, that reach up to invariant masses in the multi-TeV range and that we re-interpret within the SMEFT framework. One of these [239] was already included in the analysis of Ref. [36]. The other two [168, 197] are more recent and have been added specifically for this work. These measurements are not usually included in the SMEFT analyses and are not covered by the simplified template cross section framework [167]. Nevertheless, it can be instructive to explore their sensitivity, particularly to operators that induce momentum-enhanced corrections. Moreover, all the resonance searches considered here target heavy vector triplets decaying into WH or WW as a potential signal. Therefore they allow to compare directly the constraining power of the SMEFT analysis to that of the direct search.

Theory uncertainties

In view of the upcoming LHC runs and their rapidly growing data sets, the treatment of theory uncertainties in global analyses is becoming critical. In our analysis, we include theory uncertainties associated to parton distribution functions, to missing higher orders in the SM or SMEFT predictions, and to the matching scale to the EFT. The latter will be discussed in more detail in Sec. 5.3.2.

For the time being, we do not include uncertainties associated to missing SMEFT operators due to the truncation of the SMEFT Lagrangian [240] or to symmetry assumptions, such as CP-conservation. Nevertheless, the impact of missing higher orders in the EFT expansion becomes obviously manifest in the comparison between constraints extracted from the SMEFT analysis and from direct searches.

Concerning higher orders in the loop expansion, Higgs analyses in SFITTER currently adopt the most accurate SM predictions available, which are implemented so as to match the state-of-the art predictions reported in the experimental analyses. The corresponding K-factors are then applied onto the tree-level SMEFT predictions as well, which is tantamount to assuming that QCD corrections scale evenly for all SMEFT operators and in the same way as in the SM. Although this assumption is, strictly speaking, not correct [241], for the rate measurements considered here we do not expect large variations
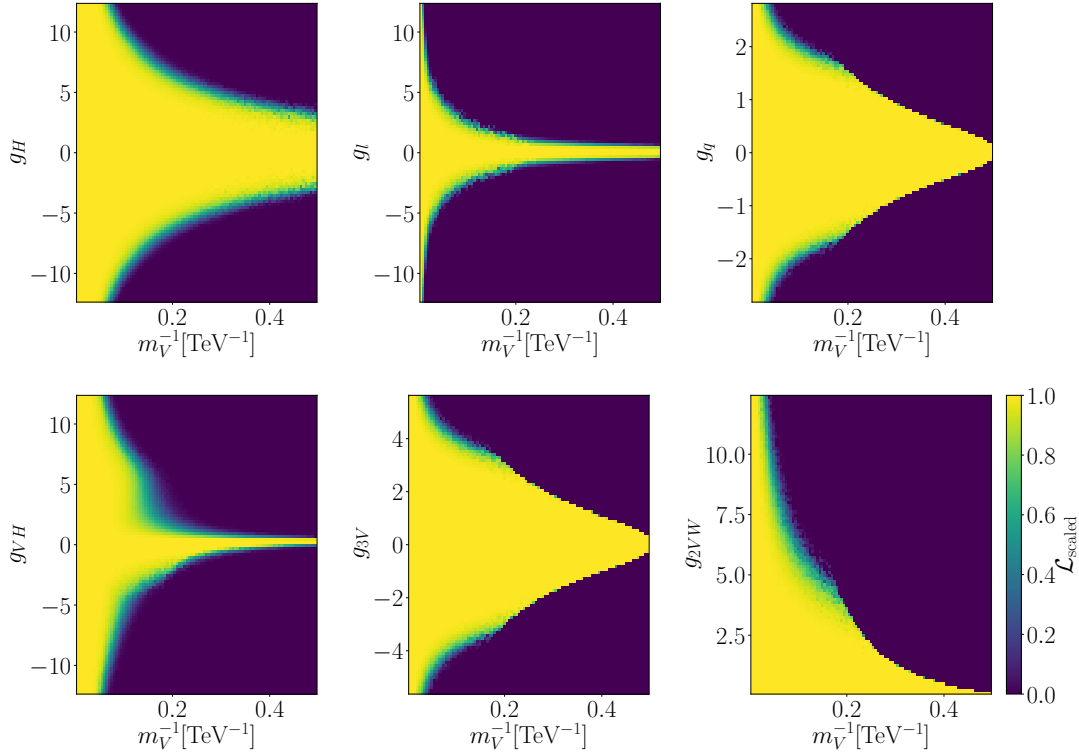
Figure 5.1: Decoupling pattern for the vector triplet model. Global fit with all measurements at their SM values and to the 4 free parameters $\tilde{m}_V, \tilde{g}_M, \tilde{g}_H, \tilde{g}_l$, and subsequently projected onto the 7 parameters of the unmixed Lagrangian Eq. (5.15).

in the K-factors between different operators. For some kinematic distributions these effects can be larger. We therefore assign conservative theory uncertainties in order to reduce the numerical impact of these effects. A proper SMEFT simulation of Higgs and di-boson production up to NLO in QCD is postponed to a future work.

5.3 Toy fits and matching uncertainty

In this section we discuss two aspects of the vector triplet model and of its matching onto the SMEFT, that are preliminary to a correct SMEFT global analysis. The first is the decoupling limit of the model, and the second is the numerical impact of varying the scale at which the one-loop matching is performed. Both issues are analyzed via simplified toy fits.

5.3.1 Decoupling

The decoupling limit of the vector triplet model considered in this work is most easily identified starting from the Lagrangian of Eq. (5.15), where, as long as the EW symmetry is unbroken, the heavy triplet and the SM gauge bosons do not mix. In this case, it is easy to see that the BSM states decouple for large values of the physical mass, $m_V \to \infty$. This is directly reflected in the matching formulas, which give $\lim_{m_V \to \infty} C_i \equiv 0$ for all the
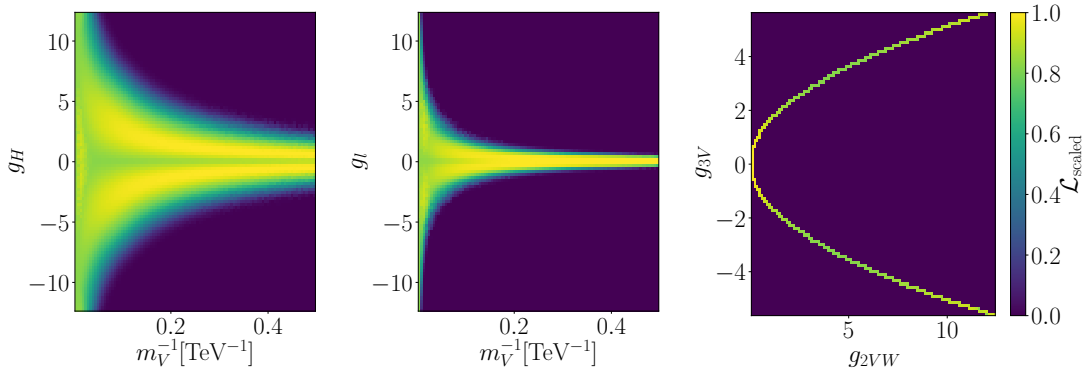
Figure 5.2: Results of the same global analysis as in Fig. 5.1, but with measurements set to their actual values.

dimension-6 WCs. At the level of a global fit, the decoupling limit can be visualized by setting the central values of all the measurements included to match the corresponding SM predictions. Figure 5.1 shows the results obtained in this way from SFITTER: the likelihood is first computed as a function of 4 free parameters in the Lagrangian of Eq. (5.10)

$$\{\tilde{m}_V, \tilde{g}_M, \tilde{g}_H, \tilde{g}_l\}\,, \tag{5.18}$$

setting other parameters $\tilde{g}_q$, $\tilde{g}_{VH}$ to zero. We then project them onto the 7 parameters for the rotated Lagrangian of Eq. (5.15),

$$\{m_V, g_H, g_l, g_q, g_{VH}, g_{3V}, g_{2VW}\}\,. \tag{5.19}$$

At this stage, we fix the matching scale to $Q = m_V = 4\,\text{TeV}$. For each of the couplings we see that, as expected, the range of allowed values increases as $m_V^{-1} \to 0$. It is worth noting that the rate at which this happens varies between the g-parameters. This is due to the fact that the matching expressions do not scale homogeneously with g_i^2/m_V^2, but generally have a more complex polynomial structure. The degeneracy between g_i and $1/m_V$ in these expressions is also broken by the $V - W$ interactions proportional to the weak gauge coupling. The homogeneity of the yellow regions indicates that there the likelihood is flat and no point is preferred. Setting all measurements to their actual measured values, which generally depart from the SM predictions, has the effect of introducing a substructure in the likelihood, thereby identifying a more restricted preferred region. This is shown, for a subset of panels, in Fig. 5.2. Here, for instance, the best fit point moves to finite m_V and prefers non-vanishing values of g_H. Note that, to good approximation, the entire region highlighted in green is allowed at 68%CL. The yellow points simply identify a best-fit region and should not be interpreted as statistically significant. Finally, the reduced number of parameters in the Lagrangian Eq. (5.10) as compared to the setup without kinetic mixing induces strong correlations through $\tilde{g}_M$, as illustrated in the $g_{2VW} - g_{3V}$ plane of Fig. 5.2.

As the matching procedure highlighted in Sec. 5.2.1 requires a separation between light and heavy degrees of freedom, defining the decoupling limit in the notation of Eq. (5.10) requires some more care, due to the explicit kinetic mixing between the heavy triplet and the SM gauge fields.

From Eq. (5.16), we see that $m_V \to \infty$ can be achieved for $\tilde{m}_V \to \infty$ or for $|\tilde{g}_M| \to 1$.

However, the condition $|\tilde{g}_M| = 1$ does not lead to a well-defined decoupling condition, because in this limit $\tilde{V}_\mu^A$ become auxiliary fields, i.e. the theory loses three dynamical degrees of freedom. This is not sufficient for a proper decoupling in the EFT sense because even as an auxiliary field $\tilde{V}_\mu^A$ still induces mass-suppressed vertices that enter correlation functions and we enter a strongly interacting regime where our perturbative approach fails.

To see the impact of $\tilde{g}_M$ we resum insertions of gauge mixing into the $\widetilde{W}_\mu^A$ and $\widetilde{V}_\mu^A$ propagators. The corrected propagators of these fields become

$$\hat{D}_{\mu\nu}^{\widetilde{V}} = -\frac{i}{p^2 - \tilde{m}_V^2 - \tilde{g}_M^2 p^2}\left(g_{\mu\nu} - (1 - \tilde{g}_M^2)\frac{p_\mu p_\nu}{\tilde{m}_V^2}\right)$$

$$\hat{D}_{\mu\nu}^{\widetilde{W}} = -\frac{i}{p^2}\left(g_{\mu\nu} - (1 - \xi)\frac{p_\mu p_\nu}{p^2}\right) - \frac{i\tilde{g}_M^2}{p^2 - \tilde{m}_V^2 - \tilde{g}_M^2 p^2}\left(g_{\mu\nu} - \frac{p_\mu p_\nu}{p^2}\right) . \tag{5.20}$$

It is easy to see that for $|\tilde{g}_M| = 1$ the resummed $\tilde{V}_\mu^A$ propagator loses its momentum dependence, which is indicative of the field becoming auxiliary. For $|\tilde{g}_M| > 1$, $\tilde{V}_\mu^A$ becomes tachyonic while, for $|\tilde{g}_M| < 1$, $\tilde{V}_\mu^A$ is a dynamical degree of freedom. In this case its propagator has a physical pole at $p^2 = m_V^2$ as defined in Eq. (5.16), and it can be expanded in $p^2/m_V^2 \ll 1$. The resummed $\widetilde{W}_\mu^A$ propagator includes a term with a pole at $p^2 = m_V^2$, contaminating $\widetilde{W}_\mu^A$ with a contribution from $\tilde{V}_\mu^A$. Therefore this field can not be directly identified with the SM weak bosons. However, in the tree-level matching procedure, once the 1LPI effective action is expanded in p^2/m_V^2, the component associated with the $\tilde{V}_\mu^A$ pole is shifted from the propagators to the interaction terms, which are unambiguously fixed at this order by the matching condition of Eq. (5.2). At one loop, the fact that the EFT is the low-energy limit of the UV model is manifest in the fact that only the 'hard' region of the momentum integral contributes to the functional trace in the matching formula of Eq. (5.6). As a consequence, the first term of the $\widetilde{W}_\mu^A$ propagator cancels against the corresponding EFT contributions, while the second term genuinely contributes to the matching in the hard region. Equivalently, one can match in the shifted basis directly identifying W_μ^A in the UV model with the corresponding weak bosons in the SMEFT.

In the top (bottom) panels of Fig. 5.3 we again show the results of a global analysis where all measurements are set to their SM prediction (to their actual values), this time projected onto a subset of the $\tilde{g}$-parameters and onto the combination $\tilde{g}_M/\sqrt{1 - \tilde{g}_M^2}$ that drives most $\tilde{g} - g$ relations, see Eq. (5.16). For reference, the right panels also show lines of constant m_V, such that the decoupling limit $m_V \to \infty$ flows orthogonally to the lines. Consistent with the results in the unmixed basis (Fig. 5.1), the expected likelihood is mostly flat in the entire preferred region, while the observed one exhibits a substructure that identifies a best-fit region where $\tilde{g}_H \neq 0$ and both m_V and $\tilde{m}_V$ are finite. The reason can be identified in a few EWPO measurements that exhibit small $(< 1\sigma)$ deviations from the SM expectation: $A_l(\text{SLD})$ and m_W.

For $|\tilde{g}_M| \to 1$ the theory becomes strongly interacting and some perturbative unitarity considerations are therefore pertinent. Requiring the couplings of the unmixed UV theory to remain perturbative, the most stringent constraints on $\tilde{g}_M$ stem from g_{2VW}

$$g_{2VW} \approx \frac{g_2 \tilde{g}_M^2}{1 - \tilde{g}_M^2} < 4\pi \qquad \Leftrightarrow \qquad |\tilde{g}_M| < 0.975 . \tag{5.21}$$
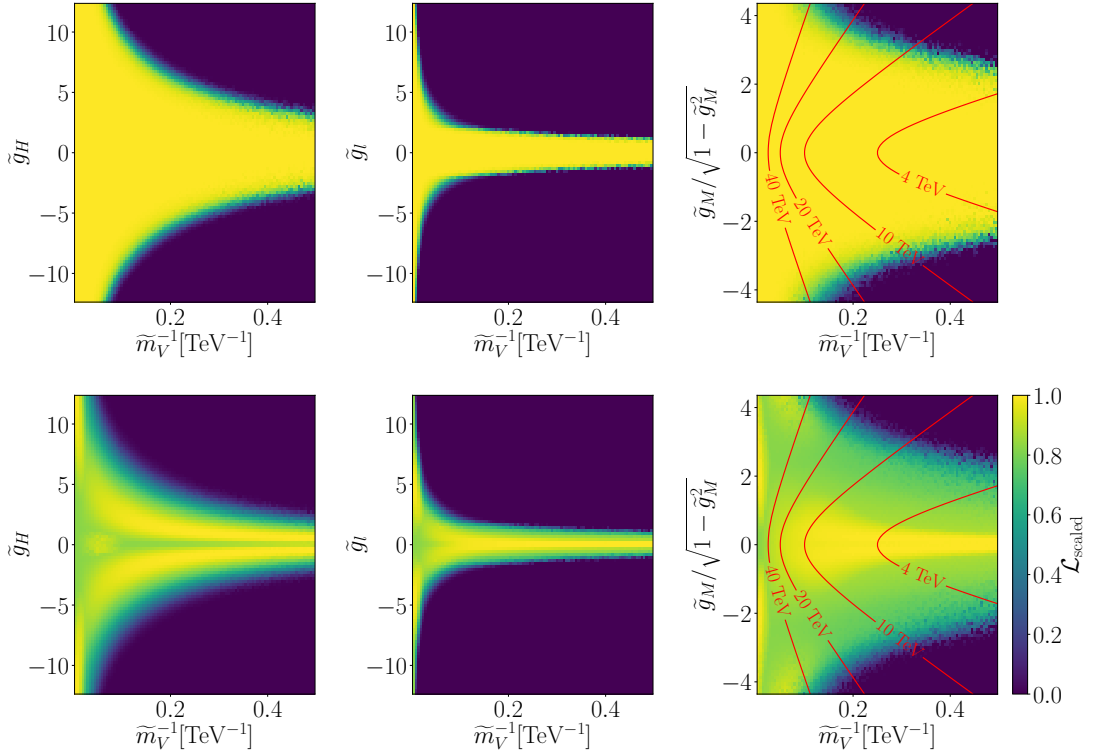
Figure 5.3: Results of the same global analyses as in Fig. 5.1 (upper) and 5.2 (lower), projected on $\tilde{m}_V, \tilde{g}_H, \tilde{g}_l$ and the combination $\tilde{g}_M/\sqrt{1 - \tilde{g}_M^2}$.

Therefore for all our fits we require $|\tilde{g}_M| < 0.975$.

5.3.2 Matching scale

In perturbative predictions of LHC observables, at least two unphysical scales are known to reflect a theory uncertainty, the factorization scale and the renormalization scale. Both arise from a separation of an observable into different regimes with different perturbative expansions, and the scale dependence would vanish if we would include all orders in all predictions. For a calculation at finite perturbative order we instead use the scale variation as one measure of a theory uncertainty and treat it as an unphysical nuisance parameter in theory predictions [38, 127].

One unphysical scale is the renormalization scale, which in the context of dimensional regularization appears as a free parameter. In more physical terms, the renormalization scale is the energy scale associated with those observables that we select for defining the numerical parameters of the theory, the renormalization conditions. Whenever scale choices are arbitrary, we often identify them with each other and a typical energy scale of the scattering process to avoid large logarithms. Clearly, this does not work if renormalization conditions involve widely distinct energy scales, such as in the relation of UV-model parameters to the low-energy observables of the SM.

The renormalization group equation apparently solves this problem. It relates observables at different scales, properly resumming logarithms and absorbing them into running parameters. However, it works only in the absence of mass thresholds. This strongly

suggests to match a UV model with a heavy mass M to a low-energy EFT even if the algebraic simplifications of the latter are not essential for a specific calculation.

In a one-loop matching calculation that uses dimensional regularization, the matching scale enters as an additional parameter. However, in contrast to the original renormalization scale this parameter is not entirely arbitrary. If we want to avoid large logarithms, its reasonable range is bounded from above and below. In line with the generic discussion of one-loop matching above, we illustrate this property in the following section. We consider examples of increasing complexity, starting from the QCD coupling, turning next to the SM extended by a scalar singlet and finally returning to the vector triplet model of Sec. 5.2.3.

Running strong coupling

We can illustrate the appearance of the matching scale using the simple example of the running strong coupling. It provides the key ingredients to understanding the EFT matching scale: the separation of low-energy and UV regimes and contributions beyond tree level. In general, the relation between the bare coupling and the renormalized coupling in the $\overline{\text{MS}}$ scheme is

$$\alpha_s^{\text{bare}} = \alpha_s(p^2) \left[1 - \alpha_s b_0 \left(\frac{1}{\bar{\epsilon}} + \log \frac{\mu_R^2}{p^2} \right) \right] \quad \text{with} \quad b_0^{(n_f)} = \frac{1}{4\pi} \left(\frac{11}{3} N_c - \frac{2}{3} n_f \right) . \tag{5.22}$$

Here, p^2 is the energy scale of the scattering, μ_R^2 is introduced by dimensional regularization, and $1/\bar{\epsilon} = 1/\epsilon - \gamma_E + \log 4\pi$. We identify our UV-regime as momenta above the top mass, with six propagating quark flavors, and the low-energy regime as described by five propagating quark flavors. The running of α_s in the two regimes is described by the beta function with five or six flavors, respectively. The UV-divergences in the low-energy and full UV-theories arise from five or six propagating flavors, so the renormalization prescription Eq. (5.22) is different in the two regimes.

The low-energy and UV-regimes are separated by a matching scale Q, which we choose to be of the order of the top mass to avoid large logarithms or inconsistent symmetry structures. Matching conditions guarantee that the two predictions for any observable are the same at least at this scale. Instead of looking at a full set of amplitudes or correlation functions, we limit ourselves to the quasi-observable α_s. Following Eq. (5.22), the definitions of $\alpha_s(p^2)$ in relation to the bare parameter are different, but they have to agree when evaluated at the matching scale. This defines a threshold correction

$$1 - \frac{\alpha_s b_0^{(6)}}{4\pi} \left(\frac{1}{\bar{\epsilon}} + \log \frac{\mu_R^2}{p^2} \right) \bigg|_{Q^2} = 1 - \frac{\alpha_s b_0^{(5)}}{4\pi} \left(\frac{1}{\bar{\epsilon}} + \log \frac{\mu_R^2}{p^2} \right) \bigg|_{Q^2} + \frac{\alpha_s}{6\pi} \log \frac{\mu_R^2}{Q^2} . \tag{5.23}$$

The relation of the threshold correction to loop effects is reflected in the logarithmic form $\log \mu_R^2/Q^2$. Together with the five-flavor $\overline{\text{MS}}$ counter term it defines α_s in the low-energy regime as

$$\alpha_s^{\text{bare}} = \alpha_s(p^2) \left[1 - \frac{\alpha_s b_0^{(5)}}{4\pi} \left(\frac{1}{\bar{\epsilon}} + \log \frac{\mu_R^2}{p^2} \right) + \frac{\alpha_s}{6\pi} \log \frac{\mu_R^2}{Q^2} \right] . \tag{5.24}$$

This definition includes three scales for a given scattering process, the physical scale p^2, the renormalization scale μ_R^2, and the matching scale Q^2. In simple problems, the renormalization scale and the physical scale can be identified to avoid potentially large logarithms. The matching scale is usually set to the mass of the decoupled particle, $Q = m_t^2$, leading to a threshold correction that is non-zero in general.

From our toy example we can immediately see the role of the threshold correction at the matching scale and the renormalization group running. If we start from the UV, all parameters of the theory evolve based on the full particle spectrum. In the low-energy theory part of the spectrum decouples also from the running, which can even break the underlying symmetries [242], and we will follow a completely different renormalization group flow. The matching corrections adjust for this effect. They move us to the same flow line in the EFT, independent of the choice of matching scale and with all the caveats of maintaining perturbative control, accounting for changes of the spectrum, changing symmetries, etc.

Singlet extension

When we interpret a SMEFT calculation for an LHC process as a low-energy approximation to a UV-prediction, we again break the phase space of the scattering process into two parts. We first illustrate SMEFT matching using the singlet-extended SM [243, 244],

$$\mathcal{L} \supset \frac{1}{2}\left(\partial_\mu S\right)\left(\partial^\mu S\right) - \frac{1}{2}M^2 S^2 - A|\phi|^2 S - \frac{\kappa}{2}|\phi|^2 S^2 - \frac{\mu}{3!}S^3 - \frac{\lambda_S}{4!}S^4 \ . \tag{5.25}$$

The singlet mass is given by $M_S^2 = M^2 + \mathcal{O}(v^2)$; we integrate it out under the condition $M_S \sim M \gg v$, ensuring a consistent expansion in v/M [236]. As a simplification, we also assume A to be of the order of M. The leading term in v/M is defined by $v = 0$ and can be obtained by matching in the unbroken phase. In the broken phase the Higgs VEV enters via the masses of the SM-particles which properly belong to the EFT Lagrangian, below the matching scale. Matching in the broken phase would allow us to include partial higher-order corrections in the EFT expansion [205]. Since the mass scales in question are not widely separated, it depends on the detailed numerics which setup yields a more reliable approximation. The SMEFT Lagrangian reads

$$\mathcal{L}_{\text{SMEFT}} = \mathcal{L}_{\text{SM}} + \sum_i f_i(p/\mu_R)\,\mathcal{O}_i \ , \tag{5.26}$$

where the WCs are scale dependent. Specifically, we want to define these coefficients such that the SMEFT reproduces all low-energy observables of the UV-theory up to $\mathcal{O}(v^3/M_S^3)$. As matching condition we use Eq. (5.1). In the functional approach we compute this once and for all using functional traces. To illustrate some features related to the matching scale, we compute some contributions to the WC $f_{\phi 2}$ of the operator $\mathcal{O}_{\phi 2} = \partial_\mu(\phi^\dagger\phi)\partial^\mu(\phi^\dagger\phi)/2$ diagrammatically. As discussed in Sec. 3.4.2, it is related to $Q_{\phi\square} = |\phi|^2\square|\phi|^2$ as $c_{\phi\square} \approx -f_{\phi 2}/2$, modulo fermionic operators. The operator contributes to the correlation function with two external fields ϕ and two external fields $\phi^\dagger$ and depends on p^2, so we fix it by requiring

$$\partial_{p^2}\Gamma_{\text{SMEFT}}(\phi^\dagger,\phi^\dagger,\phi,\phi)\Big|_{p^2=0} = \partial_{p^2}\Gamma_{\text{L,UV}}(\phi^\dagger,\phi^\dagger,\phi,\phi)\Big|_{p^2=0} \ , \tag{5.27}$$
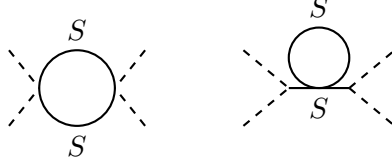
Figure 5.4: Feynman diagrams contributing to $f_{\phi 2}^{(1)}$. Left: Diagram yielding a κ^2-contribution. Right: Diagram yielding a $A^2 \lambda_S / M^2$-contribution. The dashed line corresponds to the Higgs field, whereas the solid line corresponds to the singlet.

order by order in the coupling. With some abuse of notation we also denote specific correlation functions by Γ, arguments indicating the external fields. Since both sides of the equation involve running parameters, the matching has to be imposed at a given scale,

$$\partial_{p^2} \left(\text{⊗} + \text{SM} \right) = \partial_{p^2} \left(\text{—}_S\text{—} + t\text{-channel} + \text{SM} \right) \text{ at } p^2 = 0 \quad .$$

The SM-contributions contain the same diagrams on both sides, with appropriately adjusted parameters through the matching conditions, so their contributions cancel. Only diagrams with at least one heavy propagator actually contribute to the matching, so Eq. (5.27) becomes

$$\partial_{p^2} \left(8p^2 f_{\phi 2}^{(0)} \right) \bigg|_{p^2=0} = \partial_{p^2} \frac{2A^2}{4p^2 - M^2} \bigg|_{p^2=0} \qquad \Rightarrow \qquad f_{\phi 2}^{(0)} = \frac{A^2}{M^4} . \tag{5.28}$$

At tree level, the scale dependence only appears implicitly for A and for $f_{\phi 2}^{(0)}$.

Next, we compute the κ^2-contribution to $f_{\phi 2}^{(1)}$ at one loop. This contribution is induced by the diagram on the left in Fig. 5.4, where the external particles are as specified in Eq. (5.27). We again set all external scales to p^2 and find for the diagram

$$\kappa^2 \mu_R^{4-d} \int \frac{d^d q}{(2\pi)^d} \frac{1}{((2p+q)^2 - M^2)(q^2 - M^2)} = \kappa^2 \frac{i}{16\pi^2} B_0(4p^2, M, M)$$

$$\text{with} \quad B_0(4p^2, M, M) = \frac{1}{\epsilon} - \log \frac{M^2}{\mu_R^2} + \frac{2p^2}{3M^2} + \mathcal{O}\left(\frac{p^4}{M^4} \right) . \tag{5.29}$$

In the full expression the renormalization scale appears, but taking the derivative in the matching condition for this contribution to $f_{\phi 2}$ removes it,

$$\partial_{p^2} B_0(4p^2, M, M) \bigg|_{p^2=0} = \frac{2}{3M^2} \qquad \Rightarrow \qquad f_{\phi 2}^{(1)} \supset \frac{1}{16\pi^2} \frac{\kappa^2}{12M^2} . \tag{5.30}$$

Just as at tree level, the matching scale does not appear explicitly.

Finally, we compute the $A^2 \lambda_S / M^2$-contribution to $f_{\phi 2}^{(1)}$ to illustrate the appearance of matching scale logarithms. This contribution arises from the diagram on the right in Fig. 5.4. The diagram is not 1PI, but is 1LPI and therefore has to be included in the
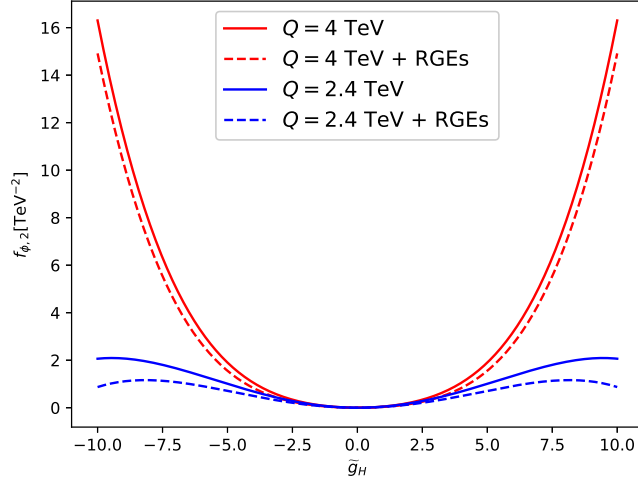
Figure 5.5: WC $f_{\phi 2}$ as a function of $\tilde{g}_H$ at different values of the matching scale Q for fixed $m_V = 4$ TeV and all other UV couplings set to zero. The dashed lines include approximate renormalization group (RG) running.

matching. With all external scales again set to p^2 this diagram gives

$$-\frac{\lambda_S A^2}{(4p^2 - M^2)^2}\mu_R^{4-d} \int \frac{\mathrm{d}^d q}{(2\pi)^d}\frac{1}{q^2 - M^2} = -\frac{\lambda_S A^2}{16\pi^2}\frac{M^2}{(4p^2 - M^2)^2}\left(\frac{1}{\epsilon} + 1 - \log\frac{M^2}{\mu_R^2}\right).$$
(5.31)

Taking the derivative with respect to p^2 and evaluating it at $p^2 = 0$ we find the one-loop matching condition

$$f_{\phi 2}^{(1)} \supset -\frac{1}{16\pi^2}\frac{\lambda_S A^2}{M^4}\left(-1 + \log\frac{M^2}{Q^2}\right),$$
(5.32)

where the WC explicitly depends on the matching scale. This scale dependence is expected since the corresponding correlation function is divergent. As mentioned before, in models with one new mass scale, we can of course avoid these logarithms by identifying $Q = M$.

Heavy vector triplet (HVT)

Moving to the triplet model defined by the Lagrangian of Eq. (5.10), we will not attempt to show analytic results and instead illustrate the matching scale dependence for one finite coupling $\tilde{g}_H$ and a mass term $\tilde{m}_V$ numerically. In this simplified setup, $m_V = \tilde{m}_V$. Among the various WCs, it is instructive to consider $f_{\phi 2}$, as its dependence on the matching scale exhibits interesting features. Including both tree and loop contributions, the matching expression has the form

$$\frac{f_{\phi,2}}{\Lambda^2} \simeq \frac{1}{m_V^2}\left[g_2^4\left(c_0 + c_1 \log\frac{m_V}{Q}\right) + \tilde{g}_H^2\left(c_2 + c_3 \log\frac{m_V}{Q}\right) + \tilde{g}_H^4\left(c_4 + c_5 \log\frac{m_V}{Q}\right)\right],$$
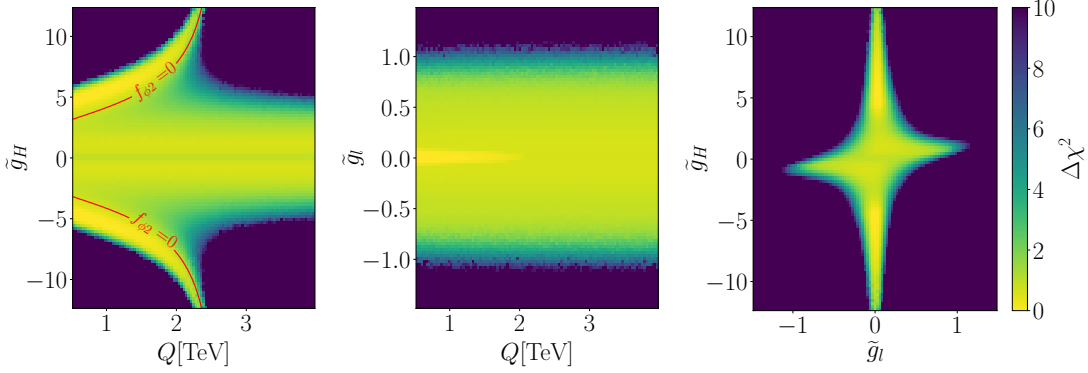(5.33)

Figure 5.6: The impact of the variation of the matching scale Q at a mass of $m_V = 4\,\text{TeV}$ for a reduced model with free $\tilde{g}_M, \tilde{g}_H, \tilde{g}_l$, expressed in the unmixed Lagrangian Eq. (5.15) with actual measurements.

where $c_0 = c_1/2$ emerges from one-loop diagrams inducing the operator structure $(D_\mu W^{\mu\nu})^2$, which maps to $\mathcal{O}_{\phi 2}$ via the equations of motion. Of the additional constants, the $\tilde{g}_H^2$-coefficient is dominated by the tree-level contribution to c_2, while the $\tilde{g}_H^4$-coefficient is completely determined by the one-loop matching. Numerically, we find

$$c_0 = \frac{c_1}{2} = \frac{3}{128\pi^2} = 0.0024\,,$$

$$c_2 = 0.75\,, \qquad c_3 = 0.0069\,, \qquad c_4 = 0.019\,, \qquad c_5 = -0.045\,. \qquad (5.34)$$

In Fig. 5.5 we show the numerical dependence of $f_{\phi,2}$ on $\tilde{g}_H$ for different choices of Q. For $Q = m_V = 4$ TeV the WC has a simple power dependence on $\tilde{g}_H$ driven by c_4. For $Q \approx 0.66\, m_V = 2.6\,\text{TeV}$ the $\tilde{g}_H^4$-term cancels exactly. For Q below this threshold, the coefficient in front of $\tilde{g}_H^4$ becomes negative, which flips the sign of $f_{\phi 2}$ at $\tilde{g}_H \gg 1$ and allows a solution of $f_{\phi 2} = 0$ for $\tilde{g}_H \neq 0$. For $Q \lesssim 2.4\,\text{TeV}$ the solution is within the range $|\tilde{g}_H| < 4\pi$ and leads to visible effects in our global analysis.

Figure 5.6 shows the results of the same global analysis as in Sec. 5.3.1, where now we fix $m_V = 4\,\text{TeV}$. The free parameters are

$$\{\tilde{g}_H, \tilde{g}_l, \tilde{g}_M, Q\}\,, \qquad (5.35)$$

where the matching scale is varied in the range $Q = 500\,\text{GeV} \dots 4\,\text{TeV}$. The left panel shows a central allowed region for $|\tilde{g}_H| \lesssim 4$ that is independent of Q. In addition, a beautiful *fleur-de-lis shape* arises in $\tilde{g}_H$ vs Q for $Q < 2.4$ TeV. It roughly follows the curves along which $f_{\phi 2} = 0$ marked in red. The WCs f_t, f_b, f_τ have a similar behavior and vanish approximately in the same region, because they are induced by the same or similar loop contributions. As these are the operators that dominate the constraint on $\tilde{g}_H$, the fleur-de-lis feature persists in the full global fit, see Sec. 5.4. When we profile over Q as a nuisance parameter, this correlation broadens the 1-dimensional and 2-dimensional profile likelihood in $\tilde{g}_H$ by roughly a factor 2. As shown in the second and third panels of Fig. 5.6, the broadening affects significantly only the constraints in the $\tilde{g}_H$ direction, while those on $\tilde{g}_l$ are essentially unchanged compared to when $Q = m_V$. Although not shown, this is also verified for $\tilde{g}_M$.

We emphasize that the tree-loop cancellations that drive this effect are only very slightly affected by the renormalization group evolution of $f_{\phi,2}$, as illustrated by the dashed

lines including approximate renormalization group equations (RGE) contributions in Fig. 5.5. They really correspond to a choice of the unphysical matching scale, which can not be compensated by the well-defined change of renormalization scale of the low-energy SMEFT description. Adding higher orders in the loop expansion to the matching decreases the sensitivity to the matching scale. Similar effects, but with a much smaller numerical impact have been observed in Ref. [243].

5.4 SMEFT global analysis

In this section we discuss the results of the SMEFT global analysis, mapped to the parameter space of the heavy vector triplet model defined in Sec. 5.2.3 using one-loop matching relations. We derive constraints on the UV-parameters $\{\tilde{g}_H, \tilde{g}_q, \tilde{g}_l, \tilde{g}_M, \tilde{g}_{VH}\}$ defined by the Lagrangian in Eq. (5.10) for fixed values of the heavy vector triplet mass. We consider two benchmark values: $m_V = 4\,\text{TeV}$, to be compared with direct resonance searches by the ATLAS Collaboration, and $m_V = 8\,\text{TeV}$ for a consistent SMEFT analysis safely below any on-shell pole.

5.4.1 Resonance searches at high invariant masses

As mentioned in Sec. 5.2.4, in addition to more standard Higgs measurements, the global analysis includes constraints from searches for exotic particles in the WH and WW channels by the ATLAS Collaboration. In particular, two of these analyses [168, 197] have been newly implemented in SFITTER.

WH search

We consider the m_{WH} invariant mass distribution measured in Ref. [197] in the WH 1-tag category, and we compare it to a WH signal including dimension-6 corrections. This kinematic distribution extends up to $m_{WH} = 5\,\text{TeV}$ and the strongest constraints on BSM effects stem from the region around $m_{WH} = 2 - 2.5\,\text{TeV}$, where the measurement exhibits large under-fluctuations. A detailed description of the implementation of this analysis will be provided in a future work [1].

For equal values of the WCs, the largest correction to the m_{WH} spectrum is induced by the operator $\mathcal{O}_{\phi Q}^{(3)}$ [108–113, 167], that contributes via corrections to the qqV vertex and via a 4-point $qqVH$ interaction. The latter exhibits an enhancement at large partonic energies due to the missing s-channel propagator and is therefore dominant in the high-invariant-mass regime. Further significant corrections, albeit less momentum-enhanced, are induced by $\mathcal{O}_W$. All other SMEFT operators in the HISZ basis do not contribute significantly to WH production in the high-energy regime.

Figure 5.7 shows the results from a 2D-analysis of the m_{WH} distribution alone, fixing the matching scale $Q = m_V = 4\,\text{TeV}$ and considering only two $\tilde{g}$-couplings at a time. The top row in Fig. 5.7 shows $\tilde{g}_f \equiv \tilde{g}_q = \tilde{g}_l$ vs $\tilde{g}_H$, which matches the benchmark considered in the ATLAS analysis [197]. In this limit, the matching contribution to $f_{\phi Q}^{(3)}$ cancels
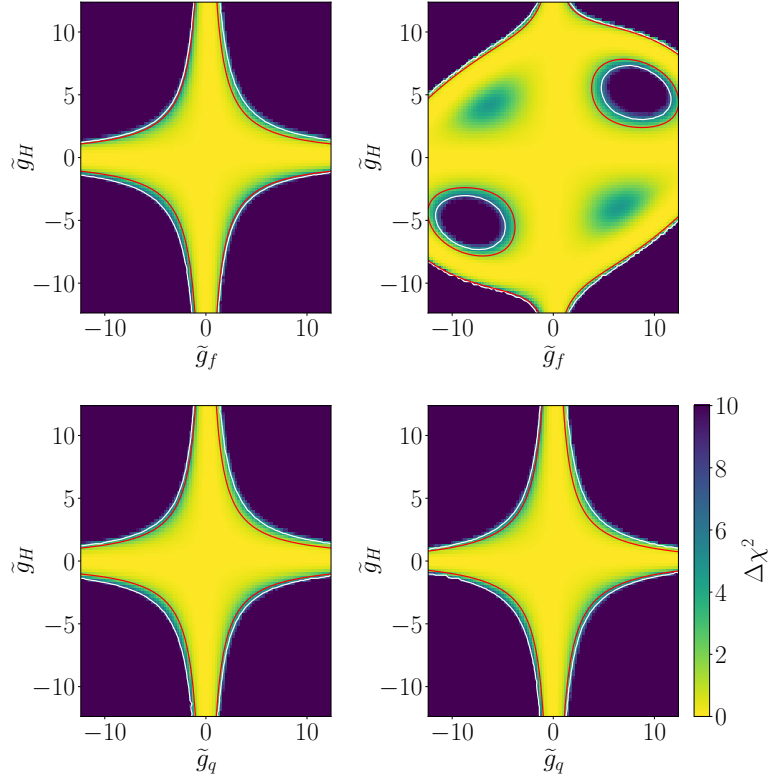
Figure 5.7: Two-dimensional (2D) fits of the WH resonance search of Ref. [197] only. We fix $m_V = 4\,\text{TeV}$ and $\tilde{g}_M = \tilde{g}_{VH} = 0$. Left: tree-level matching. Right: Loop-level matching. Top: with $\tilde{g}_l = \tilde{g}_q = \tilde{g}_f$. Bottom: with $\tilde{g}_l = 0$. In the top (bottom) row, red contours indicate $f_W = \pm 4$ ($f_{\phi Q}^{(3)} = \pm 0.8$) with $\Lambda = 1\,\text{TeV}$ and white contours indicate $\Delta\chi^2 = 5.991$.

exactly, both at tree and loop levels. As a consequence, the constraints are driven by f_W, whose matching expressions reduce to

$$\frac{f_W}{\Lambda^2} = 4.76\,\frac{\tilde{g}_H \tilde{g}_l}{m_V^2} \qquad\qquad \text{(tree)}$$

$$\frac{f_W}{\Lambda^2} \simeq \tilde{g}_l \tilde{g}_H \frac{4.71 + 0.019\,\tilde{g}_l \tilde{g}_H - 0.023\,\tilde{g}_l^2 - 0.057\,\tilde{g}_H^2}{m_V^2} \qquad \text{(tree+loop)}. \qquad (5.36)$$

The red contours in the plots indicate $f_W/\Lambda^2 = \pm 4\,\text{TeV}^{-2}$, which is representative of the 2σ boundaries $f_W/\Lambda^2 \in [-3.6, 4.4]\,\text{TeV}^{-2}$ found in a one-dimensional (1D) fit to the SMEFT parameters. In a slight abuse of language, here and in the following the $\Delta\chi^2 \leq 1\,(2.3)$ and $\Delta\chi^2 \leq 3.841\,(5.991)$ regions in 1D (2D) fits are sometimes referred to as 1σ and 2σ intervals, respectively. The fact that these lines coincide to a very good approximation with the 2σ contours (indicated in white) in Fig. 5.7 shows that the constraint on f_W is indeed the leading one. The bottom row shows $\tilde{g}_q$ vs $\tilde{g}_H$ for $\tilde{g}_l = 0$. In this case the cancellation in $f_{\phi Q}^{(3)}$ is spoiled and the constraints are dominated by this WC. Numerically, the matching expression is

$$\frac{f_{\phi Q}^{(3)}}{\Lambda^2} = \frac{\tilde{g}_H(\tilde{g}_l - \tilde{g}_q)}{m_V^2} \qquad\qquad \text{(tree)}$$

$$\frac{f_{\phi Q}^{(3)}}{\Lambda^2} \simeq 0.99 \frac{\tilde{g}_H(\tilde{g}_l - \tilde{g}_q)}{m_V^2} \qquad\qquad \text{(tree+loop)}, \qquad (5.37)$$

and the bottom panels in Fig. 5.7 show contours for $f_{\phi Q}^{(3)}/\Lambda^2 = \pm 0.8\,\text{TeV}^{-2}$, which is representative of the 2σ interval $f_{\phi Q}^{(3)}/\Lambda^2 \in [-0.90, 0.76]\,\text{TeV}^{-2}$ obtained in a 1D fit.

Finally, comparing the left and right panels in Fig. 5.7, it is worth noting that the impact of loop contributions to the matching is negligible in the case $\tilde{g}_l = 0$, but significant for $\tilde{g}_l = \tilde{g}_q$. This is a direct consequence of the form of the matching expression in the particular model considered. Loop terms only induce a very minor overall rescaling in the expression of $f_{\phi Q}^{(3)}$, Eq. (5.37), but they introduce a series of new terms in the expression of f_W, Eq. (5.36). Although numerically subdominant, the latter have a strong impact on the likelihood structure.

WW search

We consider the m_{WW} distribution measured in Ref. [168] in the WW 1-lepton category and ggF/Drell-Yan (DY) merged, high-purity signal region, that targets neutral resonances decaying to $W^\pm W^\mp$ pairs and covers invariant masses up to $m_{WW} = 4\,\text{TeV}$. We compare the measured distribution to a $W^\pm W^\mp$ production signal including SMEFT corrections. A detailed discussion of the implementation can be found in Sec. 4.3.1.

The $W^\pm W^\mp$ production process exhibits a greater complexity in the SMEFT compared to $W^\pm H$ in the high-energy limit. We find that, fixing all WCs to the same numerical value, the largest corrections are induced by the operators $\mathcal{O}_{\phi u}, \mathcal{O}_{\phi d}, \mathcal{O}_{\phi Q}^{(1)}, \mathcal{O}_{\phi Q}^{(3)}$ at quadratic level, that exhibit a large enhancement $\propto m_{WW}^2$. The origin of this behavior can be identified as a $qq\phi\phi$ contact interaction between two quarks and two Goldstone bosons induced by these operators, that dominates at high energies due to the equivalence theorem [245]. Effects induced by $\mathcal{O}_W, \mathcal{O}_B$, and $\mathcal{O}_{3W}$ have a weaker momentum-enhancement and are roughly two orders of magnitude smaller. Nevertheless, they were retained in the fit, as they are relevant for the global analysis in terms of both SMEFT and UV model parameters. In the former case, this measurement contributes significantly to improving the constraints on f_W, by roughly a factor two [1]. In the latter, it is important to stress that the matching expressions for a given UV model generally do *not* give homogeneous values for the WCs. Therefore a suppression of two orders of magnitude in the SMEFT predictions can be easily compensated in the matching, and the corresponding contributions to the signal may lead to significant constraints on the UV model parameters. In fact, for the WW analysis implemented here we find that the constraints projected on the $\tilde{g}_q - \tilde{g}_H$ and $\tilde{g}_f - \tilde{g}_H$ planes are entirely dominated by the contributions of f_W and $f_{\phi Q}^{(3)}$, the same two operators that lead in the WH case.

Figure 5.8 shows the results from a 2D-analysis of the m_{WW} distribution alone, fixing $Q = m_V = 4\,\text{TeV}$ and considering the same benchmarks as in Fig. 5.7. The red curves in Fig. 5.8 are again given by Eq. (5.36) and (5.37), but for different values of f_W and $f_{\phi Q}^{(3)}$, namely $f_W/\Lambda^2 = \pm 0.7\,\text{TeV}^{-2}$ and $f_{\phi Q}^{(3)}/\Lambda^2 = -0.27, +0.23\,\text{TeV}^{-2}$. Again, these values correspond to the 2σ-boundaries identified in 1D fits.

This analysis yields stronger bounds compared to WH because in this particular case the constraints are dominated by the tail of the distribution, in the region around $m_{WW} = 2.5 - 4\,\text{TeV}$, which exhibits under-fluctuations. Again, the effect of introducing
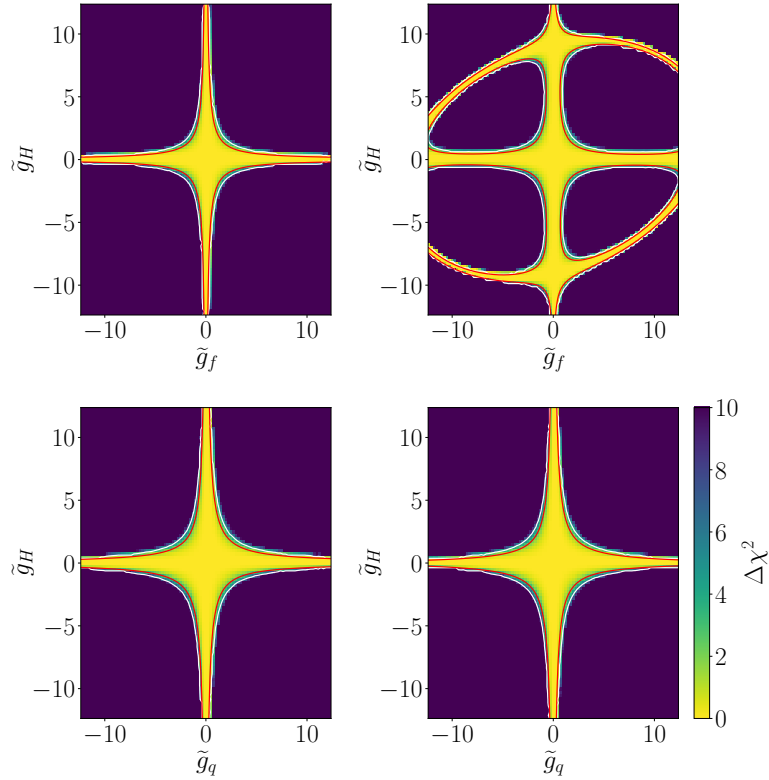
Figure 5.8: 2D fits of the WW resonance search of Ref. [168] only. We fix $m_V = 4\,\text{TeV}$ and $\tilde{g}_M = \tilde{g}_{VH} = 0$. Left: tree-level matching. Right: Loop-level matching. Top: with $\tilde{g}_l = \tilde{g}_q = \tilde{g}_f$. Bottom: with $\tilde{g}_l = 0$. In the top (bottom) row, red contours indicate $f_W = \pm 0.7$ ($f_{\phi Q}^{(3)} = 0.2$ or $f_{\phi Q}^{(3)} = -0.3$) with $\Lambda = 1\,\text{TeV}$ and white contours indicate $\Delta \chi^2 = 5.991$.

loop contributions to the matching expressions is only visible in the scenario dominated by f_W, for the same reasons as described above.

5.4.2 Global analysis results

Figure 5.9 shows the results of our global analysis, including the full data set described in Sec. 5.2.4 as well as the resonance searches discussed in Sec. 5.4.1, for a fixed value of the heavy vector triplet mass $m_V = 4\,\text{TeV}$. The analysis is performed varying $\tilde{g}_M$ and $\tilde{g}_{VH}$ within the physical region $\tilde{g}_M = -1\ ...\ 1$, $\tilde{g}_{VH} > 0$ and all other coupling parameters in the perturbative range $\tilde{g} = -4\pi\ ...\ 4\pi$.

Fixed matching scale

For a fixed matching scale $Q = m_V$ (red and orange lines in Fig. 5.9), we find that the SMEFT fit constrains significantly $\tilde{g}_l$ and $\tilde{g}_H$, while $\tilde{g}_M$, $\tilde{g}_q$, and $\tilde{g}_{VH}$ are essentially unconstrained. The striking difference between the constraints on the vector triplet couplings to leptons and to quarks is largely due to the fact that the SMEFT fit is dominated by EWPO constraints extracted at LEP, on which the leptonic interactions
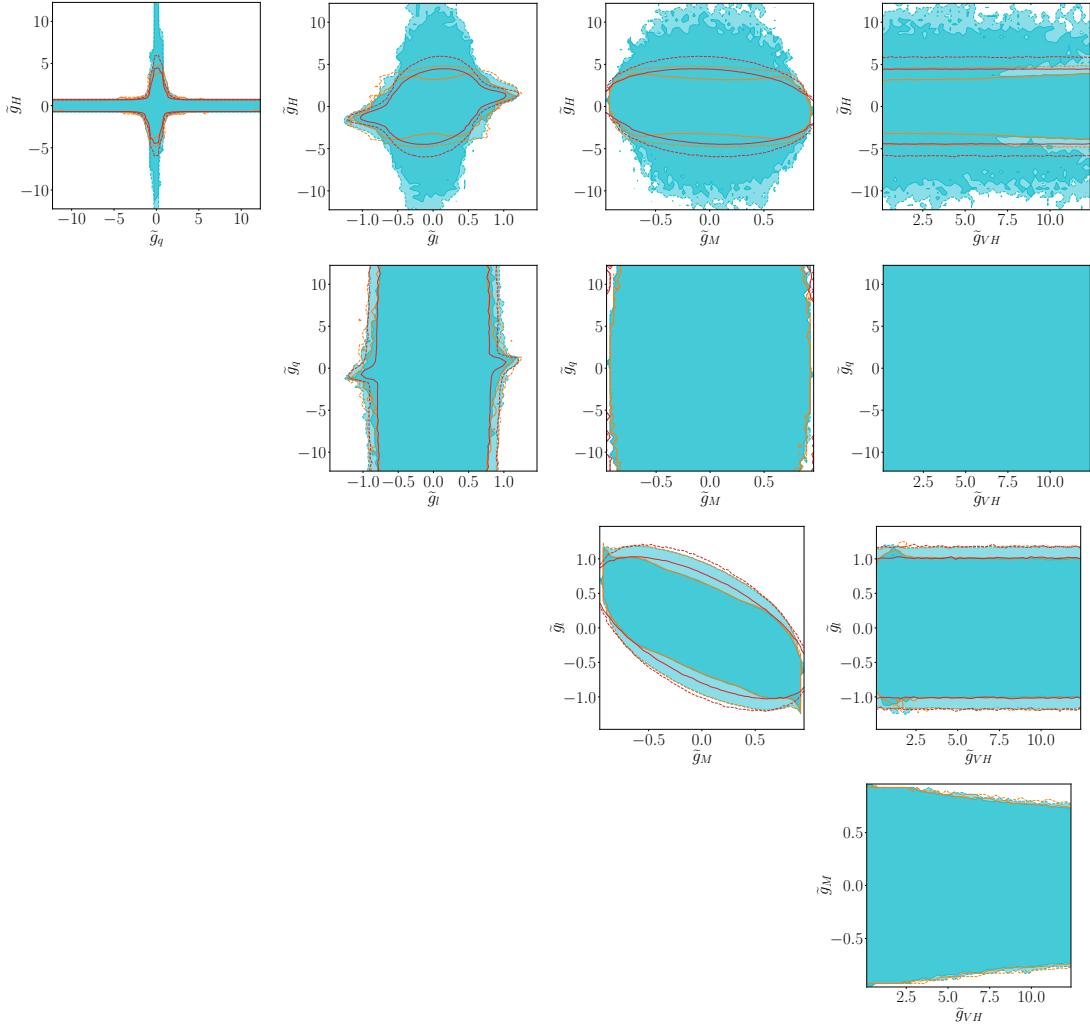
Figure 5.9: 5-parameter global fit of the full data set to the model parameters from Eq. (5.10) for fixed $m_V = 4 \, \text{TeV}$. Profiled $\Delta\chi^2 = 2.3$ ($\Delta\chi^2 = 5.991$) contours are shown as solid (dashed) lines. Red (orange) curves indicate the results obtained with tree (one-loop) matching onto the SMEFT and a fixed matching scale $Q = m_V$. The light blue region shows the results from one-loop matching, profiled over $Q = 500 \, \text{GeV} \, ... \, m_V$.

have a much stronger impact. We have verified that, indeed, removing EWPO constraints from the fit relaxes significantly the constraint on $\tilde{g}_l$.

The 2D projections show that $\tilde{g}_l$ is also anti-correlated to $\tilde{g}_M$. The reason is that, at tree-level, $\tilde{g}_l$ enters the matching expressions only in the combination $\tilde{g}_l + g_2\tilde{g}_M$, where g_2 is the $SU(2)$ coupling constant. Specifically, we find that the constraints in the $\tilde{g}_M - \tilde{g}_l$ plane are dominated by the constraint on f_{4L}, whose tree-level matching expression is quadratic in the relevant combination

$$\frac{f_{4L}}{\Lambda^2} = -\frac{(\tilde{g}_l + g_2\tilde{g}_M)^2}{4\tilde{m}_V^2} \; . \tag{5.38}$$

Therefore, for most values of $\tilde{g}_M$ and $\tilde{g}_l$, the constraints are driven by the limit for negative values of this WC. At one-loop, the matching expression is more complex and
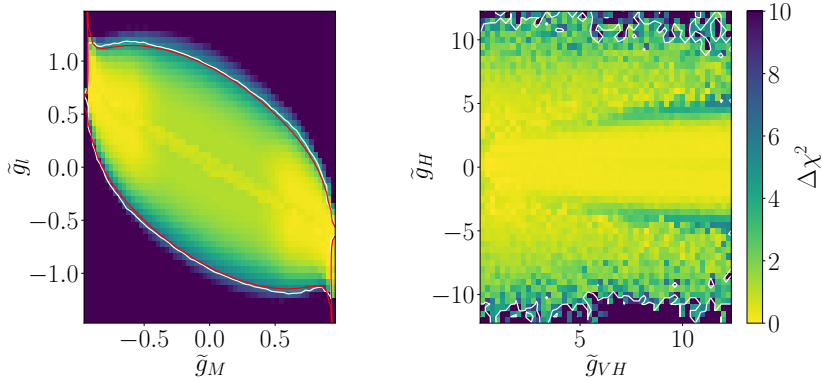
Figure 5.10: Heat map of the profiled $\Delta\chi^2$ distribution from the same fit as in Fig. 5.9, with one-loop matching and profiling over the matching scale. The red contours indicate $f_{4L}/\Lambda^2 = -0.014, +0.017$ TeV^{-2} and the white contours indicate $\Delta\chi^2 = 5.991$.

allows for positive values of f_{4L} in a region close to $|\tilde{g}_M| \simeq 1$ and $|\tilde{g}_l| \simeq 1$. The right panel in Fig. 5.10 shows that the 2σ boundary from the 5D likelihood (in white) matches very well the contours for $f_{4L}/\Lambda^2 = -0.014, +0.017$ TeV^{-2} (in red), corresponding to the 2σ interval derived from a 2D fit of f_{4L} and f_{BW}. Here a 2D fit is necessary owing to the strong correlation between f_{4L} and f_{BW}. A 1D fit would lead to an over-estimation of the constraints.

There are no major differences between tree and loop level matching when keeping the matching scale fixed $Q = m_V$. Only slight differences can be observed in the limits on $\tilde{g}_M$ and $\tilde{g}_H$. The effect on $\tilde{g}_H$ is completely washed out once the matching scale is allowed to vary, as we discuss below. Although less visible due to the different scales, an analogous anti-correlation is present in the $\tilde{g}_M - \tilde{g}_H$ plane, as $\tilde{g}_H$ also enters tree-level matching expressions exclusively in the combination $\tilde{g}_H + g_2\tilde{g}_M$. Because $\tilde{g}_H$ enters many WCs, both at tree and loop level, in this case it is not possible to identify one particular SMEFT parameter, or combination thereof, that drives the global bounds.

The constraint on $\tilde{g}_q$, on the other hand, is driven by that on $f_{\phi Q}^{(3)}$, whose matching expression is given in Eq. (5.37). This is consistent with the fact that $\tilde{g}_q$ only shows a non-trivial interplay with $\tilde{g}_H$. The cross-like shape emerging in the $(\tilde{g}_q, \tilde{g}_H)$ panel results from the superposition of the hyperbola-like shape expected from the $f_{\phi Q}^3$ matching expression, and of additional constraints on $\tilde{g}_H$ that introduce extra suppressions away from the two axes. Finally, $\tilde{g}_{VH}$ does not contribute to any dimension-6 operator at tree-level, so, in this limit, the likelihood is exactly flat in the corresponding direction. At one-loop $\tilde{g}_{VH}$ gives contributions to $f_W, f_{WW}, f_{\phi 2}, f_{t,b,\tau}$ and $f_{\phi Q}^{(3)}$. Among these, the dominant constraint stems from $f_{\phi 2}$, leading to the orange contours in the $\tilde{g}_{VH} - \tilde{g}_M$ and $\tilde{g}_{VH} - \tilde{g}_H$ planes.

Variable matching scale

Varying the matching scale as $Q = 500$ GeV ... $m_V = 4$ TeV, as shown as light blue region in Fig. 5.9, affects the constraints on $\tilde{g}_H$, while for the other parameters the dependence is negligible. This is what we expect from the toy results in Sec. 5.3.2 and Fig. 5.6, and we have verified that extending the range to $Q \gtrsim m_V$ does not add any significant feature
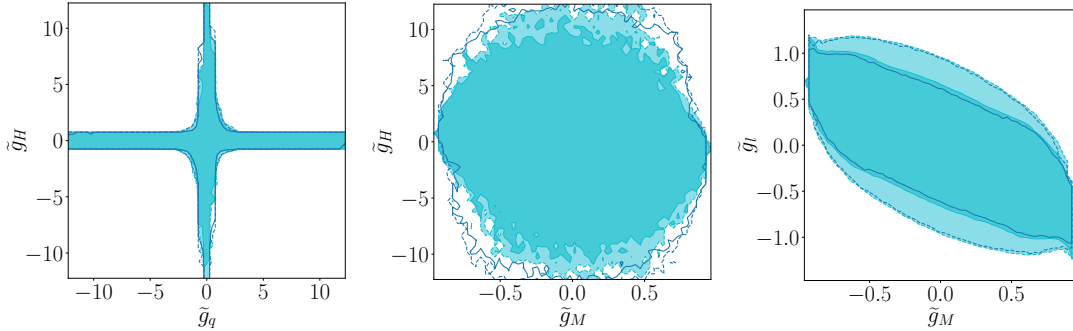
Figure 5.11: Impact of the high-energy kinematic distributions [168, 197, 239] on the global 5-parameter SMEFT fit for fixed $m_V = 4\,\mathrm{TeV}$. The solid regions include the full data set (same as Fig. 5.9), while the dark blue lines exclude the high-energy kinematic distributions. Solid (dashed) lines mark the $\Delta\chi^2 = 2.3$ ($\Delta\chi^2 = 5.991$) contours.

to the results. As for the 5-parameter fit, the main consequence of variable Q is that, for $Q \lesssim 2.4\,\mathrm{TeV}$, the matching expressions of $f_{\phi 2}$ and $f_{t,b,\tau}$ acquire a new zero. Because these operators are the dominant source of constraints on $\tilde{g}_H$, this results in a broader allowed region for this parameter, which is largest close to the $Q \simeq 2.4\,\mathrm{TeV}$ threshold. This effect washes out the correlation between $\tilde{g}_H$ and $\tilde{g}_M$ mentioned above.

At $Q \simeq 2.4\,\mathrm{TeV}$, the most constraining WC is $f_{\phi 2}$, which is responsible for the outermost region of the 2σ contours for $\tilde{g}_H$ in Fig. 5.9. The inner structure of the likelihood, including the 1σ contour, can not be explained in terms of a single WC. It is the result of a non-trivial interplay between several effects, including $\tilde{g}_H$ entering a large number of WCs and profiling over the matching scale.

It is also interesting to look at the finer structure of the profiled likelihood. In Fig. 5.10 we show $\Delta\chi^2$ for the same 2D projections as before. We can see that the best-fit points are focused in regions where $|\tilde{g}_M| > 0.5$. This effect emerges in the 5-parameter fit with one-loop matching, irrespective of whether the matching scale is fixed or varied. It is the same effect as observed for the 3-parameter fit varying the heavy vector mass in Fig. 5.3, and it is due to the EWPO preferring a best-fit point away from the SM. In particular, we have checked that the observed substructures are entirely dominated by less than 1σ deviations in $A_l(\mathrm{SLD})$ and m_W. In addition, the measurements of σ_h^0, R_l^0, $A_{FB}^{0,l}$, A_c reinforce the deviation through correlations. If future measurements with reduced uncertainties confirmed the present deviations from the SM, this would lead to exclusion limits with intricate patterns.

Impact of high energy measurements

It is well known [36] that kinematic distributions probing high invariant masses have significant impact on global fits to the SMEFT parameters. In our analysis, we confirm this behavior for the two analyses described in Sec. 5.4.1, which are found to constrain significantly f_W, $f_{\phi d}^{(1)}$ and f_{3W}. Unfortunately, once the SMEFT is mapped onto the heavy vector triplet model, the constraining power of these measurements is diminished. This is shown in Fig. 5.11, where the results of Fig. 5.9 are compared to those from a 5-parameter fit where the three analyses of Refs. [168, 197, 239] are removed (dark blue
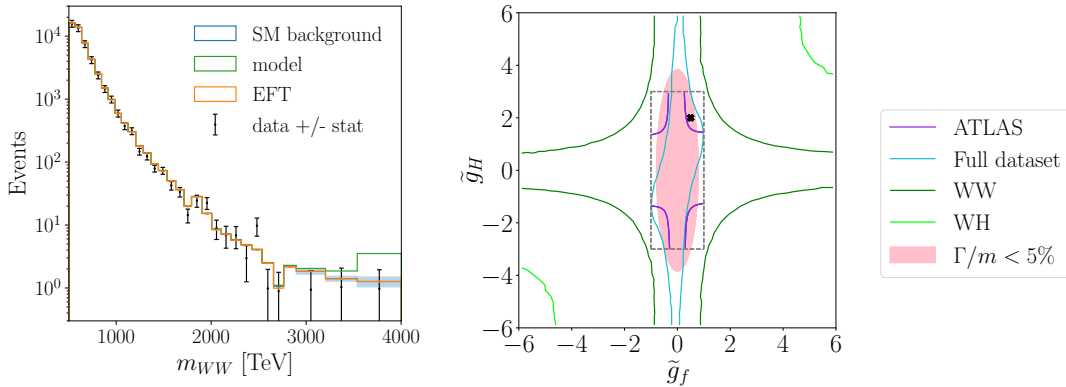
Figure 5.12: Left: Z' prediction for $m_V = 4\,\mathrm{TeV}$, $\tilde{g}_H = 2$, $\tilde{g}_f = 0.5$ (shown by a star in the right panel) for the WW search [168], compared to the SMEFT prediction. Right: SMEFT limits ($\Delta\chi^2 = 5.991$) for $m_V = 4\,\mathrm{TeV}$ and profiled over the matching scale, for the WW and WH distributions alone and the full dataset. We also show the 95%CL exclusion from the WH resonance search [197]. The gray box marks the ATLAS search region, the narrow-width is shaded in pink.

line). The lack of visible impact of the high-energy kinematic distributions is very much due to the specific model and the corresponding numerical behaviour of the matching formulae. As discussed above, the main constraints on the vector triplet parameter space are dominantly associated to those on $f_{4L}, f_{\phi2}$ and $f_{\phi Q}^{(3)}$, which are only marginally improved by these searches.

SMEFT vs direct searches

A key question we would like to address in this work is whether a global SMEFT analysis can be competitive with direct searches in constraining a given UV model. Figure 5.12 compares the constraints in the $(\tilde{g}_f, \tilde{g}_H)$ plane obtained in the direct search of WH resonances by ATLAS, Ref. [197], and from 2D SMEFT fits to different sets of observables. In particular, the light green line indicates the SMEFT constraints obtained from the same distribution as in the direct search. For all lines in this plot, the heavy triplet mass is fixed to $m_V = 4\,\mathrm{TeV}$, the maximum value accessible by the resonance search. Strictly speaking, the direct and indirect constraints extracted from the same measurement apply to complementary regions of the parameter space: the former are valid for masses $m_V \lesssim 4\,\mathrm{TeV}$ and for narrow vector triplets within the pink-shaded region of Fig. 5.12, while the latter hold for $m_V \gg 4\,\mathrm{TeV}$ irrespective of the resonance width. Obviously, a comparison should be taken with a grain of salt.

Nevertheless, it can be instructive to examine the interplay between the signals produced by a heavy resonance and by its corresponding SMEFT approximation. The left panel of Fig. 5.12 shows the m_{WW} resonant distribution obtained for a benchmark point at $m_V = 4\,\mathrm{TeV}$, $\tilde{g}_H = 2$, $\tilde{g}_f \equiv \tilde{g}_l = \tilde{g}_q = 0.5$, compared to the ATLAS measurement [197] (black data points) and the SMEFT signal matched to this benchmark model at dimension six. This point is indicated by a cross in Fig. 5.12 (right), and it is excluded at 95%CL by both the ATLAS WH and WW searches, but falls within the 2σ-allowed region of our SMEFT global analysis. This discrepancy is obvious from the high-energy m_{WW}

tail, where aside from the mass peak the dimension-6 SMEFT also misses the initial rise of the distribution. Among the WCs that contribute to WW production, only $f_W/\Lambda^2 = 0.28\,\mathrm{TeV}^{-2}$ takes a value above the permille level, while $f_{\phi Q}^{(3)} = 0$ because $\tilde{g}_q = \tilde{g}_l$. This results in SMEFT signals of only a few percent across the entire m_{WW} distribution, which are always well within the uncertainties. It is worth pointing out that in such a situation the best place to look for the SMEFT signal might not just be the bins where the energy enhancement is largest, but rather those where the uncertainties are smallest.

While not surprising, these conclusions do not extend to arbitrary BSM scenarios. One characteristic of the case examined here is that the resonance is narrow. As a consequence, the effect in m_{WW} is only visible close to m_V, where the SMEFT expansion immediately breaks down. The situation improves when we include higher-dimensional operators [204, 246]. At dimension six, the matching to our specific model suppresses all energy-enhanced SMEFT contributions to WW production, so the signal is under-estimated across the em_{WW} distribution. This does not have to be the case in other BSM models. For instance, it is possible that the dimension-6 approximation over-estimates the model predictions, in which case the dimension-8 contributions need to be large and negative, and the truncated SMEFT constraints appear more stringent than those from direct searches.

Going beyond the comparison of resonance searches and SMEFT analyses for one measurement, the true power of the SMEFT approach is that it allows to combine a large number of different measurements. This will always improve the sensitivity of the SMEFT analyses and, on the other hand, it allows to derive more general conclusions, by constraining all model parameters simultaneously, as shown in Fig. 5.9. The light blue lines in Fig. 5.12 show the constraints from a 2-parameter SMEFT fit to the entire dataset employed in this work. Consistent with the discussions above, these limits are dominated by EWPO, for which the SMEFT expansion is valid. In particular, the constraint on $\tilde{g}_f$ is dominated by the leptonic component $\tilde{g}_l$, which in turn is mostly associated to the f_{4L} WC. Comparing these limits to those from the ATLAS WH-search, we find that the latter are slightly stronger for $|\tilde{g}_H| \gtrsim 1$ (with the caveat that they are only valid in the narrow width regime), while the former dominate for $|\tilde{g}_H| \lesssim 1$. Here, the WH search has an unconstrained direction along the $\tilde{g}_H = 0$ axis, that is broken by the EWPO in the SMEFT fit [207].

Heavy vector triplet (HVT) results

One of the main motivations for the SMEFT formalism is that it allows us to derive constraints on new particles with masses beyond the reach of direct searches. In this spirit, we can extend our SMEFT constraints on the $\tilde{g}$ parameters for a heavy triplet mass to $m_V = 8\,\mathrm{TeV}$. Now, the dimension-6 SMEFT approximation is valid all over the kinematic measurements discussed above. The corresponding results in Fig. 5.13 can be directly compared to those in Fig. 5.9 for $m_V = 4\,\mathrm{TeV}$. As expected, all the bounds on the model parameters are weaker for heavier values of m_V (see also Fig. 5.3). However, a notable feature is that the limits do not simply scale with a factor proportional to m_V, as one would naively expect from the SMEFT analysis at dimension six. The reason is that the matching expressions that relate the WCs to the model parameters are generally non-trivial and do not scale universally with $(\tilde{g}_i/m_V)$, as can be seen for instance in Eq. (5.33). Moreover, as we are considering a BSM state that is not a singlet under
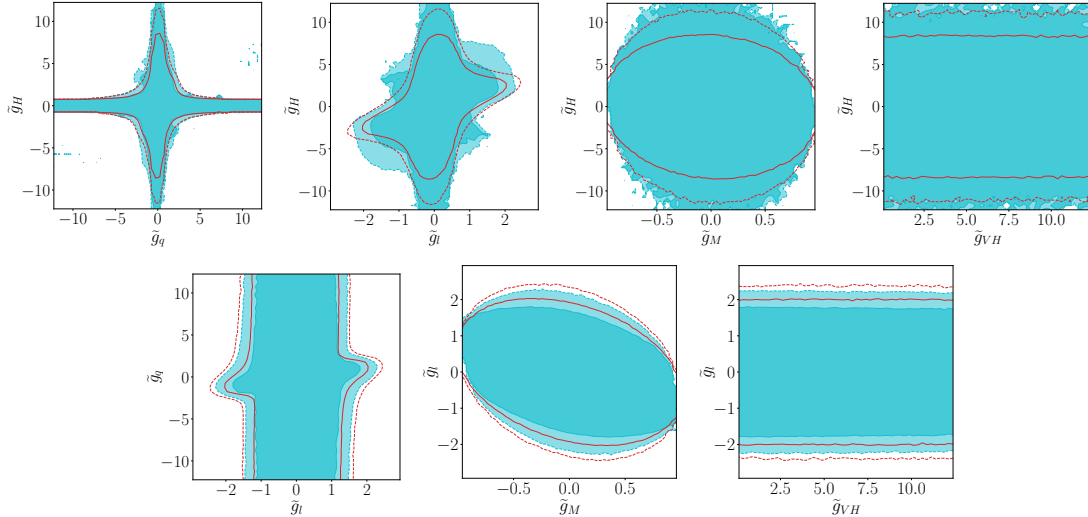
Figure 5.13: 5-parameter fit to the full data set for the model parameters in Eq. (5.10) for fixed $m_V = 8\,\text{TeV}$. Each panel shows profiled $\Delta\chi^2 = 2.3$ (solid) and $\Delta\chi^2 = 5.991$ (dashed) contours. Red curves correspond to tree-level matching, the light blue region to one-loop matching, profiled over three $\tilde{g}$ parameters plus the matching scale $Q = 500\,\text{GeV} \dots m_V$. The panels for $\tilde{g}_M - \tilde{g}_q$ $\tilde{g}_{VH} - \tilde{g}_q$ and $\tilde{g}_{VH} - \tilde{g}_M$ are not shown as they are unconstrained in the explored ranges.

$SU(2)$, the EW gauge coupling g_2 contributes to the matching independently of the $\tilde{g}$ parameters. The result is that the degeneracy between $\tilde{g}_i$ and m_V is largely broken in the matching, leading to a complex likelihood structure that changes significantly with m_V.

5.5 Conclusions

We have presented a global analysis of a SM extension with a gauge-triplet vector resonance in terms of the dimension-6 SMEFT Lagrangian. We have performed a global SFITTER analysis including electroweak precision observables, Higgs and di-boson measurements as well as resonance searches at the LHC, and have compared our results with limits obtained from direct searches. To relate the full model and the SMEFT we have employed one-loop matching with a focus on the theory uncertainties from the choice of the matching scale.

First, we have shown that the theory uncertainty due to the choice of the matching scale can have a large effect on the global analysis. In particular, the bounds on the coupling of the new vector to the SM-Higgs are significantly weakened once we profile over a variable matching scale, illustrating how all theory uncertainties need to be taken into account at least once we translate SMEFT results back into models.

Comparing the SMEFT results with direct searches reveals an intriguing complementarity. Direct and SMEFT searches are reliable in different parameter regions; while direct searches are sensitive to narrow resonances with kinematically accessible masses, SMEFT searches apply to energies sufficiently below the resonance mass. The SMEFT analysis can be sensitive to the onset of the resonance, but a reliable description of this region requires a tower of higher-dimensional operators. Specifically for the vector-triplet model, the SMEFT model for the high-energy tail of kinematic distributions turned out less

sensitive than the resonance search, and therefore provided conservative constraints. On the other hand, the SMEFT analysis can probe vector masses beyond the reach of resonance searches. Here, we found that the one-loop matching dampens the sensitivity decrease of the SMEFT analysis compared to the naively expected scaling.

While SMEFT analyses can not replace model-specific searches for new physics, they add valuable constraints from a large variety of measurements and are sensitive to new physics scales beyond the reach of resonance searches. Only this complementarity of direct and indirect searches allows us to make best use of current and future LHC data.

Summary and outlook

In this work, we motivated a bottom-up approach to set limits on BSM physics. We demonstrated how SMEFT global analyses can be used as a stepping stone to derive limits on UV models.

First, we extended our SMEFT global analysis for Higgs and electroweak (EW) processes. We included and tested over 30 new measurements in SFITTER, among them new high kinematic searches for VH and VV production from both ATLAS and CMS, as well as a boosted Higgs production measurement by ATLAS. We expanded our basis with two operators, which could now be constrained thanks to the new measurements. Additionally, because the newly added chromomagnetic operator was previously observed to be the main link between the top and Higgs sectors [39, 40], the constraints on this operator from a separate SFITTER analysis in the top sector we introduced.

We were able to compare the profiled and marginalized results of a global SMEFT analysis starting from the same set of measurements. We found that, using the old dataset from Ref. [36], the two methods yielded very similar results. The only visible difference being small shifts in the central value of some likelihood distributions. Whereas for the new dataset, the constraints on the WCs were very different for two operators in particular f_B and $f_{\phi u}^{(1)}$. The main reason for the discrepancy can be attributed to drastic volume effects when marginalizing.

Specifically, this discrepancy can be traced back to a particular measurement, a high kinematic WW search by ATLAS with an under-fluctuation in the highest kinematic bin. The SM point and the region close to it are slightly disfavoured by this under-fluctuation. Indeed, the only way to accommodate it is to have a combination of non-zero WCs that lead to large interference terms with the SM. It also turns out that the volume of parameter space allowed around the SM point is small compared to the one around the combination of non-zero WCs. Thus, when marginalizing, the region with the bigger volume blows up in importance. However, this is not the case for profiling because only the highest likelihood point is relevant in that case and not the density of point around it. This does not mean that one method is wrong, but that they ask different questions which means they might yield different answers.

In the second part of this work, we implemented a new matching interface in SFITTER. This allowed us to perform an analysis in the heavy vector triplet (HVT) model space, using all the data, predictions and statistical tools already in place for the SMEFT global analysis.

The main takeaway here is that constraints from direct searches and SMEFT global analyses are highly complementary. For our specific example, where direct searches existed, they were more powerful than constraints from the same measurement set through a SMEFT framework. However, the SMEFT global analysis still provides constraints beyond the reach of direct searches and it also combines many measurements, which put together yield competitive constraints. Another upside of a global analysis is that, because it combines a big number of measurements, it can constrain all the UV model parameters at once, which reveals potential correlations between them.

We have also shown that, because of the specific numerics of the matching, heavy resonance searches for VH and VV production, when used as high kinematic distributions, do not have as significant an impact on the HVT model analysis as they do on the regular SMEFT analysis. For this particular model, a lot of the constraints are dominated by the EWPO, because the WCs constrained by these measurements are enhanced in the matching equations.

Finally, when setting constraints through matching a UV model to the SMEFT, one should match at least at 1-loop level and treat the matching scale as a nuisance parameter, i.e. an additional theory uncertainty. We showed that this can affect the limits for some parameters quite significantly.

Now that this bottom-up pathway to UV models is implemented in SFITTER, many other opportunities are open. New UV models ought to be explored using the same framework. Scalar singlet extensions of the SM have already been studied in Ref. [41] and heavy vector triplet (HVT) extensions were presented in this work (or equivalently Ref. [2]). Many other interesting models remain: the two-Higgs-doublet model (2HDM), vector-like leptons, or the minimal supersymmetric Standard Model (MSSM) in the decoupling limit.

As we have seen the UV model analysis is only as strong as the SMEFT analysis behind it. Thus, implementing new and precise measurements remains a priority. For now, the accuracy of our measurements' implementation is limited to broad predefined uncertainty categories, for which we assume some correlations. Being able to use likelihoods provided by the experiments would greatly improve this accuracy, thanks in particular to the added information on correlations between uncertainties. Additionally, it could help resolve the tension that exists between the desire to implement measurements quicker, whilst still taking into account the full breakdown of the uncertainties. Implementing new measurements in SFITTER from experimental likelihoods will be explored in an upcoming work.

Additionally, extending the SMEFT analysis to include more operators and processes, will not just improve the SMEFT study itself, but the potential UV models to be explored. To this end, an important step will be to combine the SFITTER analyses in the Higgs and top sectors. Beyond that, other processes affecting the flavor sector at the LHC and other experiments such as Belle II or neutrino experiments [247] may provide competitive constraints on current and new operators alike.

High-luminosity LHC (HL-LHC)

Figure A.1 shows the projected limits obtained with a marginalized treatment for the high-luminosity LHC (HL-LHC) on the 21 SMEFT Wilson coefficients (WCs) presented in Eq. (2.3). We use the full set of measurements presented in Sec. 4.4, where all the LHC measurements were set to their background values and their luminosity scaled to $4\,\mathrm{ab}^{-1}$. The electroweak precision observables (EWPO) from LEP are kept the same as in the previous analyses. We also derive the projected high-luminosity limits assuming halved theory and systematic uncertainties.

A significant gain is expected on the invisible branching ratio $\mathrm{BR}_{\mathrm{inv}}$ as well as the Yukawa corrections f_t, f_b and f_τ. The constraints improve for most of the other WCs, with a few exceptions. Limits on f_{tG} and f_{GG} do not change because the main constraints on these operators stem from the top analysis, which we did not update. $f_{\phi e}^{(1)}$, $f_{\phi 1}$, f_{4L} and f_{BW} also exhibit stable constraints, because they are mostly set by the EWPO. Both the top constraints and the EWPO are also the reason why the constraints are not always centred around zero. Finally, the only operator for which the constraints worsen is f_{3W}. This particular operator is especially sensitive to high kinematic searches for VV. Thus, the pure background assumption may lead to a reduced constraining power, as there are no under-fluctuations in the higher bins of the distributions.

Once we also consider improved systematic and theoretical uncertainties, the limits on all WCs improve—sometimes significantly, as for f_μ or f_-. In the case of f_μ, this can be understood considering that the one analysis constraining this coefficient has a significance of only 3.0 standard deviations and is dominated by large experimental uncertainties.

Figure A.1: Green: 21-dimensional SFITTER analysis with all updated measurements included, where all LHC measurements were scaled to a high-luminosity of $4\,\mathrm{ab}^{-1}$ and set to their background values. The electroweak precision observables (EWPO) from LEP are kept the same as in the previous analyses. Purple: a second set of limits is derived setting all systematic and theoretical uncertainties to half their current values. We show the 68% and 95%CL error bars from a consistent marginalization treatment of all the nuisance parameters and WCs. Blue: current marginalized limits already presented in 4.27.

Global SMEFT analysis: numerical results

Table B.1 reports the numerical values of the boundaries of the 68% and 95%CL intervals shown in Fig. 4.27.

Coefficient	Marginalised		Profiled	
	68% CL	95% CL	68% CL	95% CL
f_{GG}	[1.61, 7.49]	[-2.17, 8.75]	[3.79, 8.28]	[-1.09, 9.50]
f_B	[-5.49, -3.38]	[-8.20, 10.05]	[-6.49, 5.79]	[-8.69, 10.08]
	[0.74, 8,84]			
$f_{\phi 2}$	[-1.35, 2.95]	[-3.51, 5.11]	[-2.07, 3.68]	[-4.59, 6.55]
f_μ	[-5.01, 8.43]	[-7.45, 21.88]	[-3.79, 9.66]	[-8.68, 21.88]
f_t	[-0.01, 4.09]	[-2.05, 6.47]	[-0.80, 3.68]	[-3.56, 5.75]
f_b	[-1.19, 2.28]	[-3.06, 3.88]	[-0.60, 3.44]	[-3.03, 5.33]
f_τ	[-0.78, 1.66]	[-2.11, 2.99]	[-1.88, 1.00]	[-3.66, 2.55]
f_-	[-6.16, -0.65]	[-7.73, 2.89]	[-5.34, 2.28]	[-7.75, 5.09]
$f_+ \times 10$	[1.07, 8.21]	[-3.21, 11.79]	[0.36, 8.93]	[-3.93, 13.93]
$f_{tG} \times 10$	[2.05, 6.82]	[-0.93, 7.72]	[3.53, 7.12]	[-0.36, 8.02]
$f_W \times 10$	[2.64, 16.43]	[-4.26, 24.47]	[1.25, 21.80]	[-8.35, 30.03]
$f_{BW} \times 10$	[0.86, 8.42]	[-2.91, 12.19]	[1.57, 9.82]	[-2.83, 14.22]
$f_{3W} \times 10$	[-5.0, 3.62]	[-8.7, 7.31]	[-5.31, 6.89]	[-10.19, 9.94]
$f_{\phi Q}^{(3)} \times 100$	[-11.61, 12.38]	[-18.01, 25.17]	[-1.99, 23.60]	[-13.19, 34.80]
$f_{\phi u}^{(1)} \times 100$	[-14.22, -7.98]	[-18.60, -2.17]	[-15.70, -0.90]	[-22.00, 15.80]
	[4.25, 16.01]	[0.14 18.87]	[2.70, 10.20]	
$f_{\phi d}^{(1)} \times 100$	[-8.51, 3.04]	[-13.84, 8.37]	[-8.64, 6.07]	[-14.69, 12.13]
$f_{\phi 1} \times 100$	[-0.37, 7.32]	[-4.22, 11.17]	[-0.37, 7.88]	[-4.22, 12.83]
$f_{4L} \times 100$	[-2.7, -0.46]	[-3.82, 0.66]	[-2.86, -0.46]	[-4.14, 0.82]
$f_{\phi Q}^{(1)} \times 100$	[1.2, 7.6]	[-2.8, 9.2]	[-1.20, 5.60]	[-4.00, 8.40]
$f_{\phi e}^{(1)} \times 100$	[-4.58, -1.22]	[-6.5, 0.46]	[-5.06, -1.46]	[-6.98, 0.67]
$\mathrm{BR}_{\mathrm{inv}}$	[0, 3.04]	[0, 6.88]	[0, 4.64]	[0, 9.44]

Table B.1: Numerical values for the results shown in Fig. 4.27.

Table B.2 report the numerical values of the boundaries of the 68% and 95%CL intervals shown in Fig. A.1.

Coefficient	$L = 4\,\mathrm{ab}^{-1}$		$L = 4\,\mathrm{ab}^{-1}, \sigma_{\mathrm{syst+theo}} = \mathrm{half}$	
	68% CL	95% CL	68% CL	95% CL
f_{GG}	[0.42, 5.45]	[-1.78, 7.02]	[-0.18, 4.03]	[-1.42, 6.01]
f_B	[-0.41, 3.68]	[-3.04, 6.02]	[-0.21, 2.2]	[-1.74, 3.3]
$f_{\phi 2} \times 5$	[-2.85, 4.64]	[-9.09, 9.63]	[-1.17, 3.89]	[-4.2, 6.42]
f_μ	[-5.01, 5.99]	[-9.9, 21.88]	[-1.34, 2.32]	[-3.79, 5.99]
$f_t \times 5$	[-4.77, 3.74]	[-9.63, 8.61]	[-3.09, 2.17]	[-5.72, 4.8]
$f_b \times 5$	[-3.96, 2.57]	[-9.19, 7.8]	[-1.91, 2.11]	[-4.32, 4.12]
$f_\tau \times 5$	[-1.45, 3.3]	[-6.2, 7.1]	[-1.01, 1.88]	[-2.75, 3.03]
$f_- \times 5$	[-14.31, 0.84]	[-22.39, 5.89]	[-4.88, 1.47]	[-8.06, 4.12]
$f_+ \times 10$	[0.36, 7.5]	[-3.93, 11.07]	[-1.07, 3.93]	[-3.93, 6.79]
$f_{tG} \times 10$	[-0.13, 4.13]	[-1.46, 6.0]	[-0.14, 3.39]	[-1.18, 5.06]
$f_W \times 10$	[0.59, 7.28]	[-2.75, 12.63]	[0.29, 4.55]	[-2.03, 6.48]
$f_{BW} \times 10$	[-0.05, 7.15]	[-3.42, 11.0]	[-1.5, 3.88]	[-3.98, 7.19]
$f_{3W} \times 10$	[-4.44, 5.17]	[-8.92, 7.09]	[-3.03, 3.29]	[-5.35, 4.62]
$f_{\phi Q}^{(3)} \times 100$	[-0.9, 11.55]	[-8.37, 19.01]	[-1.44, 7.22]	[-5.78, 11.55]
$f_{\phi u}^{(1)} \times 100$	[-1.45, 6.44]	[-6.3, 8.86]	[-1.63, 3.64]	[-4.5, 6.51]
$f_{\phi d}^{(1)} \times 100$	[-4.21, 3.46]	[-8.4, 7.65]	[-2.89, 2.97]	[-5.6, 6.13]
$f_{\phi 1} \times 100$	[-1.1, 6.44]	[-4.88, 11.3]	[-2.51, 3.29]	[-5.41, 6.67]
$f_{4L} \times 100$	[-2.37, 0.02]	[-3.65, 1.14]	[-1.46, 0.21]	[-2.43, 1.04]
$f_{\phi Q}^{(1)} \times 100$	[-0.21, 2.65]	[-2.11, 4.32]	[-0.32, 1.74]	[-1.45, 2.86]
$f_{\phi e}^{(1)} \times 100$	[-4.23, -0.69]	[-5.89, 1.44]	[-2.68, -0.24]	[-4.1, 0.98]
$\mathrm{BR}_{\mathrm{inv}}$	[0, 1.05]	[0, 2.26]	[0, 0.85]	[0, 1.75]

Table B.2: Numerical values for the results shown in Fig. A.1.

Acknowledgments

Ode to all the people who got me through

First and foremost was my supervisor
Tilman Plehn the super energizer
He fished me out of a flood of emails
Gave me a group of colleagues tough as nails

Ilaria who knows everything
Heartfelt chats we shared late in the evening
Sebastian, gentle friend, even tempered
Till he smells falsehood that must be slaughtered
Michel, tech genius, too nice to be proud
His dating life gripped the coffee room crowd
Nina my witty office confidante
Keep Dropbox safe from fire incident!
Nikita completed our grand Higgs team
Shy except for jokes, eyes lit with a gleam

Oh what a team we made, coding our way
Oh how many bugs did we have to slay
Nemo our ally, SFitter our foe
We all shared the high, rose up from the low

And on the long journey to a degree
Many more friends shared in my gaiety

Benedikt, king of the colourful socks
Nathalie got all men to dance, she rocks!
Theo, ideal travel companion
Tanmoy proved himself cooking champion
Anke, my vital SFitter savior
Lennart, proud Sharkow chains co-inventor
Barry, Irish by accent and green wear
Luigi, you do need holidays, I swear
Anja, the machine learning powerhouse
Jörg and physics chats about to let loose
Marco for his boundless optimism
Lennert and his axion enthusiasm
Peter, Ramon, not to rain on the pub
Buffalo was never a secret club
Nathan, Jonas, Sofia next lesson
We will focus on French cursing cannons
Claudius, take care of the kindergarten
At home and at work they will soon brighten

Lorenz's LaTeX talent is paramount
In short, so many friends I cannot count

Let us all sing as we come together
"All hail Bob, our supreme office leader!"
Let's celebrate with pizza, darts and beer
Not even the bats could dampen our cheer

Matching triplets for months with Benjamin
And Michael until the code came clean
Getting caught up in SMEFT anomalies
Wolfgang and Nils will solve the oddities
Chasing phonons with Angelo and Tom
Taking bookish detours off thesis norm
The PhD that was once marathon,
Now shorter than a sprint, demands action
Quick quick the thesis has to be written
And a committee ought to be chosen:
I'm very grateful to Ulrich Uwer,
To Richard Schmidt, to Björn Malte Schaefer

We're nearing the end, must get to the root
What secret gift nourishes the recruit
What miracle fuels a PhD's stove
The only answer, dear reader, is love
Unconditional, ever-present, pure
It gave me the strength to sometimes endure
Often celebrate, always carry on
All thanks to my loved ones, those I lean on

Friends who stayed in touch despite the distance
Our zoom calls offered support and guidance
Those who came all the way to visit me
Your warm presence filled those weekends with glee
Those whom I met here, hope you will drop by
Wherever I am next, just come say hi

My family, be it through blood or heart
In everything I do you have a part
Papa, Maman, Marie, Nathan, my rocks
When we're together, wish I could stop clocks
I owe so much to my five grandparents
You raised us curious, kind, and valiant
Big thanks to my cousins, aunts and uncles
For cocooning me in safe love bubbles

For eight years, I've had the felicity
To be part of a second family
They always welcome me into their fold
Even while locked down, when COVID took hold
My bound to them strengthens everyday
For my love for you, Jean, is here to stay
You are my other-half, best friend, partner
Each word, each touch, makes my heart grow fonder

Bibliography

[1] I. Brivio, S. Bruggisser, N. Elmer, E. Geoffray, M. Luchmann and T. Plehn, *To Profile or To Marginalize – A SMEFT Case Study* (2022), doi:10.48550/ARXIV.2208.08454, https://arxiv.org/abs/2208.08454.

[2] I. Brivio, S. Bruggisser, E. Geoffray, W. Killian, M. Krämer, M. Luchmann, T. Plehn and B. Summ, *From models to SMEFT and back?*, SciPost Physics **12** (2022), doi:10.21468/scipostphys.12.1.036, https://doi.org/10.21468%2Fscipostphys.12.1.036, arXiv:2108.01094.

[3] A. Esposito, E. Geoffray and T. Melia, *Effective field theory for acoustic and pseudoacoustic phonons in solids*, Physical Review D **102** (2020), doi:10.1103/physrevd.102.105009, https://doi.org/10.1103%2Fphysrevd.102.105009, 2006.05429.

[4] G. Aad *et al.*, *Observation of a new particle in the search for the Standard Model Higgs boson with the ATLAS detector at the LHC*, Phys. Lett. B **716**, 1 (2012), doi:10.1016/j.physletb.2012.08.020, arXiv:1207.7214.

[5] S. Chatrchyan *et al.*, *Observation of a New Boson at a Mass of 125 GeV with the CMS Experiment at the LHC*, Phys. Lett. B **716**, 30 (2012), doi:10.1016/j.physletb.2012.08.021, arXiv:1207.7235.

[6] F. Zwicky, *Die Rotverschiebung von extragalaktischen Nebeln*, Helvetica Physica Acta **6**, 110 (1933).

[7] H. Andernach and F. Zwicky, *English and Spanish Translation of Zwicky's (1933) The Redshift of Extragalactic Nebulae*, doi:10.48550/ARXIV.1711.01693 (2017).

[8] V. C. Rubin and J. Ford, W. Kent, *Rotation of the Andromeda Nebula from a Spectroscopic Survey of Emission Regions*, The Astrophysical Journal **159**, 379 (1970), doi:10.1086/150317.

[9] R. L. Workman *et al.*, *Review of Particle Physics*, PTEP **2022**, 483 (2022), doi:10.1093/ptep/ptac097.

[10] G. Hinshaw, J. L. Weiland, R. S. Hill, N. Odegard, D. Larson, C. L. Bennett, J. Dunkley, B. Gold, M. R. Greason, N. Jarosik, E. Komatsu, M. R. Nolta *et al.*, *FIVE-YEAR WILKINSON MICROWAVE ANISOTROPY PROBE* OBSERVATIONS: DATA PROCESSING, SKY MAPS, AND BASIC RESULTS*, The Astrophysical Journal Supplement Series **180**, 225 (2009), doi:10.1088/0067-0049/180/2/225, https://doi.org/10.1088%2F0067-0049%2F180%2F2%2F225.

[11] T. Abbott, M. Aguena, A. Alarcon, S. Allam, O. Alves, A. Amon, F. Andrade-Oliveira, J. Annis, S. Avila, D. Bacon, E. Baxter, K. Bechtol *et al.*, *Dark Energy Survey Year 3 results: Cosmological constraints from galaxy clustering and weak lensing*, Physical Review D **105** (2022), doi:10.1103/physrevd.105.023520, `https://doi.org/10.1103%2Fphysrevd.105.023520`.

[12] A. Porredon, M. Crocce, J. Elvin-Poole, R. Cawthon, G. Giannini, J. De Vicente, A. C. Rosell, I. Ferrero, E. Krause, X. Fang, J. Prat, M. Rodriguez-Monroy *et al.*, *Dark Energy Survey Year 3 results: Cosmological constraints from galaxy clustering and galaxy-galaxy lensing using the MagLim lens sample*, doi:10.48550/ARXIV.2105.13546 (2021).

[13] D. Clowe, M. Bradač, A. H. Gonzalez, M. Markevitch, S. W. Randall, C. Jones and D. Zaritsky, *A Direct Empirical Proof of the Existence of Dark Matter*, The Astrophysical Journal **648**, L109 (2006), doi:10.1086/508162, `https://doi.org/10.1086%2F508162`.

[14] and N. Aghanim, Y. Akrami, M. Ashdown, J. Aumont, C. Baccigalupi, M. Ballardini, A. J. Banday, R. B. Barreiro, N. Bartolo, S. Basak, R. Battye, K. Benabed *et al.*, *Planck 2018 results - VI. Cosmological parameters*, A&A **641**, A6 (2020), doi:10.1051/0004-6361/201833910, `https://doi.org/10.1051%2F0004-6361%2F201833910`.

[15] W. J. Percival, S. Cole, D. J. Eisenstein, R. C. Nichol, J. A. Peacock, A. C. Pope and A. S. Szalay, *Measuring the Baryon Acoustic Oscillation scale using the Sloan Digital Sky Survey and 2dF Galaxy Redshift Survey*, Monthly Notices of the Royal Astronomical Society **381**, 1053 (2007), doi:10.1111/j.1365-2966.2007.12268.x, `https://doi.org/10.1111%2Fj.1365-2966.2007.12268.x`.

[16] J. A. Peacock, S. Cole, P. Norberg, C. M. Baugh, J. Bland-Hawthorn, T. Bridges, R. D. Cannon, M. Colless, C. Collins, W. Couch, G. Dalton, K. Deeley *et al.*, *A measurement of the cosmological mass density from clustering in the 2dF Galaxy Redshift Survey*, Nature **410**, 169 (2001), doi:10.1038/35065528, `https://doi.org/10.1038%2F35065528`.

[17] M. Viel, J. S. Bolton and M. G. Haehnelt, *Cosmological and astrophysical constraints from the Lyman α forest flux probability distribution function*, Monthly Notices of the Royal Astronomical Society: Letters **399**, L39 (2009), doi:10.1111/j.1745-3933.2009.00720.x, `https://doi.org/10.1111%2Fj.1745-3933.2009.00720.x`.

[18] *Standard Model Summary Plots February 2022*, Tech. rep., CERN, Geneva, Available at `https://atlas.web.cern.ch/Atlas/GROUPS/PHYSICS/PUBNOTES/ATL-PHYS-PUB-2022-009` (2022).

[19] *SUSY Summary Plots March 2022*, Tech. rep., CERN, Geneva, Available at `https://atlas.web.cern.ch/Atlas/GROUPS/PHYSICS/PUBNOTES/ATL-PHYS-PUB-2022-013` (2022).

[20] *Summary Plots for Heavy Particle Searches and Long-lived Particle Searches - July 2022*, Tech. rep., CERN, Geneva, Available at `https://atlas.web.cern.ch/Atlas/GROUPS/PHYSICS/PUBNOTES/ATL-PHYS-PUB-2022-034` (2022).

[21] *Dark matter summary plots for s-channel, 2HDM+a and Dark Higgs models*, Tech. rep., CERN, Geneva, Available at `https://atlas.web.cern.ch/Atlas/GROUPS/PHYSICS/PUBNOTES/ATL-PHYS-PUB-2022-036` (2022).

[22] *Summary Plots from ATLAS Searches for Pair-Produced Leptoquarks*, Tech. rep., CERN, Geneva, Available at `https://atlas.web.cern.ch/Atlas/GROUPS/PHYSICS/PUBNOTES/ATL-PHYS-PUB-2022-012` (2022).

[23] *Summary plots for beyond Standard Model Higgs boson benchmarks for direct and indirect searches*, Tech. rep., CERN, Geneva, Available at `https://atlas.web.cern.ch/Atlas/GROUPS/PHYSICS/PUBNOTES/ATL-PHYS-PUB-2022-043` (2022).

[24] *Summary plot for the interpretation of heavy Higgs boson searches in the Georgi-Machacek model*, Tech. rep., CERN, Geneva, Available at `https://atlas.web.cern.ch/Atlas/GROUPS/PHYSICS/PUBNOTES/ATL-PHYS-PUB-2022-008` (2022).

[25] *Summary of Diboson Resonance Searches from the ATLAS Experiment*, Tech. rep., CERN, Geneva, Available at `https://atlas.web.cern.ch/Atlas/GROUPS/PHYSICS/PUBNOTES/ATL-PHYS-PUB-2021-018` (2021).

[26] *Summary of Exotic Higgs Boson Decays from the ATLAS Experiment*, Tech. rep., CERN, Geneva, Available at `https://atlas.web.cern.ch/Atlas/GROUPS/PHYSICS/PUBNOTES/ATL-PHYS-PUB-2021-008` (2021).

[27] *Summaries of CMS Cross section measurements*, Tech. rep., CERN, Geneva, Available at `https://twiki.cern.ch/twiki/bin/view/CMSPublic/PhysicsResultsCombined`. Accessed: 2022-12-3 (2022).

[28] *CMS Exotica Summary plots for 13 TeV data*, Tech. rep., CERN, Geneva, Available at `https://twiki.cern.ch/twiki/bin/view/CMSPublic/SummaryPlotsEXO13TeV`. Accessed: 2022-12-3 (2022).

[29] *CMS Beyond SM particles decaying 2(to) Higgs, top and Gauge bosons (B2G) Public Physics Results*, Tech. rep., CERN, Geneva, Available at `https://twiki.cern.ch/twiki/bin/view/CMSPublic/PhysicsResultsB2G`. Accessed: 2022-12-3 (2022).

[30] *Combined measurements of Higgs boson production and decay using up to 139 fb^{-1} of proton-proton collision data at $\sqrt{s} = 13$ TeV collected with the ATLAS experiment*, Tech. rep., CERN, Geneva, All figures including auxiliary figures are available at `https://atlas.web.cern.ch/Atlas/GROUPS/PHYSICS/CONFNOTES/ATLAS-CONF-2021-053/` (2021).

[31] *Combined effective field theory interpretation of $H \to WW^*$ and WW measurements using ATLAS data*, Tech. rep., CERN, Geneva, All figures including auxiliary figures are available at `https://atlas.web.cern.ch/Atlas/GROUPS/PHYSICS/PUBNOTES/ATL-PHYS-PUB-2021-010` (2021).

[32] *Combined effective field theory interpretation of Higgs boson and weak boson production and decay with ATLAS data and electroweak precision observables*, Tech. rep., CERN, Geneva, All figures including auxiliary figures are available at `https://atlas.web.cern.ch/Atlas/GROUPS/PHYSICS/PUBNOTES/ATL-PHYS-PUB-2022-037` (2022).

[33] A. M. Sirunyan, , A. Tumasyan, W. Adam, T. Bergauer, M. Dragicevic, A. E. D. Valle, R. Frühwirth, M. Jeitler, N. Krammer, L. Lechner, D. Liko *et al.*, *Search for new physics in top quark production with additional leptons in proton-proton collisions at $$ \sqrt{s} $$ = 13 TeV using effective field theory*, Journal of High Energy Physics **2021** (2021), doi:10.1007/jhep03(2021)095, `https://doi.org/10.1007%2Fjhep03%282021%29095`.

[34] CMS Collaboration, *Search for new physics using effective field theory in 13 TeV pp collision events that contain a top quark pair and a boosted Z or Higgs boson*, doi:10.48550/ARXIV.2208.12837 (2022).

[35] *LHC long term schedule*, https://lhc-commissioning.web.cern.ch/schedule/LHC-long-term.htm, Accessed: 2022-12-5.

[36] A. Biekötter, T. Corbett and T. Plehn, *The Gauge-Higgs Legacy of the LHC Run II*, SciPost Phys. **6**, 064 (2019), doi:10.21468/SciPostPhys.6.6.064, arXiv:1812.07587.

[37] A. Butter, O. J. P. Eboli, J. Gonzalez-Fraile, M. C. Gonzalez-Garcia, T. Plehn and M. Rauch, *The Gauge-Higgs Legacy of the LHC Run I*, JHEP **07**, 152 (2016), doi:10.1007/JHEP07(2016)152, arXiv:1604.03105.

[38] I. Brivio, S. Bruggisser, F. Maltoni, R. Moutafis, T. Plehn, E. Vryonidou, S. Westhoff and C. Zhang, *O new physics, where art thou? A global search in the top sector*, JHEP **02**, 131 (2020), doi:10.1007/JHEP02(2020)131, arXiv:1910.03606.

[39] J. J. Ethier, G. Magni, F. Maltoni, L. Mantani, E. R. Nocera, J. Rojo, E. Slade, E. Vryonidou and C. Zhang, *Combined SMEFT interpretation of Higgs, diboson, and top quark data from the LHC*, JHEP **11**, 089 (2021), doi:10.1007/JHEP11(2021)089, arXiv:2105.00006.

[40] J. Ellis, M. Madigan, K. Mimasu, V. Sanz and T. You, *Top, Higgs, Diboson and Electroweak Fit to the Standard Model Effective Field Theory*, JHEP **04**, 279 (2021), doi:10.1007/JHEP04(2021)279, arXiv:2012.02779.

[41] S. Dawson, S. Homiller and S. D. Lane, *Putting standard model EFT fits to work*, Phys. Rev. D **102**, 055012 (2020), doi:10.1103/PhysRevD.102.055012, arXiv:2007.01296.

[42] E. da Silva Almeida, A. Alves, N. Rosa Agostinho, O. J. P. Éboli and M. C. Gonzalez-Garcia, *Electroweak Sector Under Scrutiny: A Combined Analysis of LHC and Electroweak Precision Data*, Phys. Rev. **D99**, 033001 (2019), doi:10.1103/PhysRevD.99.033001, arXiv:1812.01009.

[43] E. d. S. Almeida, A. Alves, O. J. P. Éboli and M. C. Gonzalez-Garcia, *Electroweak legacy of the LHC run II*, Phys. Rev. D **105**, 013006 (2022), doi:10.1103/PhysRevD.105.013006, arXiv:2108.04828.

[44] S. Bißmann, C. Grunwald, G. Hiller and K. Kröninger, *Top and beauty synergies in SMEFT-fits at present and future colliders, journal = Journal of High Energy Physics* **2021** (2021), doi:10.1007/jhep06(2021)010, https://doi.org/10.1007%2Fjhep06%282021%29010, arXiv:2012.10456.

[45] S. Brown, A. Buckley, C. Englert, J. Ferrando, P. Galler, D. J. Miller, L. Moore, M. Russell, C. White and N. Warrack, *TopFitter: Fitting top-quark Wilson Coefficients to Run II data*, PoS **ICHEP2018**, 293 (2019), doi:10.22323/1.340.0293, arXiv:1901.03164.

[46] J. de Blas, M. Pierini, L. Reina and L. Silvestrini, *Impact of the recent measurements of the top-quark and W-boson masses on electroweak precision fits*, doi:10.48550/ARXIV.2204.04204 (2022).

[47] S. Kraml, T. Q. Loc, D. T. Nhung and L. D. Ninh, *Constraining new physics from Higgs measurements with Lilith: update to LHC Run 2 results*, SciPost Phys. **7**, 052 (2019), doi:10.21468/SciPostPhys.7.4.052, arXiv:1908.03952.

[48] S. van Beek, E. R. Nocera, J. Rojo and E. Slade, *Constraining the SMEFT with Bayesian reweighting*, SciPost Phys. **7**, 070 (2019), doi:10.21468/SciPostPhys.7.5.070, arXiv:1906.05296.

[49] N. P. Hartland, F. Maltoni, E. R. Nocera, J. Rojo, E. Slade, E. Vryonidou and C. Zhang, *A Monte Carlo global analysis of the Standard Model Effective Field Theory: the top quark sector*, JHEP **04**, 100 (2019), doi:10.1007/JHEP04(2019)100, arXiv:1901.05965.

[50] T. Corbett, O. J. P. Eboli, D. Goncalves, J. Gonzalez-Fraile, T. Plehn and M. Rauch, *The Higgs Legacy of the LHC Run I*, JHEP **08**, 156 (2015), doi:10.1007/JHEP08(2015)156, arXiv:1505.05516.

[51] T. Appelquist and J. Carazzone, *Infrared Singularities and Massive Fields*, Phys. Rev. D **11**, 2856 (1975), doi:10.1103/PhysRevD.11.2856.

[52] J. F. Donoghue, *General relativity as an effective field theory: The leading quantum corrections*, Physical Review D **50**, 3874 (1994), doi:10.1103/physrevd.50.3874, `https://doi.org/10.1103%2Fphysrevd.50.3874`, arXiv:gr-qc/9405057.

[53] J. F. Donoghue, *Introduction to the Effective Field Theory Description of Gravity*, doi:10.48550/ARXIV.GR-QC/9512024 (1995).

[54] C. P. Burgess, *Quantum Gravity in Everyday Life: General Relativity as an Effective Field Theory*, Living Reviews in Relativity **7** (2004), doi:10.12942/lrr-2004-5, `https://doi.org/10.12942%2Flrr-2004-5`, arXiv:gr-qc/0311082.

[55] J. F. Donoghue, *The effective field theory treatment of quantum gravity*, In *AIP Conference Proceedings*. AIP, doi:10.1063/1.4756964 (2012), arXiv:1209.3511.

[56] M. Ruhdorfer, J. Serra and A. Weiler, *Effective field theory of gravity to all orders*, Journal of High Energy Physics **2020** (2020), doi:10.1007/jhep05(2020)083, `https://doi.org/10.1007%2Fjhep05%282020%29083`, arXiv:1908.08050.

[57] D. T. Son, *Low-Energy Quantum Effective Action for Relativistic Superfluids*, doi:10.48550/ARXIV.HEP-PH/0204199 (2002).

[58] A. Nicolis, *Low-energy effective field theory for finite-temperature relativistic superfluids*, doi:10.48550/ARXIV.1108.2513 (2011).

[59] A. Nicolis, R. Penco, F. Piazza and R. Rattazzi, *Zoology of condensed matter: Framids, ordinary stuff, extra-ordinary stuff*, doi:10.48550/ARXIV.1501.03845 (2015).

[60] B. Horn, A. Nicolis and R. Penco, *Effective string theory for vortex lines in fluids and superfluids*, doi:10.48550/ARXIV.1507.05635 (2015).

[61] S. Moroz, C. Hoyos, C. Benzoni and D. T. Son, *Effective field theory of a vortex lattice in a bosonic superfluid*, SciPost Physics **5** (2018), doi:10.21468/scipostphys.5.4.039, `https://doi.org/10.21468%2Fscipostphys.5.4.039`, arXiv:1803.10934.

[62] F. Acanfora, A. Esposito and A. D. Polosa, *Sub-GeV dark matter in superfluid He-4: an effective theory approach*, The European Physical Journal C **79** (2019), doi:10.1140/epjc/s10052-019-7057-0, `https://doi.org/10.1140%2Fepjc%2Fs10052-019-7057-0`, arXiv:1902.02361.

[63] A. Esposito, R. Krichevsky and A. Nicolis, *Gravitational Mass Carried by Sound Waves*, Physical Review Letters **122** (2019), doi:10.1103/physrevlett.122.084501, `https://doi.org/10.1103%2Fphysrevlett.122.084501`, arXiv:1807.08771.

[64] A. Caputo, A. Esposito and A. D. Polosa, *Sub-MeV dark matter and the Goldstone modes of superfluid helium*, Physical Review D **100** (2019), doi:10.1103/physrevd.100.116007, `https://doi.org/10.1103%2Fphysrevd.100.116007`, arXiv:1907.10635.

[65] A. Caputo, A. Esposito, E. Geoffray, A. D. Polosa and S. Sun, *Dark matter, dark photon and superfluid He-4 from effective field theory*, Physics Letters B **802**, 135258 (2020), doi:10.1016/j.physletb.2020.135258, `https://doi.org/10.1016%2Fj.physletb.2020.135258`, 1911.04511.

[66] H. Leutwyler, *Phonons as Goldstone Bosons* (1996), doi:10.48550/ARXIV.HEP-PH/9609466, `https://arxiv.org/abs/hep-ph/9609466`.

[67] L. Alberte, M. Baggioli, V. C. Castillo and O. Pujolàs, *Elasticity bounds from effective field theory*, Physical Review D **100** (2019), doi:10.1103/physrevd.100.065015, `https://doi.org/10.1103%2Fphysrevd.100.065015`, arXiv:1807.07474.

[68] S. Golkar, M. M. Roberts and D. T. Son, *Effective field theory of relativistic quantum hall systems*, Journal of High Energy Physics **2014** (2014), doi:10.1007/jhep12(2014)138, `https://doi.org/10.1007%2Fjhep12%282014%29138`, arXiv:1403.4279.

[69] M. Crossley, P. Glorioso and H. Liu, *Effective field theory of dissipative fluids*, doi:10.48550/ARXIV.1511.03646 (2015).

[70] A. Nicolis and R. Penco, *Mutual interactions of phonons, rotons, and gravity*, Physical Review B **97** (2018), doi:10.1103/physrevb.97.134516, `https://doi.org/10.1103%2Fphysrevb.97.134516`, arXiv:1705.08914.

[71] I. Z. Rothstein and P. Shrivastava, *Symmetry obstruction to Fermi liquid behavior in the unitary limit*, Physical Review B **99** (2019), doi:10.1103/physrevb.99.035101, `https://doi.org/10.1103%2Fphysrevb.99.035101`, arXiv:1712.07797.

[72] G. Buchalla, A. J. Buras and M. E. Lautenbacher, *Weak decays beyond leading logarithms*, Rev. Mod. Phys. **68**, 1125 (1996), doi:10.1103/RevModPhys.68.1125, arXiv:hep-ph/9512380.

[73] J. Aebischer, M. Fael, C. Greub and J. Virto, *B physics Beyond the Standard Model at One Loop: Complete Renormalization Group Evolution below the Electroweak Scale*, JHEP **09**, 158 (2017), doi:10.1007/JHEP09(2017)158, arXiv:1704.06639.

[74] E. E. Jenkins, A. V. Manohar and P. Stoffer, *Low-Energy Effective Field Theory below the Electroweak Scale: Operators and Matching*, JHEP **03**, 016 (2018), doi:10.1007/JHEP03(2018)016, arXiv:1709.04486.

[75] W. Buchmuller and D. Wyler, *Effective Lagrangian Analysis of New Interactions and Flavor Conservation*, Nucl. Phys. B **268**, 621 (1986), doi:10.1016/0550-3213(86)90262-2.

[76] B. Grzadkowski, M. Iskrzynski, M. Misiak and J. Rosiek, *Dimension-Six Terms in the Standard Model Lagrangian*, JHEP **10**, 085 (2010), doi:10.1007/JHEP10(2010)085, arXiv:1008.4884.

[77] F. Feruglio, *The Chiral approach to the electroweak interactions*, Int. J. Mod. Phys. A **8**, 4937 (1993), doi:10.1142/S0217751X93001946, arXiv:hep-ph/9301281.

[78] B. Grinstein and M. Trott, *A Higgs-Higgs bound state due to new physics at a TeV*, Phys. Rev. D **76**, 073002 (2007), doi:10.1103/PhysRevD.76.073002, arXiv:0704.1505.

[79] G. Buchalla, O. Catà and C. Krause, *Complete Electroweak Chiral Lagrangian with a Light Higgs at NLO*, Nucl. Phys. B **880**, 552 (2014), doi:10.1016/j.nuclphysb.2014.01.018, [Erratum: Nucl.Phys.B 913, 475–478 (2016)], arXiv:1307.5017.

[80] I. Brivio, T. Corbett, O. J. P. Éboli, M. B. Gavela, J. Gonzalez-Fraile, M. C. Gonzalez-Garcia, L. Merlo and S. Rigolin, *Disentangling a dynamical Higgs*, JHEP **03**, 024 (2014), doi:10.1007/JHEP03(2014)024, arXiv:1311.1823.

[81] J. C. ROMÃO and J. P. SILVA, *A RESOURCE FOR SIGNS AND FEYNMAN DIAGRAMS OF THE STANDARD MODEL*, International Journal of Modern Physics A **27**, 1230025 (2012), doi:10.1142/s0217751x12300256, `https://doi.org/10.1142%2Fs0217751x12300256`, arXiv:1209.6213.

[82] S. Weinberg, *Varieties of Baryon and Lepton Nonconservation*, Phys. Rev. D **22**, 1694 (1980), doi:10.1103/PhysRevD.22.1694.

[83] R. Alonso, E. E. Jenkins, A. V. Manohar and M. Trott, *Renormalization Group Evolution of the Standard Model Dimension Six Operators III: Gauge Coupling Dependence and Phenomenology*, JHEP **04**, 159 (2014), doi:10.1007/JHEP04(2014)159, arXiv:1312.2014.

[84] L. Lehman, *Extending the standard model effective field theory with the complete set of dimension-7 operators*, Physical Review D **90** (2014), doi:10.1103/physrevd.90.125023, `https://doi.org/10.1103%2Fphysrevd.90.125023`, arXiv:1410.4193.

[85] B. Henning, X. Lu, T. Melia and H. Murayama, *2, 84, 30, 993, 560, 15456, 11962, 261485, …: Higher dimension operators in the SM EFT*, JHEP **08**, 016 (2017), doi:10.1007/JHEP08(2017)016, [Erratum: JHEP 09, 019 (2019)], arXiv:1512.03433.

[86] C. W. Murphy, *Dimension-8 operators in the Standard Model Effective Field Theory*, Journal of High Energy Physics **2020** (2020), doi:10.1007/jhep10(2020)174, `https://doi.org/10.1007%2Fjhep10%282020%29174`, arXiv:2005.00059.

[87] H.-L. Li, Z. Ren, J. Shu, M.-L. Xiao, J.-H. Yu and Y.-H. Zheng, *Complete set of dimension-eight operators in the standard model effective field theory*, Physical Review D **104** (2021), doi:10.1103/physrevd.104.015026, `https://doi.org/10.1103%2Fphysrevd.104.015026`, arXiv:2005.00008.

[88] B. Sekhar Chivukula and H. Georgi, *Composite-technicolor standard model*, Physics Letters B **188**, 99 (1987), doi:https://doi.org/10.1016/0370-2693(87)90713-1, `https://www.sciencedirect.com/science/article/pii/0370269387907131`.

[89] L. J. Hall and L. Randall, *Weak-scale effective supersymmetry*, Phys. Rev. Lett. **65**, 2939 (1990), doi:10.1103/PhysRevLett.65.2939, `https://link.aps.org/doi/10.1103/PhysRevLett.65.2939`.

[90] G. D'Ambrosio, G. Giudice, G. Isidori and A. Strumia, *Minimal flavour violation: an effective field theory approach*, Nuclear Physics B **645**, 155 (2002), doi:https://doi.org/10.1016/S0550-3213(02)00836-2, `https://www.sciencedirect.com/science/article/pii/S0550321302008362`.

[91] S. Brass, C. Fleper, W. Kilian, J. Reuter and M. Sekulla, *Transversal Modes and Higgs Bosons in Electroweak Vector-Boson Scattering at the LHC*, Eur. Phys. J. C **78**, 931 (2018), doi:10.1140/epjc/s10052-018-6398-4, arXiv:1807.02512.

[92] S. Dawson, S. Homiller and M. Sullivan, *Impact of dimension-eight SMEFT contributions: A case study*, Phys. Rev. D **104**, 115013 (2021), doi:10.1103/PhysRevD.104.115013, arXiv:2110.06929.

[93] S. Dawson, D. Fontes, S. Homiller and M. Sullivan, *Beyond 6: the role of dimension-8 operators in an EFT for the 2HDM* (2022), doi:10.48550/ARXIV.2205.01561, arXiv:2205.01561.

[94] A. Biekötter, J. Brehmer and T. Plehn, *Extending the limits of Higgs effective theory*, Phys. Rev. **D94**, 055032 (2016), doi:10.1103/PhysRevD.94.055032, arXiv:1602.05202.

[95] Anisha, S. Das Bakshi, J. Chakrabortty and S. K. Patra, *Connecting electroweak-scale observables to BSM physics through EFT and Bayesian statistics*, Phys. Rev. D **103**, 076007 (2021), doi:10.1103/PhysRevD.103.076007, arXiv:2010.04088.

[96] S. Das Bakshi, J. Chakrabortty and M. Spannowsky, *Classifying Standard Model Extensions Effectively with Precision Observables*, Phys. Rev. D **103**, 056019 (2021), doi:10.1103/PhysRevD.103.056019, arXiv:2012.03839.

[97] S. D. Bakshi, J. Chakrabortty, S. Prakash, S. U. Rahaman and M. Spannowsky, *EFT Diagrammatica: UV Roots of the CP-conserving SMEFT*, doi:10.48550/ARXIV.2103.11593 (2021), arXiv:2103.11593.

[98] R. Cepedello, F. Esser, M. Hirsch and V. Sanz, *Mapping the SMEFT to discoverable models* (2022), doi:10.48550/ARXIV.2207.13714, arXiv:2207.13714.

[99] K. Hagiwara, S. Ishihara, R. Szalapski and D. Zeppenfeld, *Low-energy effects of new interactions in the electroweak boson sector*, Phys. Rev. D **48**, 2182 (1993), doi:10.1103/PhysRevD.48.2182.

[100] T. Corbett, O. J. P. Eboli, J. Gonzalez-Fraile and M. C. Gonzalez-Garcia, *Robust Determination of the Higgs Couplings: Power to the Data*, Phys. Rev. D **87**, 015022 (2013), doi:10.1103/PhysRevD.87.015022, arXiv:1211.4580.

[101] S. Di Vita, C. Grojean, G. Panico, M. Riembau and T. Vantalon, *A global view on the Higgs self-coupling*, JHEP **09**, 069 (2017), doi:10.1007/JHEP09(2017)069, arXiv:1704.01953.

[102] D. Gonçalves, T. Han, F. Kling, T. Plehn and M. Takeuchi, *Higgs boson pair production at future hadron colliders: From kinematics to dynamics*, Phys. Rev. D **97**, 113004 (2018), doi:10.1103/PhysRevD.97.113004, arXiv:1802.04319.

[103] J. Chang, K. Cheung, J. S. Lee, C.-T. Lu and J. Park, *Higgs-boson-pair production $H(\to b\bar{b})H(\to \gamma\gamma)$ from gluon fusion at the HL-LHC and HL-100 TeV hadron collider*, Phys. Rev. D **100**, 096001 (2019), doi:10.1103/PhysRevD.100.096001, arXiv:1804.07130.

[104] A. Biekötter, D. Gonçalves, T. Plehn, M. Takeuchi and D. Zerwas, *The global Higgs picture at 27 TeV*, SciPost Phys. **6**, 024 (2019), doi:10.21468/SciPostPhys.6.2.024, arXiv:1811.08401.

[105] S. Borowka, C. Duhr, F. Maltoni, D. Pagani, A. Shivaji and X. Zhao, *Probing the scalar potential via double Higgs boson production at hadron colliders*, JHEP **04**, 016 (2019), doi:10.1007/JHEP04(2019)016, arXiv:1811.12366.

[106] F. Krauss, S. Kuttimalai and T. Plehn, *LHC multijet events as a probe for anomalous dimension-six gluon interactions*, Phys. Rev. D **95**, 035024 (2017), doi:10.1103/PhysRevD.95.035024, arXiv:1611.00767.

[107] J. Ellis, C. W. Murphy, V. Sanz and T. You, *Updated Global SMEFT Fit to Higgs, Diboson and Electroweak Data*, JHEP **06**, 146 (2018), doi:10.1007/JHEP06(2018)146, arXiv:1803.03252.

[108] Z. Zhang, *Time to Go Beyond Triple-Gauge-Boson-Coupling Interpretation of W Pair Production*, Phys. Rev. Lett. **118**, 011803 (2017), doi:10.1103/PhysRevLett.118.011803, arXiv:1610.01618.

[109] T. Corbett, O. J. P. Éboli and M. C. Gonzalez-Garcia, *Unitarity Constraints on Dimension-six Operators II: Including Fermionic Operators*, Phys. Rev. D **96**, 035006 (2017), doi:10.1103/PhysRevD.96.035006, arXiv:1705.09294.

[110] J. Baglio, S. Dawson and I. M. Lewis, *An NLO QCD effective field theory analysis of W^+W^- production at the LHC including fermionic operators*, Phys. Rev. D **96**, 073003 (2017), doi:10.1103/PhysRevD.96.073003, arXiv:1708.03332.

[111] J. Baglio, S. Dawson and I. M. Lewis, *NLO effects in EFT fits to W^+W^- production at the LHC*, Phys. Rev. D **99**, 035029 (2019), doi:10.1103/PhysRevD.99.035029, arXiv:1812.00214.

[112] A. Alves, N. Rosa-Agostinho, O. J. P. Éboli and M. C. Gonzalez-Garcia, *Effect of Fermionic Operators on the Gauge Legacy of the LHC Run I*, Phys. Rev. D **98**, 013006 (2018), doi:10.1103/PhysRevD.98.013006, arXiv:1805.11108.

[113] S. Dawson and A. Ismail, *Standard model EFT corrections to Z boson decays*, Phys. Rev. D **98**, 093003 (2018), doi:10.1103/PhysRevD.98.093003, arXiv:1808.05948.

[114] V. Cirigliano, J. Jenkins and M. Gonzalez-Alonso, *Semileptonic decays of light quarks beyond the Standard Model*, Nucl. Phys. B **830**, 95 (2010), doi:10.1016/j.nuclphysb.2009.12.020, arXiv:0908.1754.

[115] A. Falkowski, M. González-Alonso and K. Mimouni, *Compilation of low-energy constraints on 4-fermion operators in the SMEFT*, JHEP **08**, 123 (2017), doi:10.1007/JHEP08(2017)123, arXiv:1706.03783.

[116] S. Alioli, V. Cirigliano, W. Dekens, J. de Vries and E. Mereghetti, *Right-handed charged currents in the era of the Large Hadron Collider*, JHEP **05**, 086 (2017), doi:10.1007/JHEP05(2017)086, arXiv:1703.04751.

[117] F. Maltoni, E. Vryonidou and C. Zhang, *Higgs production in association with a top-antitop pair in the Standard Model Effective Field Theory at NLO in QCD*, JHEP **10**, 123 (2016), doi:10.1007/JHEP10(2016)123, arXiv:1607.05330.

[118] M. Grazzini, A. Ilnicka, M. Spira and M. Wiesemann, *Modeling BSM effects on the Higgs transverse-momentum spectrum in an EFT approach*, JHEP **03**, 115 (2017), doi:10.1007/JHEP03(2017)115, arXiv:1612.00283.

[119] N. Deutschmann, C. Duhr, F. Maltoni and E. Vryonidou, *Gluon-fusion Higgs production in the Standard Model Effective Field Theory*, JHEP **12**, 063 (2017), doi:10.1007/JHEP12(2017)063, [Erratum: JHEP 02, 159 (2018)], arXiv:1708.00460.

[120] R. Lafaye, T. Plehn and D. Zerwas, *SFITTER: SUSY parameter analysis at LHC and LC* (2004), doi:10.48550/ARXIV.HEP-PH/0404282, arXiv:hep-ph/0404282.

[121] R. Lafaye, T. Plehn, M. Rauch and D. Zerwas, *Measuring Supersymmetry*, Eur. Phys. J. C **54**, 617 (2008), doi:10.1140/epjc/s10052-008-0548-z, arXiv:0709.3985.

[122] C. Adam, J.-L. Kneur, R. Lafaye, T. Plehn, M. Rauch and D. Zerwas, *Measuring unification*, The European Physical Journal C **71** (2011), doi:10.1140/epjc/s10052-010-1520-2, https://doi.org/10.1140%2Fepjc%2Fs10052-010-1520-2, arXiv:1007.2190.

[123] E. Turlay, R. Lafaye, T. Plehn, M. Rauch and D. Zerwas, *Measuring supersymmetry with heavy scalars*, Journal of Physics G: Nuclear and Particle Physics **38**, 035003 (2011), doi:10.1088/0954-3899/38/3/035003, https://doi.org/10.1088%2F0954-3899%2F38%2F3%2F035003, arXiv:1011.0759.

[124] D. López-Val, T. Plehn and M. Rauch, *Measuring extended Higgs sectors as a consistent free couplings model*, JHEP **10**, 134 (2013), doi:10.1007/JHEP10(2013)134, arXiv:1308.1979.

[125] A. Butter, T. Plehn, M. Rauch, D. Zerwas, S. Henrot-Versillé and R. Lafaye, *Linking the Galactic Center excess to invisible Higgs boson decays in the NMSSM*, Physical Review D **93** (2016), doi:10.1103/physrevd.93.015011, https://doi.org/10.1103%2Fphysrevd.93.015011, arXiv:1507.02288.

[126] S. Henrot-Versillé, R. Lafaye, T. Plehn, M. Rauch, D. Zerwas, S. Plaszczynski, B. R. d'Orfeuil and M. Spinelli, *Constraining supersymmetry using the relic density and the Higgs boson*, Physical Review D **89** (2014), doi:10.1103/physrevd.89.055017, https://doi.org/10.1103%2Fphysrevd.89.055017, arXiv:1309.6958.

[127] R. Lafaye, T. Plehn, M. Rauch, D. Zerwas and M. Duhrssen, *Measuring the Higgs Sector*, JHEP **08**, 009 (2009), doi:10.1088/1126-6708/2009/08/009, arXiv:0904.3866.

[128] M. Klute, R. Lafaye, T. Plehn, M. Rauch and D. Zerwas, *Measuring Higgs Couplings from LHC Data*, Phys. Rev. Lett. **109**, 101801 (2012), doi:10.1103/PhysRevLett.109.101801, arXiv:1205.2699.

[129] M. Bauer, A. Butter, J. Gonzalez-Fraile, T. Plehn and M. Rauch, *Learning from a Higgs-like scalar resonance*, Physical Review D **95** (2017), doi:10.1103/physrevd.95.055011, https://doi.org/10.1103%2Fphysrevd.95.055011, arXiv:1607.04562.

[130] A. Butter, *Global Fits for New Physics at the LHC and Beyond*, Ph.D. thesis, U. Heidelberg (main), doi:10.11588/heidok.00023710 (2017).

[131] A. Biekötter, *Know its limits: A global view on Higgs couplings at the LHC*, Ph.D. thesis, Heidelberg U., doi:10.11588/heidok.00026907 (2019).

[132] A. Hocker, H. Lacker, S. Laplace and F. Le Diberder, *A New approach to a global fit of the CKM matrix*, Eur. Phys. J. C **21**, 225 (2001), doi:10.1007/s100520100729, arXiv:hep-ph/0104062.

[133] J. Neyman and E. S. Pearson, *IX. On the problem of the most efficient tests of statistical hypotheses*, Physical Review D **231** (1933), doi:http://doi.org/10.1098/rsta.1933.0009.

[134] A. Gelman, J. Carlin, H. Stern, D. Dunson, A. Vehtari and D. Rubin, *Bayesian Data Analysis*, Chapman and Hall/CRC, third edn., ISBN 9780429113079, doi:10.1201/b16018 (2013).

[135] S. S. Wilks, *The Large-Sample Distribution of the Likelihood Ratio for Testing Composite Hypotheses*, The Annals of Mathematical Statistics **9**, 60 (1938), doi:10.1214/aoms/1177732360, https://doi.org/10.1214/aoms/1177732360.

[136] *Prospects for $H \to c\bar{c}$ using Charm Tagging with the ATLAS Experiment at the HL-LHC*, Tech. rep., CERN, Geneva, All figures including auxiliary figures are available at https://atlas.web.cern.ch/Atlas/GROUPS/PHYSICS/PUBNOTES/ATL-PHYS-PUB-2018-016 (2018).

[137] *Precision electroweak measurements on the Z resonance*, Physics Reports **427**, 257 (2006), doi:10.1016/j.physrep.2005.12.006, https://doi.org/10.1016%2Fj.physrep.2005.12.006, arXiv:0509008.

[138] M. Tanabashi, K. Hagiwara, K. Hikasa, K. Nakamura, Y. Sumino, F. Takahashi, J. Tanaka, K. Agashe, G. Aielli, C. Amsler, M. Antonelli, D. M. Asner *et al.*, *Review of Particle Physics*, Phys. Rev. D **98**, 030001 (2018), doi:10.1103/PhysRevD.98.030001, https://link.aps.org/doi/10.1103/PhysRevD.98.030001.

[139] J. Alwall, R. Frederix, S. Frixione, V. Hirschi, F. Maltoni, O. Mattelaer, H. S. Shao, T. Stelzer, P. Torrielli and M. Zaro, *The automated computation of tree-level and next-to-leading order differential cross sections, and their matching to parton shower simulations*, JHEP **07**, 079 (2014), doi:10.1007/JHEP07(2014)079, arXiv:1405.0301.

[140] T. Sjöstrand, S. Ask, J. R. Christiansen, R. Corke, N. Desai, P. Ilten, S. Mrenna, S. Prestel, C. O. Rasmussen and P. Z. Skands, *An introduction to PYTHIA 8.2*, Comput. Phys. Commun. **191**, 159 (2015), doi:10.1016/j.cpc.2015.01.024, arXiv:1410.3012.

[141] M. Cacciari, G. P. Salam and G. Soyez, *FastJet User Manual*, Eur. Phys. J. C **72**, 1896 (2012), doi:10.1140/epjc/s10052-012-1896-2, arXiv:1111.6097.

[142] J. de Favereau, C. Delaere, P. Demin, A. Giammanco, V. Lemaître, A. Mertens and M. Selvaggi, *DELPHES 3, A modular framework for fast simulation of a generic collider experiment*, JHEP **02**, 057 (2014), doi:10.1007/JHEP02(2014)057, arXiv:1307.6346.

[143] M. Ciuchini, E. Franco, S. Mishima, M. Pierini, L. Reina and L. Silvestrini, *Update of the electroweak precision fit, interplay with Higgs-boson signal strengths and model-independent constraints on new physics* (2014), doi:10.48550/ARXIV.1410.6940, https://arxiv.org/abs/1410.6940.

[144] B. Henning, X. Lu and H. Murayama, *How to use the Standard Model effective field theory*, JHEP **01**, 023 (2016), doi:10.1007/JHEP01(2016)023, arXiv:1412.1837.

[145] B. Henning, X. Lu and H. Murayama, *One-loop Matching and Running with Covariant Derivative Expansion*, JHEP **01**, 123 (2018), doi:10.1007/JHEP01(2018)123, arXiv:1604.01019.

[146] A. Drozd, J. Ellis, J. Quevillon and T. You, *The Universal One-Loop Effective Action*, JHEP **03**, 180 (2016), doi:10.1007/JHEP03(2016)180, arXiv:1512.03003.

[147] S. A. R. Ellis, J. Quevillon, T. You and Z. Zhang, *Extending the Universal One-Loop Effective Action: Heavy-Light Coefficients*, JHEP **08**, 054 (2017), doi:10.1007/JHEP08(2017)054, arXiv:1706.07765.

[148] J. Fuentes-Martin, J. Portoles and P. Ruiz-Femenia, *Integrating out heavy particles with functional methods: a simplified framework*, JHEP **09**, 156 (2016), doi:10.1007/JHEP09(2016)156, arXiv:1607.02142.

[149] Z. Zhang, *Covariant diagrams for one-loop matching*, JHEP **05**, 152 (2017), doi:10.1007/JHEP05(2017)152, arXiv:1610.00710.

[150] S. Das Bakshi, J. Chakrabortty and S. K. Patra, *CoDEx: Wilson coefficient calculator connecting SMEFT to UV theory*, Eur. Phys. J. C **79**, 21 (2019), doi:10.1140/epjc/s10052-018-6444-2, arXiv:1808.04403.

[151] M. Krämer, B. Summ and A. Voigt, *Completing the scalar and fermionic Universal One-Loop Effective Action*, JHEP **01**, 079 (2020), doi:10.1007/JHEP01(2020)079, arXiv:1908.04798.

[152] S. A. R. Ellis, J. Quevillon, P. N. H. Vuong, T. You and Z. Zhang, *The fermionic universal one-loop effective action*, Journal of High Energy Physics **2020** (2020), doi:10.1007/jhep11(2020)078, `http://dx.doi.org/10.1007/JHEP11(2020)078`, arXiv:2006.16260.

[153] A. Angelescu and P. Huang, *Integrating out new fermions at one loop*, Journal of High Energy Physics **2021** (2021), doi:10.1007/jhep01(2021)049, `http://dx.doi.org/10.1007/JHEP01(2021)049`, arXiv:2006.16532.

[154] T. Cohen, X. Lu and Z. Zhang, *STrEAMlining EFT Matching*, SciPost Phys. **10**, 098 (2021), doi:10.21468/SciPostPhys.10.5.098, arXiv:2012.07851.

[155] J. Fuentes-Martin, M. König, J. Pagès, A. E. Thomsen and F. Wilsch, *SuperTracer: A Calculator of Functional Supertraces for One-Loop EFT Matching*, JHEP **04**, 281 (2021), doi:10.1007/JHEP04(2021)281, arXiv:2012.08506.

[156] S. Dittmaier, S. Schuhmacher and M. Stahlhofen, *Integrating out heavy fields in the path integral using the background-field method: general formalism*, The European Physical Journal C **81** (2021), doi:10.1140/epjc/s10052-021-09587-7, `http://dx.doi.org/10.1140/epjc/s10052-021-09587-7`, arXiv:2102.12020.

[157] D. Zhang and S. Zhou, *Complete one-loop matching of the type-I seesaw model onto the Standard Model effective field theory*, Journal of High Energy Physics **2021** (2021), doi:10.1007/jhep09(2021)163, `http://dx.doi.org/10.1007/JHEP09(2021)163`, arXiv:2107.12133.

[158] B. Summ, `github.com/BenjaminSumm/Triplet_Model_WCs` (2021).

[159] S. Dawson, C. Englert and T. Plehn, *Higgs Physics: It ain't over till it's over*, Phys. Rept. **816**, 1 (2019), doi:10.1016/j.physrep.2019.05.001, arXiv:1808.01324.

[160] I. Brivio and M. Trott, *The Standard Model as an Effective Field Theory*, Phys. Rept. **793**, 1 (2019), doi:10.1016/j.physrep.2018.11.002, arXiv:1706.08945.

[161] S. Iranipour and M. Ubiali, *A new generation of simultaneous fits to LHC data using deep learning*, JHEP **05**, 032 (2022), doi:10.1007/JHEP05(2022)032, arXiv:2201.07240.

[162] S. Bißmann, J. Erdmann, C. Grunwald, G. Hiller and K. Kröninger, *Correlating uncertainties in global analyses within SMEFT matters*, Phys. Rev. D **102**, 115019 (2020), doi:10.1103/PhysRevD.102.115019, arXiv:1912.06090.

[163] B. Dumont, S. Fichet and G. von Gersdorff, *A Bayesian view of the Higgs sector with higher dimensional operators*, JHEP **07**, 065 (2013), doi:10.1007/JHEP07(2013)065, arXiv:1304.3369.

[164] S. Fichet and G. Moreau, *Anatomy of the Higgs fits: a first guide to statistical treatments of the theoretical uncertainties*, Nucl. Phys. B **905**, 391 (2016), doi:10.1016/j.nuclphysb.2016.02.019, arXiv:1509.00472.

[165] J. De Blas *et al.*, `HEPfit`: *a code for the combination of indirect and direct constraints on high energy physics models*, Eur. Phys. J. C **80**, 456 (2020), doi:10.1140/epjc/s10052-020-7904-z, arXiv:1910.14012.

[166] J. de Blas, M. Ciuchini, E. Franco, A. Goncalves, S. Mishima, M. Pierini, L. Reina and L. Silvestrini, *Global analysis of electroweak data in the Standard Model*, Phys. Rev. D **106**, 033003 (2022), doi:10.1103/PhysRevD.106.033003, arXiv:2112.07274.

[167] J. Brehmer, S. Dawson, S. Homiller, F. Kling and T. Plehn, *Benchmarking simplified template cross sections in WH production*, JHEP **11**, 034 (2019), doi:10.1007/JHEP11(2019)034, arXiv:1908.06980.

[168] G. Aad *et al.*, *Search for heavy diboson resonances in semileptonic final states in pp collisions at $\sqrt{s} = 13$ TeV with the ATLAS detector*, Eur. Phys. J. C **80**, 1165 (2020), doi:10.1140/epjc/s10052-020-08554-y, arXiv:2004.14636.

[169] J. Brehmer, K. Cranmer, F. Kling and T. Plehn, *Better Higgs boson measurements through information geometry*, Phys. Rev. D **95**, 073002 (2017), doi:10.1103/PhysRevD.95.073002, arXiv:1612.05261.

[170] J. M. Campbell, R. K. Ellis and C. Williams, *Vector boson pair production at the LHC*, JHEP **07**, 018 (2011), doi:10.1007/JHEP07(2011)018, arXiv:1105.0020.

[171] ATLAS Collaboration, *Measurements of gluon fusion and vector-boson-fusion production of the Higgs boson in $H \to WW^* \to e\nu\mu\nu$ decays using pp collisions at $\sqrt{s} = 13$ TeV with the ATLAS detector* (2021), https://cds.cern.ch/record/2759651.

[172] CMS Collaboration, *Search for a heavy vector resonance decaying to a Z boson and a Higgs boson in proton-proton collisions at $\sqrt{s} = 13$ TeV*, Eur. Phys. J. C **81**, 688 (2021), doi:10.1140/epjc/s10052-021-09348-6, arXiv:2102.08198.

[173] ATLAS Collaboration, *Measurements and interpretations of Higgs-boson fiducial cross sections in the diphoton decay channel using 139 fb^{-}1 of pp collision data at $\sqrt{s}$ = 13 TeV with the ATLAS detector*, Tech. rep., All figures including auxiliary figures are available at `https://atlas.web.cern.ch/Atlas/GROUPS/PHYSICS/CONFNOTES/ATLAS-CONF-2019-029/` (2019).

[174] R. K. Ellis, I. Hinchliffe, M. Soldate and J. J. van der Bij, *Higgs Decay to tau+ tau-: A Possible Signature of Intermediate Mass Higgs Bosons at the SSC*, Nucl. Phys. B **297**, 221 (1988), doi:10.1016/0550-3213(88)90019-3.

[175] U. Baur and E. W. N. Glover, *Higgs Boson Production at Large Transverse Momentum in Hadronic Collisions*, Nucl. Phys. B **339**, 38 (1990), doi:10.1016/0550-3213(90)90532-I.

[176] A. Banfi, A. Martin and V. Sanz, *Probing top-partners in Higgs+jets*, JHEP **08**, 053 (2014), doi:10.1007/JHEP08(2014)053, arXiv:1308.4771.

[177] A. Azatov and A. Paul, *Probing Higgs couplings with high p_T Higgs production*, JHEP **01**, 014 (2014), doi:10.1007/JHEP01(2014)014, arXiv:1309.5273.

[178] R. V. Harlander and T. Neumann, *Probing the nature of the Higgs-gluon coupling*, Phys. Rev. D **88**, 074015 (2013), doi:10.1103/PhysRevD.88.074015, arXiv:1308.2225.

[179] C. Grojean, E. Salvioni, M. Schlaffer and A. Weiler, *Very boosted Higgs in gluon fusion*, JHEP **05**, 022 (2014), doi:10.1007/JHEP05(2014)022, arXiv:1312.3317.

[180] M. Buschmann, C. Englert, D. Goncalves, T. Plehn and M. Spannowsky, *Resolving the Higgs-Gluon Coupling with Jets*, Phys. Rev. D **90**, 013010 (2014), doi:10.1103/PhysRevD.90.013010, arXiv:1405.7651.

[181] M. Buschmann, D. Goncalves, S. Kuttimalai, M. Schonherr, F. Krauss and T. Plehn, *Mass Effects in the Higgs-Gluon Coupling: Boosted vs Off-Shell Production*, JHEP **02**, 038 (2015), doi:10.1007/JHEP02(2015)038, arXiv:1410.5806.

[182] C. Degrande, G. Durieux, F. Maltoni, K. Mimasu, E. Vryonidou and C. Zhang, *Automated one-loop computations in the standard model effective field theory*, Phys. Rev. D **103**, 096024 (2021), doi:10.1103/PhysRevD.103.096024, arXiv:2008.11743.

[183] ATLAS Collaboration, *Measurement of the properties of Higgs boson production at $\sqrt{s} = 13$ TeV in the $H \to \gamma\gamma$ channel using 139 fb^{-1} of pp collision data with the ATLAS experiment*, doi:10.48550/ARXIV.2207.00348 (2022).

[184] CMS Collaboration, *Measurements of Higgs boson production cross sections and couplings in the diphoton decay channel at $\sqrt{s} = 13$ TeV*, Journal of High Energy Physics **2021** (2021), doi:10.1007/jhep07(2021)027, `https://doi.org/10.1007%2Fjhep07%282021%29027`, arXiv:2103.06956.

[185] ATLAS Collaboration, *Search for associated production of a Z boson with an invisibly decaying Higgs boson or dark matter candidates at $\sqrt{s}$ = 13 TeV with the ATLAS detector*, Physics Letters B **829**, 137066 (2022), doi:10.1016/j.physletb.2022.137066, `https://doi.org/10.1016%2Fj.physletb.2022.137066`.

[186] CMS Collaboration, *Search for dark matter produced in association with a leptonically decaying Z boson in proton-proton collisions at $\sqrt{s}$ = 13 TeV*, Eur. Phys. J. C **81**, 13. 33 p (2020), doi:10.1140/epjc/s10052-020-08739-5, `https://cds.cern.ch/record/2727805`, arXiv:2008.04735.

[187] ATLAS Collaboration, *Search for invisible Higgs-boson decays in events with vector-boson fusion signatures using 139 fb^{-1} of proton-proton data recorded by the ATLAS experiment*, doi:10.48550/ARXIV.2202.07953 (2022).

[188] CMS Collaboration, *Search for invisible decays of the Higgs boson produced via vector boson fusion in proton-proton collisions at $\sqrt{s}$ = 13 TeV* (2022), doi:10.48550/ARXIV.2201.11585, `https://arxiv.org/abs/2201.11585`.

[189] ATLAS Collaboration, *Measurements of Higgs boson production cross-sections in the $H \to \tau^+\tau^-$ decay channel in pp collisions at $\sqrt{s} = 13$ TeV with the ATLAS detector*, doi:10.48550/ARXIV.2201.08269 (2022).

[190] CMS Collaboration, *Measurements of Higgs boson production in the decay channel with a pair of τ leptons in proton-proton collisions at $\sqrt{s}$ = 13 TeV*, doi:10.48550/ARXIV.2204.12957 (2022).

[191] CMS Collaboration, *Measurements of the Higgs boson production cross section and couplings in the W boson pair decay channel in proton-proton collisions at $\sqrt{s}$ = 13 TeV*, doi:10.48550/ARXIV.2206.09466 (2022).

[192] ATLAS Collaboration, *Measurements of WH and ZH production in the $H \to b\bar{b}$ decay channel in pp collisions at 13 TeV with the ATLAS detector*, Eur. Phys. J. C **81**, 178. 41 p (2020), doi:10.1140/epjc/s10052-020-08677-2, `https://cds.cern.ch/record/2723187`, arXiv:2007.02873.

[193] CMS Collaboration, *Evidence for Higgs boson decay to a pair of muons*, Journal of High Energy Physics **2021** (2021), doi:10.1007/jhep01(2021)148, `https://doi.org/10.1007%2Fjhep01%282021%29148`.

[194] B. Mellado Garcia, P. Musella, M. Grazzini and R. Harlander, *CERN Report 4: Part I Standard Model Predictions* (2016), `https://cds.cern.ch/record/2150771`.

[195] LHC Higgs Working Group, *SM Higgs production cross sections at $\sqrt{s} = 13$ TeV (update in CERN Report 4)* (2016), `https://twiki.cern.ch/twiki/bin/view/LHCPhysics/CERNYellowReportPageAt13TeV`.

[196] LHC Higgs Working Group, *SM Higgs Branching Ratios and Total Decay Widths (update in CERN Report 4)* (2016), `https://twiki.cern.ch/twiki/bin/view/LHCPhysics/CERNYellowReportPageBR`.

[197] G. Aad *et al.*, *Search for resonances decaying into a weak vector boson and a Higgs boson in the fully hadronic final state produced in proton−proton collisions at $\sqrt{s} = 13$ TeV with the ATLAS detector*, Phys. Rev. D **102**, 112008 (2020), doi:10.1103/PhysRevD.102.112008, arXiv:2007.05293.

[198] G. Aad *et al.*, *Combined measurements of Higgs boson production and decay using up to 80 fb^{-1} of proton-proton collision data at $\sqrt{s}$ = 13 TeV collected with the ATLAS experiment*, Phys. Rev. D **101**, 012002 (2020), doi:10.1103/PhysRevD.101.012002, arXiv:1909.02845.

[199] A. M. Sirunyan *et al.*, *Combined measurements of Higgs boson couplings in proton–proton collisions at $\sqrt{s}$ = 13 TeV*, Eur. Phys. J. C **79**, 421 (2019), doi:10.1140/epjc/s10052-019-6909-y, arXiv:1809.10733.

[200] J. Brehmer, A. Freitas, D. Lopez-Val and T. Plehn, *Pushing Higgs Effective Theory to its Limits*, Phys. Rev. D **93**, 075014 (2016), doi:10.1103/PhysRevD.93.075014, arXiv:1510.03443.

[201] C. Englert, R. Kogler, H. Schulz and M. Spannowsky, *Higgs coupling measurements at the LHC*, The European Physical Journal C **76** (2016), doi:10.1140/epjc/s10052-016-4227-1, http://dx.doi.org/10.1140/epjc/s10052-016-4227-1.

[202] S. Das Bakshi, J. Chakrabortty, C. Englert, M. Spannowsky and P. Stylianou, *CP violation at ATLAS in effective field theory*, Physical Review D **103** (2021), doi:10.1103/physrevd.103.055008, http://dx.doi.org/10.1103/PhysRevD.103.055008.

[203] Anisha, S. D. Bakshi, S. Banerjee, A. Biekötter, J. Chakrabortty, S. K. Patra and M. Spannowsky, *Effective limits on single scalar extensions in the light of recent LHC data*, doi:10.48550/ARXIV.2111.05876 (2021), arXiv:2111.05876.

[204] W. Kilian, T. Ohl, J. Reuter and M. Sekulla, *Resonances at the LHC beyond the Higgs boson: The scalar/tensor case*, Phys. Rev. D **93**, 036004 (2016), doi:10.1103/PhysRevD.93.036004, arXiv:1511.00022.

[205] A. Freitas, D. López-Val and T. Plehn, *When matching matters: Loop effects in Higgs effective theory*, Phys. Rev. D **94**, 095007 (2016), doi:10.1103/PhysRevD.94.095007, arXiv:1607.08251.

[206] I. Low, R. Rattazzi and A. Vichi, *Theoretical Constraints on the Higgs Effective Couplings*, JHEP **04**, 126 (2010), doi:10.1007/JHEP04(2010)126, arXiv:0907.5413.

[207] F. del Aguila, J. de Blas and M. Perez-Victoria, *Electroweak Limits on General New Vector Bosons*, JHEP **09**, 033 (2010), doi:10.1007/JHEP09(2010)033, arXiv:1005.3998.

[208] D. Pappadopulo, A. Thamm, R. Torre and A. Wulzer, *Heavy Vector Triplets: Bridging Theory and Data*, JHEP **09**, 060 (2014), doi:10.1007/JHEP09(2014)060, arXiv:1402.4431.

[209] A. Biekötter, A. Knochel, M. Krämer, D. Liu and F. Riva, *Vices and virtues of Higgs effective field theories at large energy*, Phys. Rev. D **91**, 055029 (2015), doi:10.1103/PhysRevD.91.055029, arXiv:1406.7320.

[210] V. D. Barger, W.-Y. Keung and E. Ma, *Doubling of Weak Gauge Bosons in an Extension of the Standard Model*, Phys. Rev. Lett. **44**, 1169 (1980), doi:10.1103/PhysRevLett.44.1169.

[211] N. Arkani-Hamed, A. G. Cohen and H. Georgi, *Electroweak symmetry breaking from dimensional deconstruction*, Phys. Lett. B **513**, 232 (2001), doi:10.1016/S0370-2693(01)00741-9, arXiv:hep-ph/0105239.

[212] S. Weinberg, *Implications of Dynamical Symmetry Breaking*, Phys. Rev. D **13**, 974 (1976), doi:10.1103/PhysRevD.19.1277, [Addendum: Phys.Rev.D 19, 1277–1280 (1979)].

[213] R. D. C. Miller, *Effective Field Theory and Weak Nonleptonic Interactions*, Phys. Rept. **106**, 169 (1984), doi:10.1016/0370-1573(84)90035-8.

[214] M. K. Gaillard, *The Effective One Loop Lagrangian With Derivative Couplings*, Nucl. Phys. **B 268**, 669 (1986), doi:10.1016/0550-3213(86)90264-6.

[215] L.-H. Chan, *Derivative Expansion for the One Loop Effective Actions With Internal Symmetry*, Phys. Rev. Lett. **57**, 1199 (1986), doi:10.1103/PhysRevLett.57.1199.

[216] O. Cheyette, *Effective Action for the Standard Model With Large Higgs Mass*, Nucl. Phys. **B 297**, 183 (1988), doi:10.1016/0550-3213(88)90205-2.

[217] R. D. Ball, *Chiral Gauge Theory*, Phys. Rept. **182**, 1 (1989), doi:10.1016/0370-1573(89)90027-6.

[218] B. S. DeWitt, *Quantum Theory of Gravity. 2. The Manifestly Covariant Theory*, Phys. Rev. **162**, 1195 (1967), doi:10.1103/PhysRev.162.1195.

[219] W. A. Bardeen, *Anomalous Ward identities in spinor field theories*, Phys. Rev. **184**, 1848 (1969), doi:10.1103/PhysRev.184.1848.

[220] G. 't Hooft, *The Background Field Method in Gauge Field Theories*, In *12th Annual Winter School of Theoretical Physics*, pp. 345–369 (1975).

[221] B. S. DeWitt, *A gauge invariant effective action*, In *Oxford Conference on Quantum Gravity*, pp. 449–487 (1980).

[222] D. G. Boulware, *Gauge Dependence of the Effective Action*, Phys. Rev. **D 23**, 389 (1981), doi:10.1103/PhysRevD.23.389.

[223] L. F. Abbott, *The Background Field Method Beyond One Loop*, Nucl. Phys. **B 185**, 189 (1981), doi:10.1016/0550-3213(81)90371-0.

[224] L. F. Abbott, *Introduction to the Background Field Method*, Acta Phys. Polon. **B 13**, 33 (1982).

[225] A. Denner, G. Weiglein and S. Dittmaier, *Application of the background field method to the electroweak standard model*, Nucl. Phys. B **440**, 95 (1995), doi:10.1016/0550-3213(95)00037-S, arXiv:hep-ph/9410338.

[226] A. Denner and S. Dittmaier, *Electroweak Radiative Corrections for Collider Physics*, Phys. Rept. **864**, 1 (2020), doi:10.1016/j.physrep.2020.04.001, arXiv:1912.06823.

[227] S. Dittmaier and C. Grosse-Knetter, *Deriving nondecoupling effects of heavy fields from the path integral: A Heavy Higgs field in an SU(2) gauge theory*, Phys. Rev. D **52**, 7276 (1995), doi:10.1103/PhysRevD.52.7276, arXiv:hep-ph/9501285.

[228] S. Dittmaier and C. Grosse-Knetter, *Integrating out the standard Higgs field in the path integral*, Nucl. Phys. B **459**, 497 (1996), doi:10.1016/0550-3213(95)00551-X, arXiv:hep-ph/9505266.

[229] J. Preskill, *Gauge anomalies in an effective field theory*, Annals Phys. **210**, 323 (1991), doi:10.1016/0003-4916(91)90046-B.

[230] O. Cata, W. Kilian and N. Kreher, *Gauge anomalies in the Standard-Model Effective Field Theory* (2020), doi:10.48550/ARXIV.2011.09976, arXiv:2011.09976.

[231] M. Beneke and V. A. Smirnov, *Asymptotic expansion of Feynman integrals near threshold*, Nucl. Phys. **B 522**, 321 (1998), doi:10.1016/S0550-3213(98)00138-2, arXiv:hep-ph/9711391.

[232] V. A. Smirnov, *Applied asymptotic expansions in momenta and masses*, Springer Tracts Mod. Phys. **177**, 1 (2002).

[233] B. Jantzen, *Foundation and generalization of the expansion by regions*, JHEP **12**, 076 (2011), doi:10.1007/JHEP12(2011)076, arXiv:1111.2589.

[234] B. Summ, *One Formula To Match Them All: The Bispinor Universal One-Loop Effective Action*, Ph.D. thesis, RWTH Aachen U., doi:10.18154/RWTH-2021-00828 (2020), arXiv:2103.02487.

[235] M. Bauer, P. Foldenauer and J. Jaeckel, *Hunting All the Hidden Photons*, JHEP **07**, 094 (2018), doi:10.1007/JHEP07(2018)094, arXiv:1803.05466.

[236] T. Cohen, N. Craig, X. Lu and D. Sutherland, *Is SMEFT Enough?*, JHEP **03**, 237 (2021), doi:10.1007/JHEP03(2021)237, arXiv:2008.08597.

[237] J. de Blas, J. C. Criado, M. Perez-Victoria and J. Santiago, *Effective description of general extensions of the Standard Model: the complete tree-level dictionary*, JHEP **03**, 109 (2018), doi:10.1007/JHEP03(2018)109, arXiv:1711.10391.

[238] T. Corbett, O. J. P. Eboli, D. Goncalves, J. Gonzalez-Fraile, T. Plehn and M. Rauch, *The Non-Linear Higgs Legacy of the LHC Run I* (2015), doi:10.48550/ARXIV.1511.08188, arXiv:1511.08188.

[239] M. Aaboud *et al.*, *Search for heavy resonances decaying into a W or Z boson and a Higgs boson in final states with leptons and b-jets in 36 fb^{-1} of $\sqrt{s} = 13$ TeV pp collisions with the ATLAS detector*, JHEP **03**, 174 (2018), doi:10.1007/JHEP03(2018)174, [Erratum: JHEP 11, 051 (2018)], arXiv:1712.06518.

[240] M. Trott, *Methodology for theory uncertainties in the standard model effective field theory*, Physical Review D **104** (2021), doi:10.1103/physrevd.104.095023, `http://dx.doi.org/10.1103/PhysRevD.104.095023`, arXiv:2106.13794.

[241] J. Baglio, S. Dawson, S. Homiller, S. D. Lane and I. M. Lewis, *Validity of standard model EFT studies of VH and VV production at NLO*, Phys. Rev. D **101**, 115004 (2020), doi:10.1103/PhysRevD.101.115004, arXiv:2003.07862.

[242] W. Kilian, T. Plehn, P. Richardson and E. Schmidt, *Split supersymmetry at colliders*, Eur. Phys. J. C **39**, 229 (2005), doi:10.1140/epjc/s2004-02046-5, arXiv:hep-ph/0408088.

[243] S. Dawson, P. P. Giardino and S. Homiller, *Uncovering the High Scale Higgs Singlet Model*, Phys. Rev. D **103**, 075016 (2021), doi:10.1103/PhysRevD.103.075016, arXiv:2102.02823.

[244] U. Haisch, M. Ruhdorfer, E. Salvioni, E. Venturini and A. Weiler, *Singlet night in Feynman-ville: one-loop matching of a real scalar*, JHEP **04**, 164 (2020), doi:10.1007/JHEP04(2020)164, [Erratum: JHEP 07, 066 (2020)], arXiv:2003.05936.

[245] A. Falkowski, M. Gonzalez-Alonso, A. Greljo, D. Marzocca and M. Son, *Anomalous Triple Gauge Couplings in the Effective Field Theory Approach at the LHC*, JHEP **02**, 115 (2017), doi:10.1007/JHEP02(2017)115, arXiv:1609.06312.

[246] J. Lang, S. Liebler, H. Schäfer-Siebert and D. Zeppenfeld, *Effective field theory versus UV-complete model: vector boson scattering as a case study*, The European Physical Journal C **81** (2021), doi:10.1140/epjc/s10052-021-09428-7, `http://dx.doi.org/10.1140/epjc/s10052-021-09428-7`, arXiv:2103.16517.

[247] V. Bresó-Pla, A. Falkowski, M. González-Alonso and K. Monsálvez-Pozo, *EFT for New Physics at COHERENT* (2023), To be published soon.